

# The SHMS 11GeV/c Spectrometer in Hall C at Jefferson Lab

S. Ali<sup>a</sup>, G.R. Ambrose<sup>b</sup>, A. Asaturyan<sup>c</sup>, V. Berdnikov<sup>a,d</sup>, P. Brindza<sup>d</sup>, R. Carlini<sup>d</sup>, M. Carmignotto<sup>a</sup>, D. Day<sup>b,k</sup>, A. Dittmann<sup>g</sup>, D. Dutta<sup>e</sup>, R. Ent<sup>d</sup>, H. Fenker<sup>d</sup>, M. Fowler<sup>d</sup>, D. Gaskell<sup>d</sup>, W. Henry<sup>d</sup>, N. Hlavin<sup>a</sup>, T. Horn<sup>a,d</sup>, G.M. Huber<sup>b</sup>, Y. Illieva<sup>f</sup>, M. K. Jones<sup>d,\*</sup>, S.J.D. Kay<sup>b,i</sup>, V. Kumar<sup>b</sup>, S. Lassiter<sup>d</sup>, W.B. Li<sup>b,j</sup>, A. Mkrtchyan<sup>a</sup>, H. Mkrtchyan<sup>c</sup>, P. Nadel-Turonski<sup>d</sup>, I. Pegg<sup>a</sup>, A. Ramos<sup>h</sup>, J. Reinhold<sup>h</sup>, I. Sapkota<sup>a</sup>, B. Sawatzky<sup>d</sup>, V. Tadevosyan<sup>c</sup>, R.L. Trotta<sup>a</sup>, M. Yurov<sup>k</sup>, S. Zhamkochyan<sup>c</sup>, S. A. Wood<sup>d</sup>, J. Zhang<sup>k</sup>

<sup>a</sup>The Catholic University of America, Washington, DC 20064, USA

<sup>b</sup>University of Regina, Regina, Saskatchewan S4S 0A2, Canada

<sup>c</sup>A. I. Alikhanyan National Science Laboratory, Yerevan 0036, Armenia

<sup>d</sup>Thomas Jefferson National Accelerator Facility, Newport News, Virginia 23606, USA

<sup>e</sup>Mississippi State University, Mississippi State, Mississippi 39762, USA

<sup>f</sup>University of South Carolina, Columbia, South Carolina 29208, USA

<sup>g</sup>University of Illinois, Urbana-Champaign, Illinois, USA

<sup>h</sup>Florida International University, University Park, Florida 33199, USA

<sup>i</sup>University of York, Heslington, York, YO10 5DD, UK

<sup>j</sup>Stony Brook University, Stony Brook NY 11794, USA

<sup>k</sup>University of Virginia, Charlottesville, Virginia 22904, USA

---

## Abstract

The *Super High Momentum Spectrometer* (SHMS) has been built for Hall C at the Thomas Jefferson National Accelerator Facility (Jefferson Laboratory). With a momentum capability reaching 11 GeV/c, the SHMS provides measurements of secondary charged particles produced in electron scattering experiments using the maximum available beam energy from the upgraded Jefferson Lab accelerator. The SHMS is an ion-optics magnetic spectrometer comprised of a series of new superconducting magnets which transport charged particles through an array of triggering, tracking, and particle-identification detectors that measure momentum, energy, angle and position in order to allow kinematic reconstruction of the events back to their origin at the scattering target. The detector system is protected from background radiation by a sophisticated shielding enclosure. The entire spectrometer is mounted on a rotating support structure which allows measurements to be taken with a large acceptance over laboratory scattering angles from 5.5° to 40°, thus allowing a wide range of low cross-section experiments to be conducted. These will complement and extend the previous Hall C research program to higher energies.

**Keywords:** Magnetic spectrometer, Electron scattering, Tracking detectors, Particle identification, Electron calorimetry, Radiation shielding.

---

## 1. Introduction

### 1.1. Jefferson Lab Overview

The Continuous Electron Beam Accelerator Facility at Thomas Jefferson National Accelerator Facility (Jefferson Lab) provides high energy electron beams for fundamental nuclear physics experiments. Originally planned for maximum electron beam energies of 4 GeV, the accelerator operated at energies of up to 6 GeV starting in 2000. An upgrade of the facility was recently

completed in 2017, enabling beam delivery at a maximum energy of 12 GeV to the new experimental Hall D, and 11 GeV to the existing Halls, A, B, and C.

The electron beam at Jefferson Lab operates at high duty cycle, with beam repetition rates of 249.5 or 499 MHz delivered to the experimental halls. High beam polarization (> 80%) is also routinely available.

In the 6 GeV era, Halls A, B, and C executed a large program of experiments focusing primarily on elucidating the quark-gluon structure of nucleons and nuclei. Experimental Hall B made use of a large acceptance spectrometer capable of detecting many-body final states over a large region of kinematic phase space

---

\*Corresponding author

in one setting. Halls A and C made use of magnetic focusing spectrometers. In Hall A, the two High Resolution Spectrometers (HRS) emphasized excellent momentum resolution. In Hall C, the Short Orbit Spectrometer (SOS) facilitated the detection of short-lived final states (pions and kaons) at modest momentum while the High Momentum Spectrometer was capable of detecting particles up to the maximum beam energy at Jefferson Lab.

As part of the 12 GeV upgrade at Jefferson Lab, a new experimental hall, Hall D, was built to search for gluonic excitations in the meson spectrum using a photon beam produced via coherent bremsstrahlung. The GlueX experiment in Hall D began commissioning in 2014 and has taken production-quality data since 2016.

The existing Halls A, B, and C were also upgraded as part of the 12 GeV upgrade. The Hall A beamline and beam polarimeters were upgraded to accommodate operation at 11 GeV. Hall A has made use of the existing HRS spectrometers in its early 12 GeV era experiments (which began initial data-taking in 2014) and has also installed specialized, dedicated equipment for recent measurements. Experimental Hall B replaced its large acceptance CLAS spectrometer with the new CLAS-12 spectrometer. This new spectrometer retains the key features of large acceptance and robust particle identification over a large momentum range but with more emphasis on particle detection in the forward direction, required due to the higher beam energies. Finally, Hall C replaced its Short Orbit Spectrometer with the new Super-High Momentum Spectrometer (SHMS). This new spectrometer was designed guided by experience from the 6 GeV program, with the goal of serving as an optimal partner to the HMS for coincidence experiments.

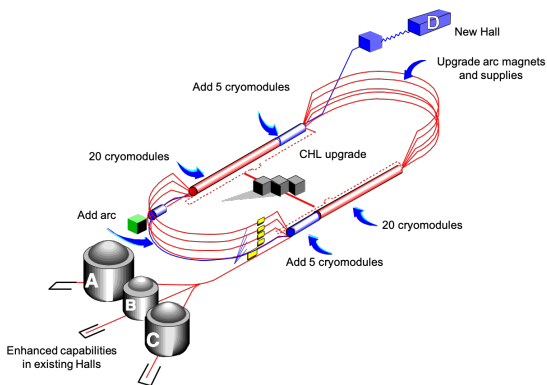


Figure 1: Schematic of hall and accelerator improvements as part of Jefferson Lab 12 GeV Upgrade.

### 1.2. Hall C Experimental Program at 6 GeV

The HMS and SOS spectrometers in Hall C enabled the execution of a diverse program of experiments. The well-understood acceptance of both spectrometers, in tandem with excellent kinematic reproducibility allowed the extraction of precise cross sections. A particular strength was the control of point-to-point systematic uncertainties, which allowed high precision Rosenbluth, or L-T, separations. Examples of inclusive cross section measurements, using primarily the HMS, are shown in Figs. 2 and 3.

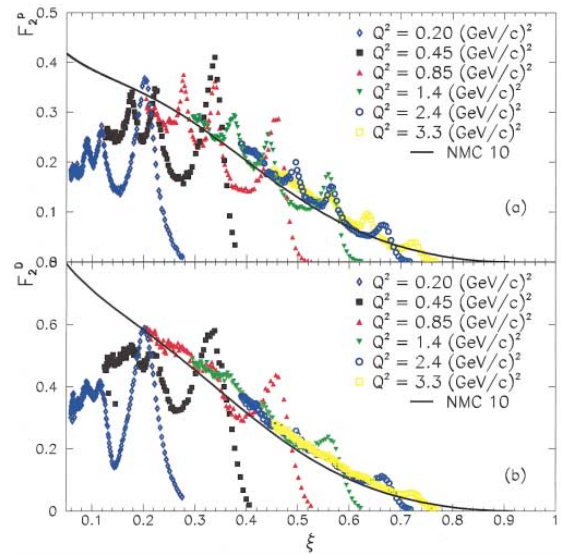


Figure 2: Inclusive  $F_2$  structure functions measured in the resonance region compared to a DIS fit. When plotted vs. the Nachtmann variable  $\xi$ , the DIS fit agrees, on average, with the resonance region data, demonstrating quark-hadron duality [1].

In addition, the small minimum angle (10.5 degrees) accessible with the HMS allowed the execution of pion electroproduction experiments, where, in many cases, the pion is emitted in the forward direction. This allowed the successful execution of a program of measurements of the pion form factor [3, 4], which also incorporates precise L-T separations, as well measurements of charged pion production in Semi-inclusive Deep Inelastic Scattering (SIDIS) [5] (see Figs. 4 and 5).

The high momentum reach of the HMS (up to the available beam energy of 6 GeV) enabled measurements of the  $A(e, e'p)$  process to large  $Q^2$  [6, 7] (Fig. 6) to look for signs of color transparency as well measurements of inclusive electron scattering at  $x > 1$  to access contributions of “superfast” quarks to inelastic structure func-

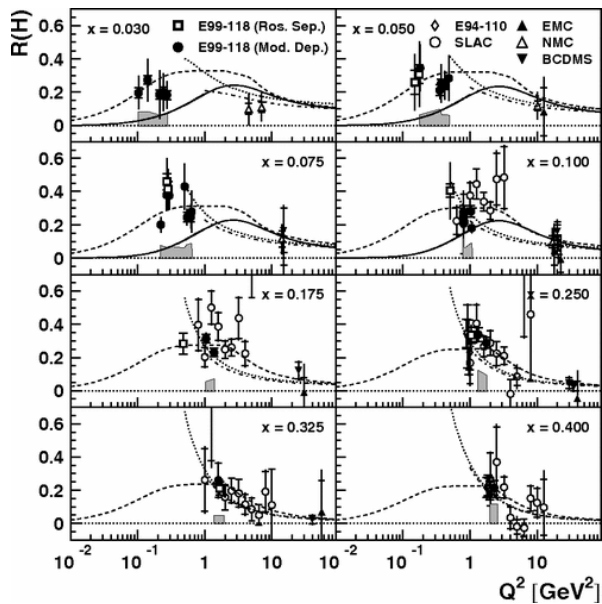


Figure 3: Measurement of  $R = \frac{\sigma_L}{\sigma_T}$  at low  $Q^2$ . The extraction of  $R$  requires precise L-T separations with excellent control of point-to-point systematic uncertainties. Figure from [2].

tions [8] and measure the relative contributions of Short Range Correlations (SRCs) in the nuclear wave function [9] (Fig. 7).

The experiments noted above are just a sample of the  $\sim 30$  “standard equipment” experiments that were executed in the 6 GeV era in Hall C. Other experiments include measurements of exclusive kaon production, resonance ( $\Delta$ ,  $S_{11}$ ) production, color transparency via pion electroproduction, and numerous inclusive electron scattering measurements using hydrogen and deuterium, as well as heavier nuclear targets. In some cases, the HMS was paired with dedicated equipment for special measurements. Examples of this include measurement of the ratio of elastic proton form factors ( $G_E/G_M$ ) to large  $Q^2$ , as well as measurements using a dynamically polarized  $\text{NH}_3$ .

### 1.3. Hall C 12 GeV Program

The new, Super-High Momentum Spectrometer was designed to build on the experimental capabilities exploited during the Hall C program at lower energies. Notably, this includes:

1. Excellent kinematic control and reproducibility.
2. Thorough understanding of spectrometer acceptance.
3. Small angle capability (down to 5.5 degrees) for detection of forward mesons.

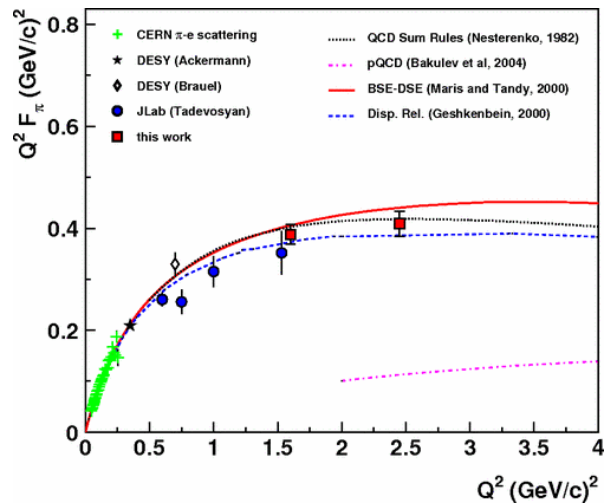


Figure 4: Measurements of the charged pion form factor in Hall C (6 GeV era). Extraction of the pion form factor requires a precise L-T separation, as well as detection of the charged pion at small forward angles. Figure from [4].

4. Central momentum up to (nearly) the maximum beam energy accessible in Hall C.
5. In-plane and out-of-plane acceptance well matched to the existing HMS to facilitate experiments detecting two particle in coincidence.

Several “commissioning” experiments were chosen for the first year of 12 GeV running in Hall C to exercise the above requirements as much as possible. These experiments ran in 2018 and will be discussed briefly below.

The first commissioning experiment was a measurement of inclusive electron scattering cross sections from hydrogen and deuterium [10] (see Fig. 8). Such a cross section experiment is an excellent testing ground for understanding of the spectrometer acceptance, while not pushing the SHMS performance in other areas. Some settings for this experiment were chosen to allow simultaneous measurement with the well-understood HMS to provide a cross section. In addition, some time was devoted to the measurement of inclusive cross section ratios for nuclear targets relative to deuterium [11]. These ratios are well-measured for certain nuclei and serve as another straightforward verification of the spectrometer acceptance due to the need to compare yields from extended (10 cm long) targets to shorter, solid targets (mm scale). These measurements resulted in the first extraction of the EMC Effect in  $^{10}\text{B}$  and  $^{11}\text{B}$  [12].

An extension of the 6 GeV color transparency experiments to larger  $Q^2$  [13] served as an excellent first experiment with which to exercise the SHMS in coin-

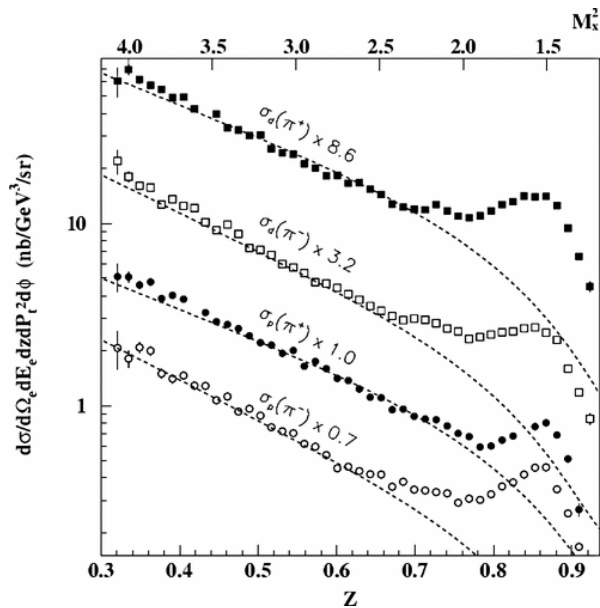


Figure 5: Cross sections for semi-inclusive  $\pi^+$  and  $\pi^-$  production from hydrogen and deuterium. The cross sections are compared to a parameterization that uses fragmentation functions fit to high energy  $e^+e^-$  collisions. Figure from [5].

141 cidence mode. In this  $A(e, e'p)$  experiment, there are  
 142 few random coincidences so isolating the coincidence  
 143 reaction is straightforward. This experiment, as well as  
 144 a measurement of deuteron electro-disintegration [14],  
 145 also tested the high momentum capabilities of the  
 146 SHMS. The SHMS was used at momenta larger than  
 147 8.5 GeV/c for these experiments. Although the maximum  
 148 central momentum of the SHMS is almost 11  
 149 GeV, 8.5 GeV/c was already sufficient to learn about the  
 150 performance of the superconducting magnets and spec-  
 151 trometer optics when pushed to a significant fraction of  
 152 the spectrometer's ultimate capabilities. In addition, the  
 153 body of  $H(e, e'p)$  data acquired for both these initial  
 154 coincidence experiments served to provide constraints on  
 155 the experiment kinematics, allowing one to test the possible  
 156 variation of, e.g. the spectrometer pointing or central  
 157 momentum for various settings. Results from the color  
 158 transparency and deuteron electro-disintegration  
 159 experiments are shown in Figs. 9 and 10.

160 A set of meson electroproduction experiments fol-  
 161 lowed the initial commissioning experiments and fur-  
 162 ther exercised the SHMS capabilities. Two of the ex-  
 163 periments measured charged pion electroproduction in  
 164 semi-inclusive deep inelastic scattering [17, 18]. The  
 165 SHMS was used at central angles smaller than  $7^\circ$  for the  
 166 SIDIS running. An additional challenge was the rela-  
 167 tively high singles rates in the SHMS. Both experiments

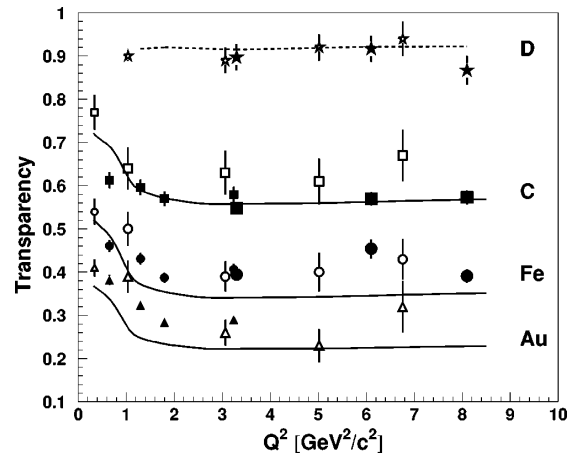


Figure 6: Measurement of transparency for  $(e, e'p)$ . Solid points are from (6 GeV era) Hall C measurements [6, 7]. At the largest  $Q^2$ , the HMS momentum is  $> 5$  GeV. Figure from [7].

168 aimed to make precise measurements of  $\pi^+/\pi^-$  ratios,  
 169 so control of rate dependent systematic effects is a key  
 170 challenge. The third experiment [19] measured exclu-  
 171 sive cross sections for  $K^+$  production above the reso-  
 172 nance region, in particular, extracting the longitudinal  
 173 and transverse cross sections via a Rosenbluth separa-  
 174 tion. In this case, the experimental uncertainties are ex-  
 175 pected to be dominated by statistics, so this serves as an  
 176 excellent candidate for a first L-T separation, since the  
 177 systematic requirements are less stringent. In common  
 178 with the charged pion SIDIS experiments, the kaon ex-  
 179 periment required use of the SHMS at small angles and  
 180 had to face the challenge of high singles rates.

181 The "commissioning" and "year-1" experiments de-  
 182 scribed above give a sense of the SHMS capabilities  
 183 important for the overall physics program. Since then,  
 184 a variety of experiments have been completed in Hall  
 185 C. These include measurements of  $J/\Psi$  photoproduc-  
 186 tion [20], virtual Compton scattering [21], exclusive  
 187 charged pion electroproduction to extract the pion form  
 188 factor and for cross section scaling tests [22], inclusive  
 189 electron scattering from polarized  $^3\text{He}$  to extract  $A_1^n$  and  
 190  $d_2^n$  [23, 24], and exclusive and inclusive scattering from  
 191 nuclei to make measurements of short range correla-  
 192 tions and the EMC Effect [25, 26, 11]. In the future, ad-  
 193 ditional L-T separations in inclusive scattering (to mea-  
 194 sure  $R = \frac{\sigma_L}{\sigma_T}$  from hydrogen, deuterium, and several nu-  
 195 clei) and semi-inclusive reactions (to make the first pre-  
 196 cise measurement of  $R$  for the SIDIS reaction) are also  
 197 planned. While not all future experiments will make  
 198 use of the SHMS, it is a key component of the Hall C  
 199 12 GeV experimental program.

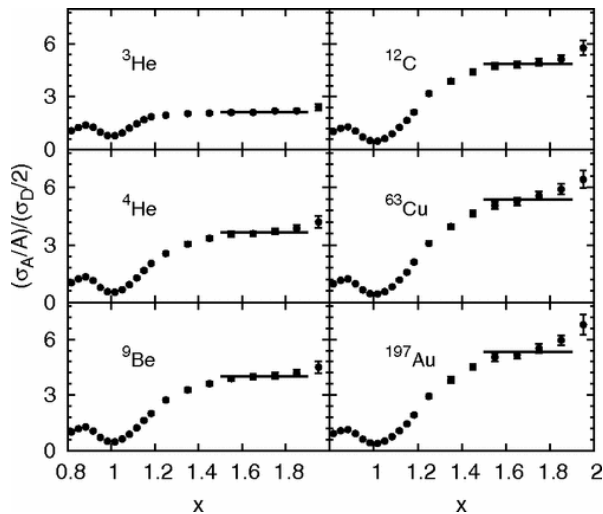


Figure 7: Measurements of cross section ratios for nuclear targets relative to deuterium at  $x > 1$ . The size of the ratio is proportional to the relative contributions of 2-nucleon Short Range Correlations to the nuclear wave function. These measurements required high momentum in the HMS. Figure from [9].

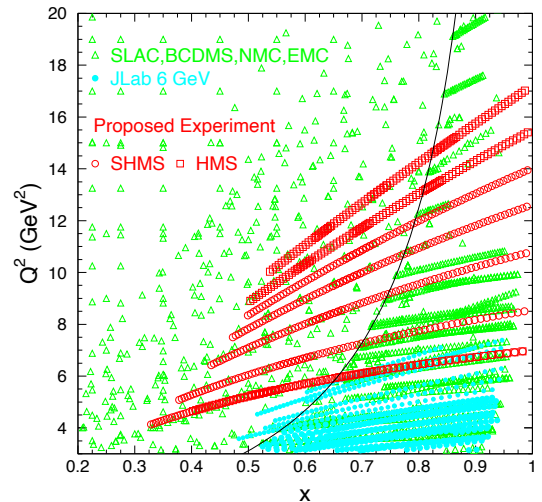


Figure 8: Kinematic coverage of  $F_2$  measurements from experiment E12-10-002 [10], which measured inclusive electron scattering cross sections as part of Hall C's 12 GeV commissioning experiments.

## 2. Specifications for the upgraded Hall-C Spectrometer complex

The physics outlined in the previous section can be accessed only if the Hall C spectrometer system is capable of providing the necessary measurements with precision, rate, and trigger capabilities consistent with those physics goals. Originally, Hall C offered the 7.4 GeV/c High Momentum Spectrometer (HMS) and its lower-momentum (1.8 GeV/c) partner, the Short-Orbit Spectrometer (SOS). These two devices were utilized independently by some experiments and in coincidence by others. The performance specifications for the SHMS were drafted such that the SHMS-HMS pair would provide similar complimentary functions in the higher-momentum regime. That is, the SHMS was developed as a general-purpose spectrometer with properties similar to the existing HMS, but with a higher maximum momentum capability (11 GeV/c). The 11 GeV/c limit of the SHMS was selected because the accelerator constrained maximum beam energy to any of the first generation endstations (A, B, C) is 11 GeV/c. Table 1 summarizes the demonstrated performance of the HMS and the design specifications for the SHMS.

With the higher beam energies in use at Jefferson Lab after the 12 GeV upgrade, scattered electrons and secondary particles are boosted to more forward directions. Thus the SHMS acceptance is made to extend down to a  $5.5^\circ$  scattering angle, and needs to cover angles no higher than  $40^\circ$ . Nevertheless, high energies

generally lead to smaller cross sections. Therefore precision experiments can be performed only if a spectrometer provides large overall acceptance, high rate capability, and precise momentum measurement. As shown in Table 1, the SHMS design includes a momentum bite even larger than the HMS, and achieves an angular acceptance within a factor of two of its low-energy partner. The combination of dispersive optics and precision tracking provides excellent momentum resolution. Triggering, data-acquisition, and particle identification rates are the same or better than those of the HMS. This performance is achieved not only through the use of faster, modern electronics, but also by innovative radiation shielding that reduces the background flux seen by the detectors.

## 3. Design and Development of the SHMS Systems

In this section we present design details and data demonstrating the performance of each the SHMS subsystems. The entire spectrometer is carried on a steel support structure which can rotate through an arc on the left side of the beam-line in Hall C. Like the HMS carriage, it is secured to a central pivot so that it rotates around a vertical axis that intersects the electron beam-line at the experimental target. This is shown in Fig. 11.

Acceptance at the smallest scattering angles is enabled by the presence of a horizontal-bending dipole as the first element in the magnetic optical system. This small deflection moves the subsequent pieces of the

<i>Parameter</i>	<i>HMS Performance</i>	<i>SHMS Specification</i>
Range of Central Momentum	0.4 to 7.4 GeV/c	2 to 11 GeV/c
Momentum Acceptance	$\pm 10\%$	-10% to +22%
Momentum Resolution	0.1% – 0.15%	0.03% – 0.08%
Scattering Angle Range	10.5° to 90°	5.5° to 40°
Target Length Accepted at 90°	10 cm	25 cm
Horizontal Angle Acceptance	$\pm 32$ mrad	$\pm 18$ mrad
Vertical Angle Acceptance	$\pm 85$ mrad	$\pm 45$ mrad
Solid Angle Acceptance	8.1 msr	4 msr
Horizontal Angle Resolution	0.8 mrad	0.5 – 1.2 mrad
Vertical Angle Resolution	1.0 mrad	0.3 – 1.1 mrad
Target resolution ( $y_{tar}$ )	0.3 cm	0.1 - 0.3 cm
Maximum Event Rate	4–5 kHz	4–5 kHz
Max. Flux within Acceptance	$\sim 5$ MHz	$\sim 5$ MHz
e/h Discrimination	>1000:1 at 98% efficiency	>1000:1 at 98% efficiency
$\pi/K$ Discrimination	100:1 at 95% efficiency	100:1 at 95% efficiency

Table 1: Demonstrated Performance of the HMS and Design Specifications for the SHMS. Resolutions are quoted at 1 sigma.

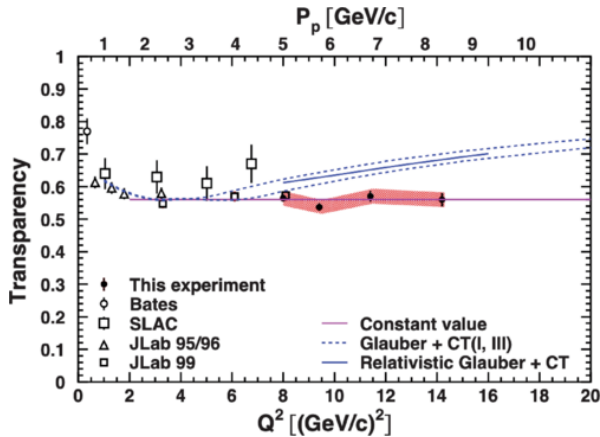


Figure 9: Results from experiment E12-06-107, a measurement of color transparency to large  $Q^2$  [15] (Hall C commissioning experiment). This measurement served as the first coincidence measurement in the 12 GeV era in Hall C.

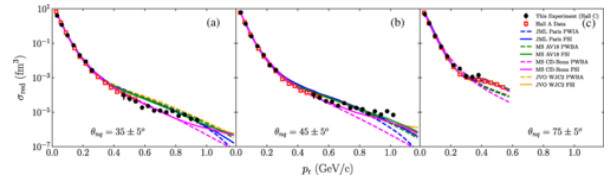


Figure 10: Results from experiment E12-10-003, a measurement of deuteron electro-disintegration at large missing momentum [16] (Hall C commissioning experiment).

266 provided by twelve planes of conventional drift chambers, and particle identification uses gas and aerogel  
267 Cherenkov counters, a preshower counter, and a total-  
268 absorption shower counter. The detector system details  
269 are presented in sections 3.3 through 3.9. Details of the  
270 event-triggering schemes, the data-acquisition system,  
271 and software appear in sections 4 and 5.  
272

### 273 3.1. Magnetic Optics

274 The SHMS consists of five magnets used to deter-  
275 mine the momentum, angles and position of particles  
276 scattered from the target using their angle and posi-  
277 tion measurements by the SHMS detectors. The first  
278 is a dipole magnet which bends the incident particles  
279 in the horizontal plane. A quadrupole triplet provides  
280 a point-to-point focus. To optimize acceptance in the  
281 vertical scattering plane, the first quadrupole focuses in  
282 the vertical while the second quadrupole defocuses and

257 SHMS farther from the beamline, relaxing the size con-  
258 straints on the other magnetic elements (described in  
259 Section 3.1) and shielding (Section 3.2). The shielded  
260 enclosure is itself a technically-optimized combination  
261 of concrete, lead, boron, and plastic. It surrounds the  
262 detectors and the electronics of the control and data-  
263 acquisition systems.

264 Basic trigger information comes from four planes  
265 of scintillator or quartz-bar hodoscopes. Tracking is

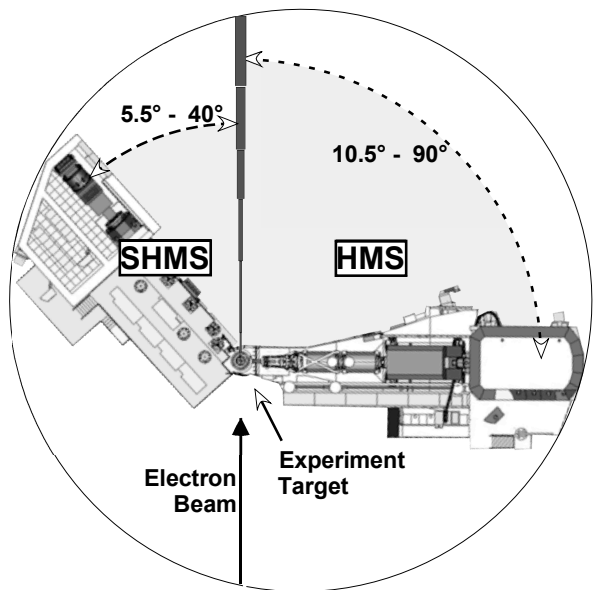


Figure 11: Simplified Plan View of Hall C showing the footprints of the SHMS and HMS. The SHMS occupies the smaller side of Hall C, where the smaller, low-momentum Short-Orbit Spectrometer (SOS) had been previously located.

283 the third quadrupole focuses. A vertical-bending dipole  
 284 magnet follows the last quadrupole and disperses parti-  
 285 cles with different momenta across the focal plane. In  
 286 point-to-point optics, all particles with the same mo-  
 287 mentum will be displaced by the same vertical distance  
 288 in the focal plane.

### 289 3.1.1. The Magnets and Vacuum Channel

290 A specially-designed horizontal-bend dipole (HB)  
 291 precedes the first quadrupole. Its purpose is to provide  
 292 an initial  $3^\circ$  separation between scattered particles and  
 293 the electron beam so that particles scattered at small an-  
 294 gles can be accepted.

295 As shown in Fig. 11, in order to fit within the space  
 296 available in Hall C the SHMS must be even shorter  
 297 than its lower-momentum partner, the HMS. All of the  
 298 SHMS magnets are superconducting so that they can  
 299 provide the necessary large bending and focusing effects  
 300 in short distances. Given the small-angle acceptance re-  
 301 quirement, the HB and the first two quadrupoles (Q1  
 302 and Q2) must have special provisions to provide clear-  
 303 ance for the electron beam and its vacuum pipe. HB  
 304 is a “C”-magnet so that all of the flux-return iron is on  
 305 the side away from the beamline. The front of the HB  
 306 cryostat, between the beamline and the magnet bore,  
 307 is made very narrow. Both Q1 and Q2 have notches  
 308 in their cryostats and iron yokes so that they, too, can  
 309 clear the beamline when the spectrometer is configured

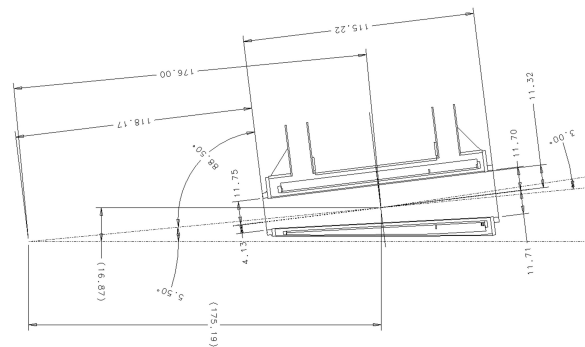


Figure 12: Top view schematic of the horizontal bender (HB) magnet with dimensions given in units of cm. The center of the HB magnet is at  $5.5^\circ$  for the beam line and 176 cm from the hall center.

310 at small scattering angles. Yoke steel for Q1 is inside  
 311 the cryostat. The final quadrupole (Q3) and the dipole  
 312 ( $D_{SHMS}$ ) have external warm yokes. Parameters of the  
 313 SHMS magnets are provided in Table 2.

314 To minimize multiple scattering as particles pass  
 315 through the SHMS, the bores of all of the magnets are  
 316 evacuated. The vacuum space begins at a window on  
 317 the front of HB. The entrance window into HB is ap-  
 318 proximately 15 cm square and is made of 0.01” thick  
 319 aluminum. A vacuum connection is made between the  
 320 exit of HB and Q1 entrance which is followed by the  
 321 40 cm diameter vacuum bore in Q1. The exit of Q1  
 322 is connected to the entrance of Q2 by a vacuum pipe.  
 323 The vacuum vessel bore through Q2, Q3, and  $D_{SHMS}$  is  
 324 60 cm in diameter. The location of the end of the vac-  
 325 uum after the exit of  $D_{SHMS}$  depends on the needs of  
 326 the experiment. If the experiment needs the Noble Gas  
 327 Cherenkov (NGC) detector (described in Sec. 3.7), then  
 328 a window is placed at the exit of  $D_{SHMS}$  with the NGC  
 329 detector placed between the exit window and the drift  
 330 chambers. Otherwise, a Vacuum Extension Tank (VET)  
 331 is attached to the exit of the  $D_{SHMS}$  that puts the exit  
 332 window at 30 cm from the first drift chamber in the de-  
 333 tector stack. In both cases, the dipole exit window is  
 334 made of 0.020” thick aluminum.

### 335 3.1.2. Optics

The relative strengths of the integral fields of the  
 magnets are set to maximize acceptance while at the  
 same time optimizing resolution in momentum and scat-  
 tering angle. The transport of a particle with the relative  
 momentum,  $\delta = \frac{p-p_c}{p_c}$ , from the target to midway be-  
 tween the two set drift chambers in the focal plane of the  
 SHMS can be characterized by an optics matrix. The  
 particle momentum is  $p$  and the central momentum of

<i>Parameter</i>	<i>HB</i>	<i>Q1</i>	<i>Q2</i>	<i>Q3</i>	<i>D<sub>SHMS</sub></i>
Max Field or Gradient	2.6 T	7.9 T/m	11.8 T/m	7.9 T/m	3.9 T
Effective Field Length	0.80 m	1.9 m	1.6 m	1.6 m	2.9 m
Current at 11 GeV/c	3923 A	2322 A	3880 A	2553 A	3510 A
Aperture	14.5x18 cm	40 cm	60 cm	60 cm	60 cm

Table 2: Parameters of the SHMS Magnets

the spectrometer is  $p_c$ . The particle starts with the vertical and horizontal positions ( $x_{tar}$  and  $y_{tar}$ ) and angles ( $x'_{tar} = \frac{\Delta x_{tar}}{\Delta z_{tar}}$  and  $y'_{tar} = \frac{\Delta y_{tar}}{\Delta z_{tar}}$ ) in the  $z_{tar} = 0$  plane. These positions and angles are measured relative to the central ray of the spectrometer. After magnetic transport, it arrives at the focal plane with the vertical and horizontal positions ( $x_{fp}$  and  $y_{fp}$ ) and angles ( $x'_{fp}$  and  $y'_{fp}$ ). The first order optics matrix is

$$\begin{pmatrix} x_{fp} \\ x'_{fp} \\ y_{fp} \\ y'_{fp} \end{pmatrix} = \begin{pmatrix} -1.5 & 0.0 & 0.0 & 0.0 & 1.65 \\ -0.5 & -0.7 & 0.0 & 0.0 & 3.2 \\ 0.0 & 0.0 & -1.9 & -0.2 & -0.1 \\ 0.0 & 0.0 & -3.0 & -0.8 & 0.1 \end{pmatrix} \begin{pmatrix} x_{tar} \\ x'_{tar} \\ y_{tar} \\ y'_{tar} \\ \delta \end{pmatrix} \quad (1)$$

The units of the positions, angles and  $\delta$  are in centimeters, milliradians and %.

The acceptance of the spectrometer is mainly determined by the collimator that is placed between the HB magnet and the first quadrupole. A remotely-operated collimator box is installed on the SHMS between the HB and Q1 magnets. The collimator ladder assembly within this box may be positioned at three settings. The top position (accessed when the assembly is at its lowest position) is a stretched octagon with opening height 9.843" and width 6.693" on the upstream side. It is 2.5" thick. The lower two positions both present sieve holes in rectangular pattern with holes separated by 0.6457" horizontally and 0.9843" vertically. The sieve pattern at the middle ladder position has 11 columns of holes with the sixth column centered horizontally. The holes on the bottom sieve are in ten columns and are offset by one-half a column gap from those in the middle sieve. The sieve collimators are 1.25" thick. The geometry is illustrated in Fig. 13. Both sieves and octagonal collimator are made of Mi-Tech™ Tungsten HD-17 (Density 17 g/cc, 90% W, 6% Ni, 4% Cu).

To determine the vertical size of the collimator studies were done with SNAKE (magnet transport code). Without the collimator, the vertical acceptance is mainly determined by the mechanical exit of the HB magnet. The vertical size of  $\pm 12.5$  cm was chosen to match this vertical cut-off to maximize the acceptance. Two vertical sizes of  $\pm 8$  cm and  $\pm 10.5$  cm for the collimators

were studied. A plot of the acceptance of each collimator versus  $\delta$  is shown in Fig. 14. The acceptance drops from an average of 4 msr for  $\pm 12.5$  cm to an average of 3 msr for  $\pm 8$  cm. Another consideration is minimizing the loss of events in the bore of the vertical dipole after they pass the entrance of the dipole. A plot in Fig. 14 shows the fraction of events which make it to the focal plane. The number of events lost in the dipole bore as a function of  $\delta$  is reduced by decreasing the vertical height of the collimator. With the  $\pm 12.5$  cm collimator, the fraction of events making to the focal plane drops to 75% at  $\delta = 0.15$ . The decision was made to use the  $\pm 12.5$  cm vertical opening to maximize the solid angle acceptance of the SHMS at the expense of increased reliance on the understanding the losses in the SHMS dipole bore.

SNAKE was also used to model the acceptance of the SHMS. The mechanical sizes of the magnets and magnet field maps from TOSCA are used to create a model of the SHMS in SNAKE. The acceptance of the SHMS versus  $\delta$  determined by SNAKE is plotted in Fig. 15. A separate calculation is done using the Hall C Monte Carlo (SIMC) simulation which uses the COSY transport matrix. The acceptance of the SHMS versus  $\delta$  determined by SIMC is also plotted in Fig. 15. As seen in this figure, the agreement between the two calculations is excellent.

The reconstruction of a particle's momentum, horizontal target position, vertical and horizontal angles from the focal plane positions and angles can also be represented by an optics matrix. Each event calculates the target interaction point from the tracks reconstructed in the focal plane using the drift chamber information. Target offsets, beam offsets and spectrometer mis-pointings are accounted for separately when reconstructing events. The optics matrix elements consist of a set of coefficients and the values of the powers for each focal plane element. The coefficients for each focal plane variable are  $X'$ ,  $Y$ ,  $Y'$ , and  $D$ , and the powers of each focal plane variable are represented by  $ijklm$ . The powers for each term range from zero to six with the sum of the powers for a given term not exceeding



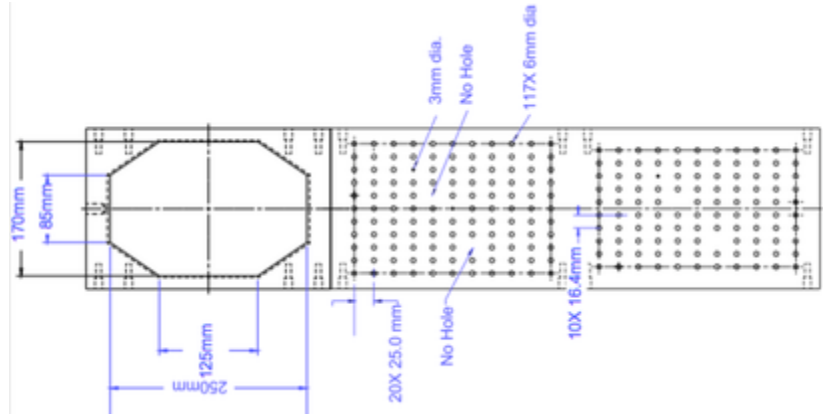


Figure 13: Schematic diagram of the SHMS collimator.

407 six. The reconstruction equations for the target quanti- 413  
 408 ties are written as shown in Eq. 2.

$$\begin{aligned}
 x'_{tar} &= \sum_{ijklm} X'_{ijklm} x_{fp}^i x_{fp}^j y_{fp}^k y_{fp}^l x_{tar}^m \\
 y_{tar} &= \sum_{ijklm} Y_{ijklm} x_{fp}^i x_{fp}^j y_{fp}^k y_{fp}^l x_{tar}^m \\
 y'_{tar} &= \sum_{ijklm} Y'_{ijklm} x_{fp}^i x_{fp}^j y_{fp}^k y_{fp}^l x_{tar}^m \\
 \delta &= \sum_{ijklm} D_{ijklm} x_{fp}^i x_{fp}^j y_{fp}^k y_{fp}^l x_{tar}^m
 \end{aligned} \quad (2)$$

409 From Eq. 2, it can be seen that the target reconstruction 426  
 410 is actually under-determined. For each event, there 427  
 411 are four given quantities ( $x_{fp}$ ,  $y_{fp}$ ,  $x'_{fp}$ ,  $y'_{fp}$ ) and five un- 428  
 412 knowns to solve for ( $x_{tar}$ ,  $y_{tar}$ ,  $x'_{tar}$ ,  $y'_{tar}$ , and  $\delta$ ).  $x_{tar}$  is 429

never directly measured, but it is reconstructed with the 413  
 414 knowledge of the beam position and reconstructed val- 415  
 416 ues of  $y_{tar}$ ,  $x'_{tar}$ ,  $y'_{tar}$ . The  $x_{tar}$  dependent coefficients are 417  
 418 used directly from COSY calculations with the recon- 419  
 420 structed  $x'_{tar}$  and  $\delta$  being most sensitive to knowledge of 421  
 422  $x_{tar}$ . To account for  $x_{tar}$ , an iterative procedure is done 423  
 424 where first the  $y_{tar}$ ,  $x'_{tar}$ ,  $y'_{tar}$  and  $\delta$  are calculated by set- 425  
 426 ting  $x_{tar}$  equal to the vertical beam position. Then  $x_{tar}$  is 427  
 428 calculated using the vertical beam position,  $y_{tar}$ ,  $x'_{tar}$  and 429  
 429  $y'_{tar}$  and the reconstruction matrix is recalculated with 430  
 431 the new  $x_{tar}$ . This is repeated in a loop until the change 432  
 433 in  $x'_{tar}$  compared to the previous iteration is less than 434  
 435 2 mrad for no more than five iterations.

The determination of  $x_{tar}$  independent coefficients 436  
 437 (when  $m = 0$  in Eq. 2) in the reconstructed matrix el- 438  
 439 ements was done using data from specific run settings. 440  
 441 In all cases, a single or multi-foil carbon target is used 442

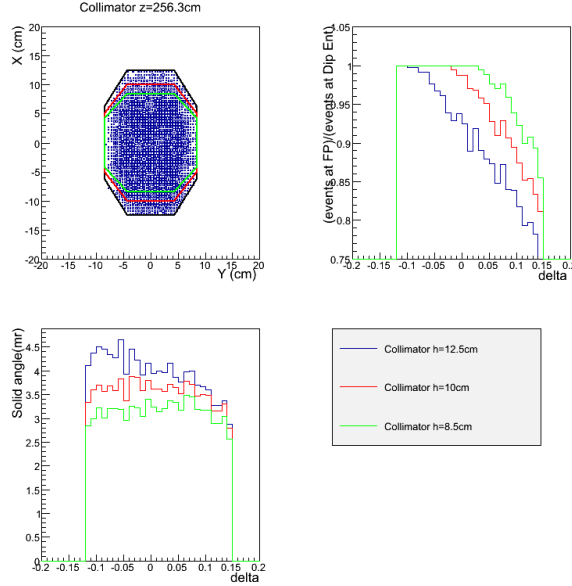


Figure 14: The upper left figure is distribution of events at the location of the collimator with three different vertical size collimators. The lower left figure is the acceptance as a function of  $\delta$  for each of the collimators. The upper right figure is the fraction of events lost in the dipole bore after the dipole entrance.

430 with a sieve installed downstream from the target. For  
 431 each interaction that pass through a sieve hole, all true  
 432 target quantities, including  $x_{tar}$ , can be calculated from  
 433 knowledge of the beam position, foil location and sieve  
 434 hole location.

435 The calibration of the  $\delta$  matrix elements was done us-  
 436 ing carbon elastic data. Using the first order optics from  
 437 COSY and selecting events from a carbon target inter-  
 438 action that pass through a single hole in the sieve, the  
 439 carbon elastic peak and excitation spectrum is clearly  
 440 seen as shown in Fig. 16.

441 The carbon energy spectrum shows the elastic peak  
 442 and the 4.4 MeV carbon excited state. Additional car-  
 443 bon states are observable in the smaller peaks to the  
 444 right of the 4.4 MeV peak. The  $\delta$  matrix elements were  
 445 optimized by taking a series of runs where the carbon  
 446 elastic peak moved across the focal plane for incremen-  
 447 tal settings of the spectrometer central momentum.

448 The optimization of the reconstructed target quanti-  
 449 ties  $y_{tar}$ ,  $y'_{tar}$ , and  $x'_{tar}$  used data from multi-foil carbon  
 450 targets with the sieve inserted in the beam line. Each

451 hole in the sieve is used to define the true physical values  
 452 of an event and is compared to the reconstructed angles  
 453 and positions for optimization. The reconstructed  $y_{tar}$   
 454 is approximately  $z_{tar} \sin \theta$  where  $\theta$  is the central angle  
 455 of the spectrometer, and  $z_{tar}$  is the target foil position  
 456 in the hall beam line coordinate system. To optimize over  
 457 the full range of possible  $y_{tar}$  values, data must be taken  
 458 with the spectrometer at various central angles. Two  
 459 sieves were used to collect the data having the same hole  
 460 patterns: one where the central hole was centered on the  
 461 spectrometer axis and the other where the central hole  
 462 was shifted by half the distance between the holes rela-  
 463 tive to the spectrometer axis. Data was taken with each  
 464 sieve separately in order optimize the full spectrometer  
 465 acceptance. A reconstructed sieve pattern using a single  
 466 carbon foil is shown in Fig. 17.

467 The general procedure for the optimization of the  
 468 target quantities  $y_{target}$ ,  $y'_{target}$ , and  $x'_{target}$  is as follows:  
 469 the events are initially reconstructed using the origi-  
 470 nal reconstruction matrix elements generated from the  
 471 COSY model. These events are used to determine the

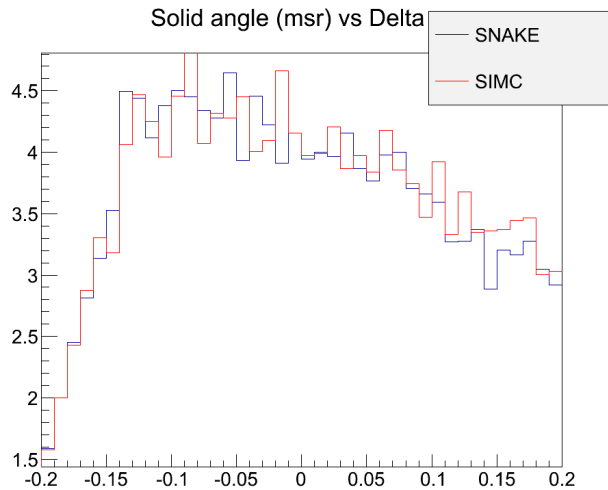


Figure 15: Comparison of predicted SHMS acceptance using the Hall C Monte Carlo (SIMC) and the magnetic transport code SNAKE.

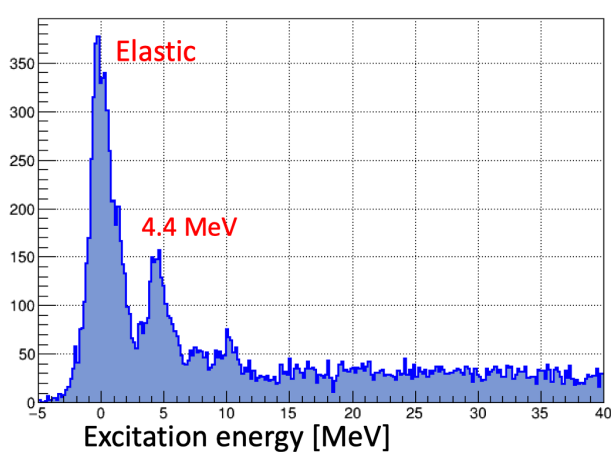


Figure 16: The carbon elastic energy spectrum for events for a single sieve hole, as calculated in terms of delta from the first order optics, clearly shows the carbon elastic peak and the 4.4 MeV excited state.

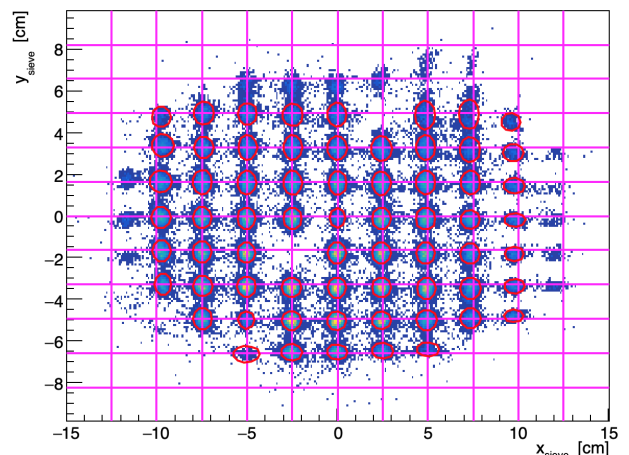


Figure 17: The sieve pattern is reconstructed here where the true sieve hole positions are indicated by the magenta cross lines and the reconstructed holes are outlined in red. The holes at the edges of the sieve are somewhat shifted from the true desired values.

472 true physical values by determining which target foil an  
 473 event originated from and which sieve hole the event  
 474 passed through. The differences between the measured  
 475 events and the real true physical values are minimized  
 476 by solving a Singular Value Decomposition (SVD) to  
 477 calculate the optimized/improved reconstruction matrix  
 478 elements.

479 **Need to mention the reconstructed angular resolu-**  
 480 **tions. From CT, I obtained 0.9 mrad horizontal and**  
 481 **1.1 mrad vertical.**

### 482 3.2. Shield House Layout, Shielding Design

483 The radiation environment is an important consid-  
 484 eration for the design of the SHMS shield house, in  
 485 particular, the effect of radiation-induced effects on the  
 486 performance and reliability of detectors and electron-  
 487 ics. It has been shown that many new commercial off  
 488 the shelf components are sensitive to radiation dam-  
 489 age and single event upsets, requiring a careful evalu-

490 ation of the impact of the radiation-induced effects on 542  
491 their performance and reliability [27, 28]. A specialized 543  
492 SHMS shield house design was thus developed at Jef- 544  
493 ferson Lab. Shielding thicknesses were optimized using 545  
494 a Monte Carlo simulation and benchmarked against the 546  
495 HMS shielding house, which has been proven to pro- 547  
496 vide the necessary detector shielding over more than a 548  
497 decade of experiments at the 6 GeV JLab. A full de- 549  
498 scription of the shielding optimization can be found in 550  
499 Ref. [29]. 551

500 The primary particle radiation is created when the 552  
501 CEBAF electron beam strikes the experimental target. 553  
502 The main components are scattered electrons, neutral 554  
503 particles (photons and neutrons), and charged hadrons. 555  
504 The energy spectrum of this radiation depends on the 556  
505 incident beam energy and decreases generally as  $1/E$ . It 557  
506 has been shown that the most efficient way to protect 558  
507 the experimental equipment from radiation damage is 559  
508 to build an enclosure around it using certain key ma- 560  
509 terials. The type and thickness of the shield house walls 561  
510 depends on the energy and particle one needs to shield 562  
511 against. However, one may qualitatively expect that the 563  
512 largest amount of shielding material is needed on the 564  
513 side facing the primary source, which in the case of the 565  
514 Hall C focusing spectrometers is the front face. Addi- 566  
515 tional sources of radiation are the beampipe, which ex- 567  
516 tends from the experimental target to the beam dump, 568  
517 and the beam dump area itself. Thus, the faces of the 569  
518 spectrometer exposed to direct sources of radiation are 570  
519 the front, beam side, and the back walls. 571

520 Primary and scattered electrons lose a significant 572  
521 amount of energy as they traverse a material by pro- 573  
522 ducing a large number of lower energy photons through 574  
523 bremsstrahlung [30]. It is thus important to consider 575  
524 shielding materials that efficiently stop the latter as well. 576

525 Neutral particles have a higher penetration power 577  
526 than charged particles. They are attenuated in intensity 578  
527 as they traverse matter, but do not continuously lose en- 579  
528 ergy. Photons interact in materials almost exclusively 580  
529 with electrons surrounding the atom or by pair produc- 581  
530 tion in the field of the nucleus. The probability for an 582  
531 interaction depends on the atomic number of the ma- 583  
532 terial. Neutrons interact with atomic nuclei in a more 584  
533 complicated way. 585

534 An additional source of radiation is due to charged 586  
535 hadrons (e.g. protons, pions). However, the probabil- 587  
536 ity for producing hadron radiation is relatively low, and 588  
537 thus will be neglected here. The shielding is, neverthe- 589  
538 less, effective for charged hadrons. The front wall will, 590  
539 for instance, stop 1 GeV protons. 591

540 Fig. 18 shows a schematic of the SHMS shielding 592  
541 plan. The SHMS shield house is similar to the HMS 593

design, but has several new features due to additional 542  
requirements. For example, the space between the beam 543  
side shield wall and the beam pipe is limited at very for- 544  
ward angles, and in addition, the length of the SHMS 545  
detector stack and minimum distance between the back 546  
of the detector house to the hall wall requires a reduc- 547  
tion in thickness of the concrete shield wall. 548

549 Typical beam-target geometries were simulated using 550  
Monte Carlo techniques. Simulations were performed 551  
using the GEANT MCWORKS distribution, which in- 552  
cludes detailed physical and geometric descriptions of 553  
the experimental hall and simulates the physics pro- 554  
cesses using standard GEANT3 together with the DIN- 555  
REG nuclear fragmentation package. Hadronic inter- 556  
actions are treated using the DINREG package, which 557  
calculates the probability of such interactions using a 558  
database of photonuclear cross sections. For electron- 559  
nucleus interactions an “equivalent photon” representa- 560  
tion of the electron (or positron) is used. 561

562 In this simulation, the CEBAF beam electrons start 563  
564 1 m upstream of the target, strike it head-on along the 565  
566 cylindrical symmetry axis, and have no momentum 567  
568 component transverse to the beamline. The simulation 569  
570 also includes the beam pipe, target entrance and exit 571  
572 windows, and the entire geometry of Hall C, including 573  
574 all elements of the beam dump. The transmission of 575  
576 particles through the shielding materials was calculated 577  
578 as a function of the material thickness and the angle re- 579  
580 lative to the beam direction. 581

582 A limitation of the radiation studies is the lack of 583  
584 cross section data for low-energy neutrons. The accu- 585  
586 racy of the GEANT simulations was tested by bench- 587  
588 mark calculations using the MCNP code [31] with an 589  
590 isotropic neutron point source of 1 MeV located 1 m 591  
592 from the shield wall. The MCNP calculations sug- 593  
594 gest that 50 cm of concrete thermalizes most of the fast 595  
596 neutrons, and after 1 m practically no epithermal neu- 597  
598 trons remain. The thermalized neutrons can be captured 599  
600 by a 1 cm Boron layer. In reality, however, the neu- 601  
602 tron spectrum also includes higher energy neutrons, for 603  
604 instance produced by electrons interacting in the con- 605  
606 crete, and thus the actual amount of material for the 607  
608 walls exposed to the primary sources of radiation has 609  
610 to be thicker. A simple transmission calculation using 611  
612 GEANT4 for incident neutron beams of energies be- 613  
614 tween 1 and 10 MeV suggests that a thickness 150 cm of 615  
616 concrete is sufficient to stop the majority of low-energy 617  
618 neutrons [32]. 619

620 The SHMS shielding model is composed of standard 621  
622 concrete ( $\rho = 2.4 \text{ g/cm}^3$ ). The thickness of the wall in 623  
624 front of the detector and electronics rooms is 200 cm, 625  
626 to shield from the primary radiation source around the 627

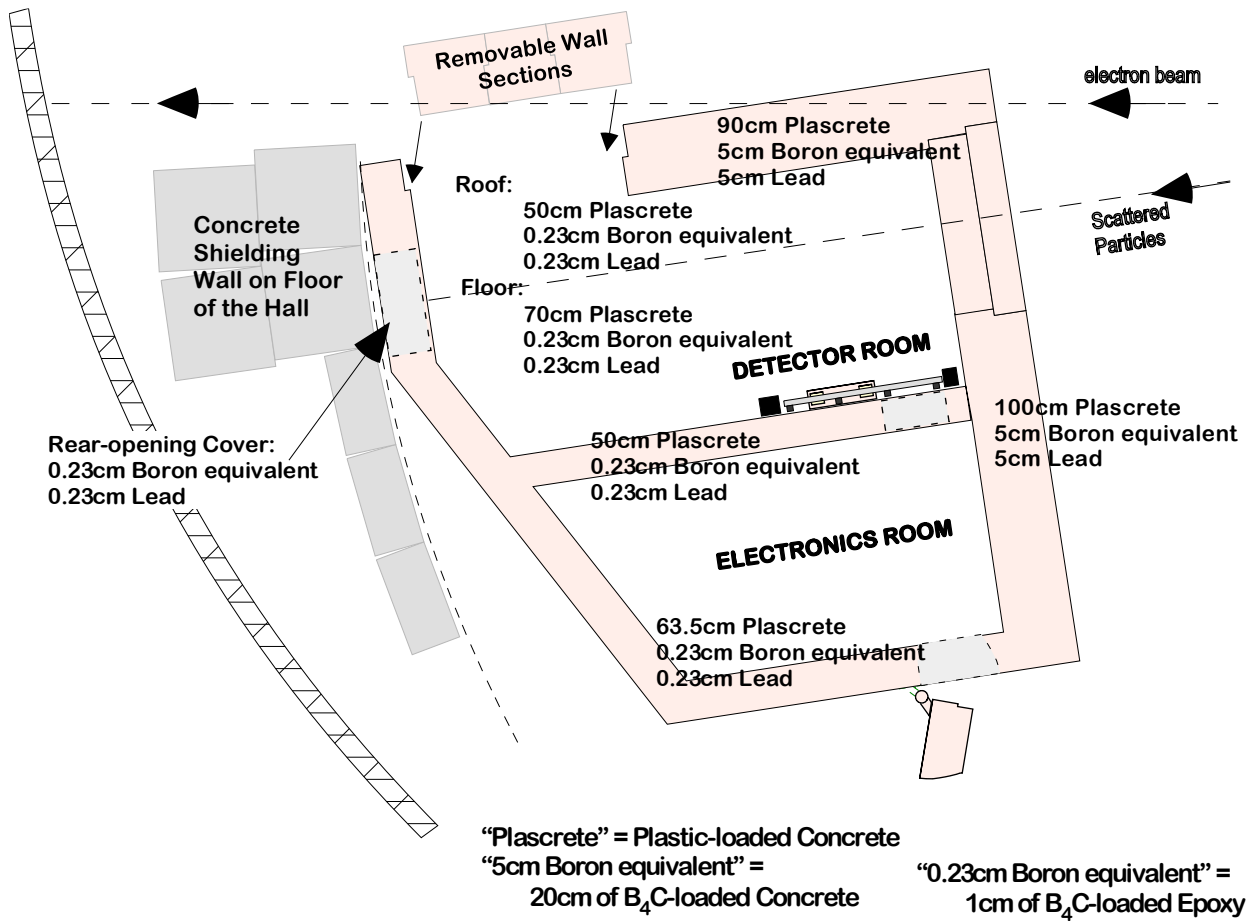


Figure 18: Plan View of the SHMS Shield House showing the layout, thickness, and composition of the walls.

594 target. Figure 19 shows the surviving background flux  
 595 for varying front wall concrete thicknesses. The results  
 596 are normalized to the background flux in the HMS at  
 597 20°. This angle was chosen as experiments in Hall C  
 598 have shown that electronics problems seem to dominate  
 599 at lower angles [33]. The simulation results suggest that  
 600 200 cm of concrete reduces the total flux to half of the  
 601 HMS at 20°.

602 Figure 20 shows the energy spectra for surviving photons  
 603 and neutrons with varying front wall thickness. In  
 604 order to optimize the shielding, these secondary particles  
 605 have to be absorbed as well. Our assumption on radiation  
 606 damage is that photons below 100 keV will not be a  
 607 significant source of dislocations in the lattice of the  
 608 electronics components, while neutrons will cause radiation  
 609 damage down to thermal energies. Adding lead to the  
 610 concrete wall reduces the photon flux significantly,  
 611 but it does not help for neutrons. On the other hand,  
 612 the boron reduces the flux of very low energy neutrons.

613 Assuming that low energy photons and neutrons cause a  
 614 significant fraction of the radiation damage, then adding  
 615 the relevant material would be important.

616 The thickness of the beam-side wall (shielding from  
 617 an extended source, the beamline) is constrained by the  
 618 clearance with the detector stack inside the enclosure  
 619 and the beamline at small angles. Conservatively assuming  
 620 a clearance of 5 cm between detector stack and the  
 621 shield wall, the total concrete wall thickness is limited  
 622 to 105 cm. A 90 cm concrete wall combined with a  
 623 5 cm boron and 5 cm lead layer provides the optimal  
 624 shielding configuration. Adding boron is not much different  
 625 from adding (or replacing) concrete, but in addition  
 626 it captures thermal neutrons.

627 The majority of charged particles are stopped by the  
 628 outer walls of the spectrometer shield house. An additional  
 629 source of radiation may be created from particles entering  
 630 the enclosure through the magnets. In order to protect  
 631 the electronics further, an intermediate wall was

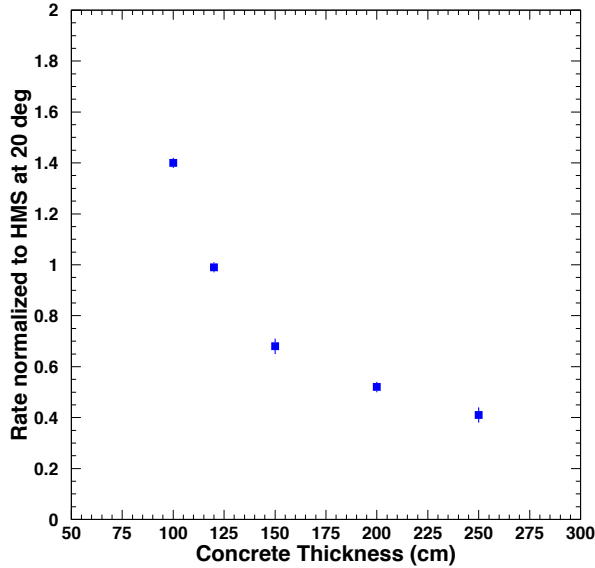


Figure 19: The normalized background rate vs. front wall thickness. The rates are normalized to those found in the HMS at 20°.

632 installed between the detector and electronics rooms.  
 633 Figure 21 shows the normalized rate as the thickness of  
 634 this intermediate wall is varied. This suggests that the  
 635 optimal configuration is provided by a concrete thick-  
 636 ness of 80–100 cm<sup>1</sup>. Further details on shielding con-  
 637 figurations investigated and their optimization can be  
 638 found in Ref. [29].

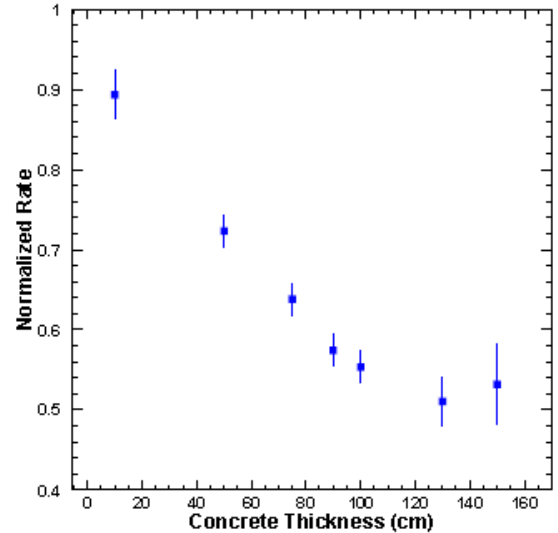


Figure 21: The normalized rate versus the intermediate concrete wall thickness.

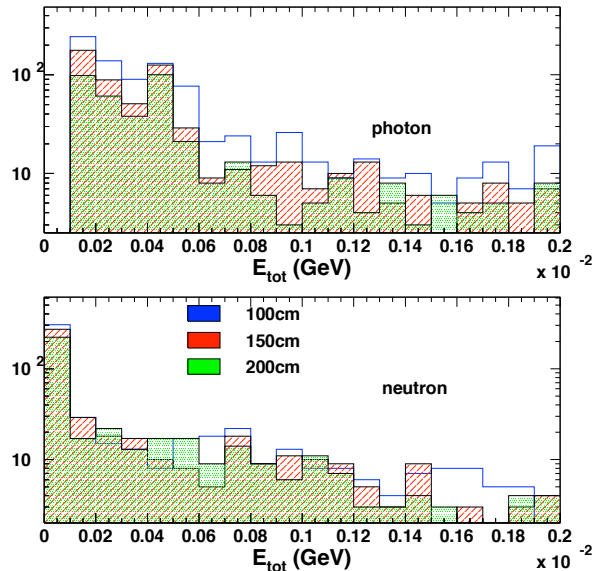


Figure 20: The outgoing particle spectrum, which is soft (< 10 MeV).

639 The hydrogen-rich concrete walls function as a  
 640 shield, an absorber, and a neutron moderator, and are  
 641 thus placed on the outside of all faces of the shield  
 642 house. On the other hand, the ordering of lead and boron  
 643 to shield against the photon and neutron flux may, at first  
 644 glance, not be obvious, and is discussed in detail below.

645 The incoming photon flux has two components: ex-  
 646 ternally produced photons and bremsstrahlung photons  
 647 produced by electrons in the twenty radiation lengths of  
 648 concrete. The simulations have shown that the outgoing  
 649 photon spectrum is soft (<10 MeV). Placing a lead layer  
 650 after the concrete is essential to suppress this low energy  
 651 photon flux. The  $(\gamma, n)$  reaction in lead is not a problem.  
 652 The threshold for the reaction is given by the neutron  
 653 binding energy ( $\sim 8$  MeV). At higher energies, the cross  
 654 sections are in the mbarn range [34]. Even disregarding  
 655 the low cross section, however, it is not clear that this  
 656 reaction contributes to the irradiation of the electronics,  
 657 because a high energy photon is replaced by a low energy  
 658 (but not thermal) neutron.

<sup>1</sup>Note that a minimum wall thickness of 50 cm is needed to provide support for the roof of the shield house

659 The incoming neutron flux also has two components.  
 660 Neutrons from excited nuclei will typically not exceed  
 661 10 MeV. The other neutrons are produced through direct  
 662 interactions with only one nucleon in the nucleus.  
 663 These will have high energies, but the flux is low. As  
 664 shown by the MCNP calculation, which has reliable low  
 665 energy neutron cross sections, 0.5 m of concrete almost  
 666 fully thermalizes 1 MeV neutrons. Thus, 2 m of concrete  
 667 should be sufficient to thermalize the first component.  
 668 Some of these will be captured in the concrete, but to  
 669 eliminate the surviving thermal neutrons a layer of boron  
 670 is needed. There are two relevant reaction channels:  $(n, \gamma)$   
 671 and  $(n, \alpha\gamma)$ . The former produces high energy photons,  
 672 but the cross section is relatively small. The latter produces  
 673 a 0.48 MeV photon for every captured neutron. The thermal  
 674 cross section is about 10 kbarn, and even at 1 MeV it is  
 675 still in the barn range. The majority of neutrons can thus  
 676 be expected to be captured in a sufficiently thick boron  
 677 layer. An optimal shielding configuration would also stop  
 678 these photons produced in the capture. At 0.48 MeV, the  
 679 photoelectric effect and Compton scattering contribute about  
 680 equally to the attenuation in lead. Photons from the latter  
 681 will also need to be absorbed.  
 682

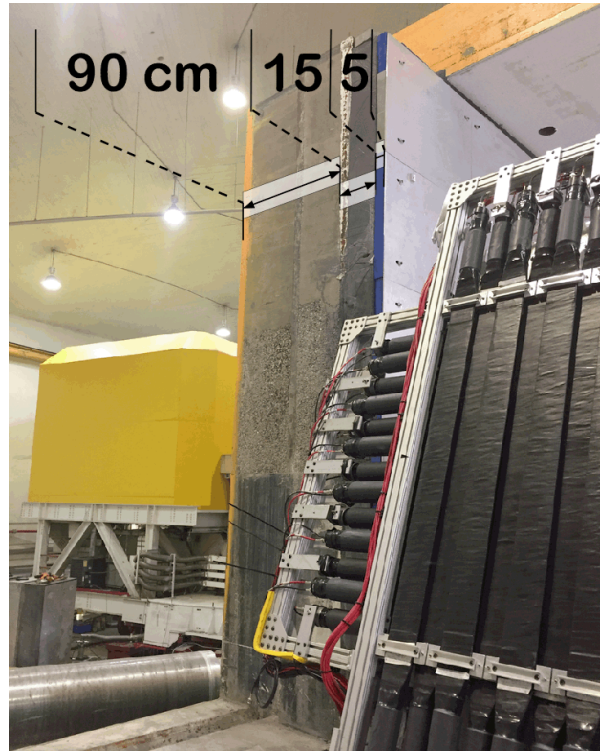
683 Thus, placing the lead in front of the boron layer has  
 684 limited benefit. It will not affect the neutron flux, but  
 685 will create an additional source of photons. The more lead  
 686 one places after the boron, the more efficiently these  
 687 photons will be suppressed. From the point of view of  
 688 stopping bremsstrahlung photons, the order of boron and  
 689 lead layers does not matter. Thus, all lead should be  
 690 placed after the boron.

691 Fig. 22 is a photograph showing the resulting multi-  
 692 layered shielding in one of the SHMS shield house walls.  
 693 The ceiling, floor, and other walls have similar  
 694 compositions but varying dimensions as shown in  
 695 Fig. 18. Details about the development of custom  
 696 concrete material containing boron can be found in  
 697 Ref. [35].

698 In summary, the SHMS shielding consists of concrete  
 699 walls to moderate and attenuate particles. Low energy  
 700 (thermal) neutrons are absorbed in a boron layer inside  
 701 the concrete. Low energy and 0.5 MeV capture photons  
 702 are absorbed in lead. With this design, the rates at  
 703 forward angles of  $5.5^\circ$  are estimated to be less than  
 704 70% of the design goal (HMS at  $20^\circ$ ) in the detector  
 705 room and below 50% in the electronics room.

### 706 3.3. Scintillator Trigger Hodoscopes

707 The SHMS hodoscope system provides a clean trigger  
 708 and trigger time information as well as the definition  
 709 of the detector package fiducial area, required



710 Figure 22: Photograph of the SHMS beam-side shield wall in cross-  
 711 section view, showing the layers of different materials making up the  
 712 wall.

713 for physics cross section measurements. The system is  
 714 composed of four separate planes of detector paddles:  
 715 S1X and S1Y located immediately after the second drift  
 716 chamber and S2X and S2Y approximately 2.6 m away  
 along the z direction. The S1X, S1Y, and S2X planes  
 were built using thin scintillator paddles while S2Y uses  
 quartz bars.

#### 717 3.3.1. Design and Construction

718 The overall dimensions and granularity of the three  
 719 scintillator planes were driven by the Monte Carlo sim-  
 720 ulations of the SHMS acceptance. The S1X and S1Y  
 721 planes cover a  $1000 \times 980 \text{ mm}^2$  area while the S2X plane  
 722 covers  $1100 \times 1335 \text{ mm}^2$ . Further design constraints  
 723 for this detector include high ( $\geq 99\%$ ) detection effi-  
 724 ciency, position independent along the scintillator pad-  
 725 dle; good time resolution ( $\sim 100 \text{ ps}$ ) and high rate ca-  
 726 pability ( $\sim 1 \text{ MHz/cm}$ ). As the detector's lifetime is as-  
 727 sumed to be a decade or more stable, cost effective, and  
 728 readily available materials and readout chain were used.

729 To meet the requirements listed above the SHMS Ho-  
 730 doscope was built as a series of arrays (planes) of plastic  
 731 scintillator paddles. The S1X and S1Y planes have 13

1000x80 mm paddles each, while the S2X plane has 14 1100x100 mm paddles. For each of the three scintillator planes the paddles were staggered by 7 mm and overlapped by 5 mm. To minimize the impact of the scintillators on downstream detectors and also to ensure good timing resolution the thickness of paddles was 5 mm.

The scintillator material used was Rexon RP-408. The paddles were wrapped by the manufacturer with millipore paper, aluminum foil, and 2" wide electrical tape. The transition between the thin scintillator material and the photomultiplier (PMT) tubes used for readout was done using a Lucite fishtail-shaped light guide. As the glued joint between the scintillator paddle and the light guide is rather fragile (5x80 and 5x100 mm joints) aluminum "splints" were used to reinforce it. The PMT to fishtail joint was originally wrapped with 2" tape as well and light-leak tested; subsequently this wrapping was reinforced with TEFLON tape and a 3" heat-shrink sleeve.

Each scintillator paddle is read at both ends by PMTs glued to the fishtail using optical glue (BC-600) matching the index of refraction of the Lucite. A combination of Photonis XP 2262 and ET 9214B 2" tubes were used. Both models have 12-stage amplification and their maximum photocathode sensitivity is in the blue-green range. The typical gain is  $3 \times 10^7$ . Gains were measured as a function of high voltage during the construction and the whole hodoscope was gain matched *in situ* once installed in SHMS.

### 3.4. Quartz-bar Trigger Hodoscope

The SHMS hodoscope quartz plane was designed to help with neutral background rejection in the 12 GeV high-rate environment. It operates on the principle of Cherenkov light production by electrically charged particles. It is one of the four hodoscope planes that form the basic 3 out of 4 trigger in the SHMS. In what follows the design and construction of this detector will be presented as well as its performance with electron beam in Hall C.

#### 3.4.1. Design and Construction

The design and construction of the SHMS hodoscope quartz plane was done by the North Carolina A&T group led by Abdellah Ahmidouch and Samuel Danagoulian. Quartz bars of  $2.5 \times 5.5 \times 125$  cm<sup>3</sup> dimensions with an index of refraction of 1.5 were chosen. The Cherenkov light produced by electrically charged particles is detected by UV-glass window PMTs (model ET9814WB) quartz window ET9814QB photomultiplier tubes optically coupled to the quartz bars through

RTV615 silicon rubber of 50  $\mu$ m thickness. There are 16 bars in use in the hodoscope quartz plane are staggered so that there is an overlap between adjacent bars of 0.5 cm. The quartz plane frame allows for more bars to be added.

### 3.5. Drift Chambers

#### 3.5.1. Design

The SHMS horizontal drift chambers provide information to determine the trajectory of charged particles passing through the detector stack. The drift chamber package consists of two horizontal drift chambers separated by a distance of 1.1 m and oriented in the detector stack such that the sense wires planes are perpendicular to the central ray. Each chamber consists of a stack of six wire planes providing information on the track position along a single dimension in the plane of the wires and perpendicular to the wire orientations to better than 250  $\mu$ m. The perpendicular distance of the track relative to the wire is determined from the time of the signal produced by the ionization electrons as they drift from their production point to the wire in an electric field of approximately 3700 V/cm.

The basic design and construction technique is based on that of previous successful chambers built for the Hall C 6 GeV program, which have been shown to reach the resolutions and particle rate specifications of the SHMS. The open layout design consists of a stack of alternating wire and cathode foil planes; each plane consisting of 1/8" thick printed circuit board (PCB). These are sandwiched between a pair of aluminum plates on the outside, which provide both the overall structural support and the precise alignment of each board via dowel pins at the corners. Just inside each pair of plates is a fiberglass board with the central area cut out and covered with a vacuum stretched film of aluminized Mylar, which provides the gas window. These are sealed to prevent gas leakage via an o-ring around the gas fitting through-hole on the inside of the plate.

Each chamber consists of two identical half chambers separated by a fiberglass mid-plane, which also supports the amplifier discriminator cards required for the sense wire readout. To minimize the production costs, only two unique PCB types were designed: an X-plane with wires oriented horizontally (left panel of Figure 23), and a U-plane with wires oriented at +60° relative the X-plane (right panel of Figure 23). All other plane orientations are generated by rotations of these two basic board types. For instance, the boards are designed such that a rotation of 180° in-plane about an axis through the center of the board produces boards with wires of



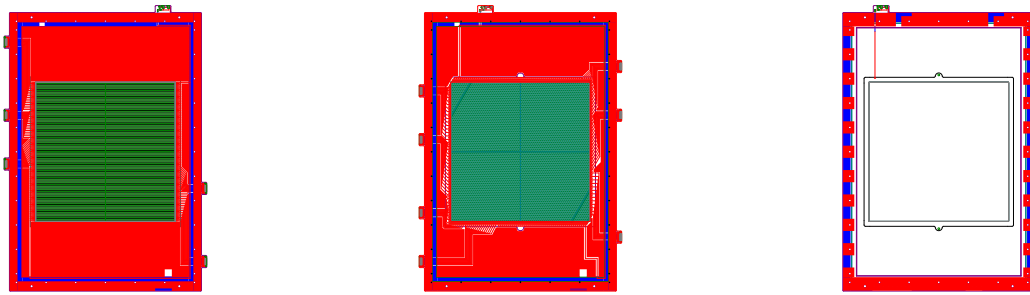


Figure 23: Technical drawings of the PCBs for the X-plane (Left), U-plane (Middle), and K-plane (Right).

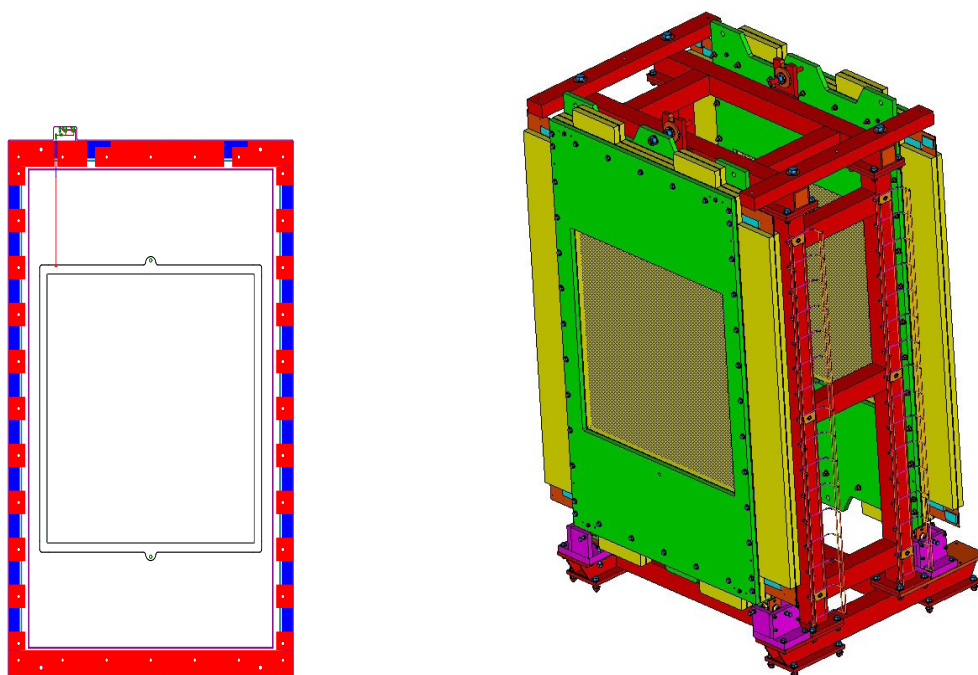


Figure 24: (Left) Technical drawing of cathode (k-plane) PCB. (Right) Technical drawing of the two drift chambers mounted in the Aluminum frame such that the scattered particles would enter the chamber from the left. The chambers are fixed to the frame by a bolt through the top tab on the chamber plate which allows for fine adjustments to the pitch. The downstream chamber (DC2) is mounted in the reverse orientation from the upstream chamber (DC1).

831 the same orientation, but shifted by 1/2 cell width, thus  
 832 allowing the resolution of left/right ambiguities. Ro-  
 833 tation of Figure 23 such that the top becomes the bot-  
 834 tom produces the X' and U' orientations. The V and V'  
 835 boards with wire orientation of  $-60^\circ$  relative to the X-  
 836 plane are produced by a rotation of the U and U' boards  
 837 of  $180^\circ$  into the page about a vertical axis through the  
 838 center of the board. Each half chamber has three planes  
 839 with the first half consisting of (U, U', X) and the second  
 840 half consisting of (X', V', V). The first chamber is ori-  
 841 ented in the SHMS frame such that the board ordering

842 as seen by particle traversing the spectrometer is (U, U',  
 843 X, X', V', V), while for the second chamber the order-  
 844 ing is reversed (V, V', X', X, U', U). A drawing showing  
 845 the chambers mounted in the frame is presented in Fig-  
 846 ure 24.

847 The drift gas (50/50 mixture of Ethane/Argon in pro-  
 848 duction mode) flows across each board through holes  
 849 in the cathode planes (k-planes) alternating from top to  
 850 bottom. A technical drawing of a k-plane is presented  
 851 in Figure 23. The overall dimensions of the wire cham-  
 852 bers are driven by the desired active area for particles at

853 the focal plane of the SHMS; this has been set at 80 cm 897  
 854 x 80 cm. The active area of each wire plane consists 898  
 855 of alternating 20  $\mu\text{m}$  diameter gold tungsten sense wires 899  
 856 and 80  $\mu\text{m}$  diameter copper plated beryllium field wires 900  
 857 separated by 0.5 cm. Each wire plane is sandwiched be-  
 858 tween a pair of cathode planes with the cathode surfaces  
 859 consisting of 5 mil thick stretched foils of copper plated  
 860 Kapton.

### 861 3.5.2. Calibration

862 As charged particles traverse the drift chambers and  
 863 ionize the gas, free electrons from the ionized gas drift  
 864 towards the sense wires in the chamber. This process  
 865 produces a measurable current signal in the sense wire,  
 866 this signal is pre-amplified and read out by 16-channel  
 867 input discriminators. The discriminators produce logic  
 868 signals that are sent to the TDC which registers the time  
 869 at which this signal arrives. This signal is utilised to de-  
 870 termine the drift time, the time taken for the free elec-  
 871 trons to drift to the sense wire, via -

$$t_D = (t_{meas} - t_{REF}) - [(t_{wire} + t_{cable}) - t_{REF}]. \quad (3)$$

872 In Eqn. 3  $t_{meas}$  is the time recorded by the TDC and  
 873 the term  $t_{wire} + t_{cable}$  is the time it takes the signal to  
 874 propagate across the sense wire, through the cable and  
 875 into the TDC if the track were to pass directly through  
 876 the sense wire. All of these times are measured relative to  
 877 a common reference time,  $t_{REF}$ . When combined with  
 878 information about the position of wires in each cham-  
 879 ber, this quantity can provide coarse track information.  
 880 However, this can be further refined by converting the  
 881 drift time to a drift distance. This is accomplished by  
 882 utilising time-to-distance maps for the detector. The  
 883 purpose of the drift chamber calibration procedure is to  
 884 produce these per-plane look-up tables.

885 A single cell<sup>2</sup> will see a uniform distribution of events  
 886 through it. For a collection of events illuminating all  
 887 cells in any given wire plane, a drift time distribution  
 888 can be obtained. This distribution can be averaged over  
 889 an entire group (up to 16 wires per discriminator card)  
 890 or over the entire plane. Associated with each drift time  
 891 distribution is a time,  $t_0$ , which corresponds to the time  
 892 at which ionized particles come into contact with the  
 893 wire. If this value is non-zero, this is the value by which  
 894 all drift times must be shifted in order to assure that  $t_0 =$   
 895  $0 \text{ ns}$ . All subsequent times in each spectra are measured  
 896 relative to this time. To determine  $t_0$  for a plane, the

<sup>2</sup>A cell is one sense wire surrounded by field wires such that the sense wire is at the center and the field wires are at the corners

weighted average of all  $t_0$  wire values in that plane is utilised.

From the drift time spectra,  $F(t)$ , the drift distance,  $D(t)$ , spectra can be determined via -

$$D(t) = D_{Max} \frac{\int_{t_0}^t F(t) dt}{\int_{t_0}^{t_{Max}} F(t) dt} \quad (4)$$

901 where  $D_{Max}$  is the maximum possible drift distance  
 902 (0.5 cm, half a cell),  $t_{Max}$  is the maximum drift time and  
 903  $t$  is the measured drift time. Note that  $D(t_0) = 0 \text{ cm}$  and  
 904  $D(t_{Max}) = 0.5 \text{ cm}$ . Due to the finite resolution of the  
 905 TDC, the integrals in Eqn. 4 become sums over finite  
 906 bin widths and Eqn. 4 can be re-written as -

$$\frac{1}{N_{Tot}} \sum_{\text{bin}(t_0)}^{\text{bin}(t_0+T)} F(t), \quad (5)$$

907 which is simply a ratio of the sum of bin contents  
 908 (up to some drift time,  $T$ ) over all bin contents (up to a  
 909 maximum,  $t_{max}$ ),  $N_{tot}$ . The results of the calibration are  
 910 per-plane look up tables which utilise this ratio to map  
 911 any given drift time to a drift distance for that plane.  
 912 When properly calibrated, this should result in a flat,  
 913 uniform distribution of drift distances for each chamber.  
 914 An example drift distance spectra, showing the pre and  
 915 post calibration distributions can be seen in Fig. 25.

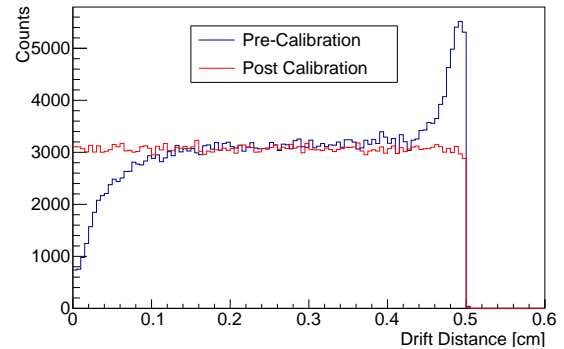


Figure 25: Example drift distance distributions for the SHMS drift chambers before (blue) and after (red) a successful calibration.

## 916 3.6. Heavy-Gas Cherenkov Counter

### 917 3.6.1. Design

918 The SHMS Heavy-Gas Cherenkov detector (HGC) is  
 919 a threshold-type Cherenkov detector, designed to sepa-  
 920 rate charged  $\pi$  and  $K$  over most of the SHMS operating  
 921 momentum range, 3–11 GeV/c.  $\text{C}_4\text{F}_{10}$  radiator gas at

922 1 atm, with an index of refraction of  $n=1.00143$  at standard  
 923 temperature [36], allows  $\pi^\pm$  to produce abundant Cherenkov  
 924 light above 3 GeV/c momentum, while  $K^\pm$  remain below Cherenkov  
 925 threshold until about 7 GeV/c. Optimal  $\pi/K$  separation at higher momenta  
 926 requires a reduction in the gas pressure, down to 0.3 atm at  
 927 11 GeV/c.  
 928

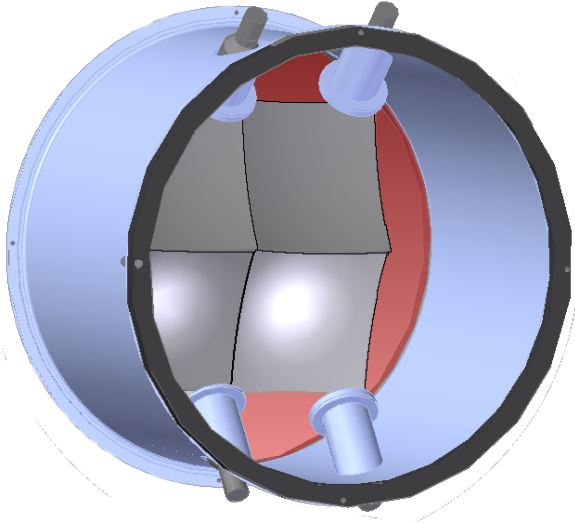


Figure 26: 3D-CAD rendering of the Heavy Gas Cherenkov Detector.

929 A schematic view of the detector is shown in Fig. 26.  
 930 The SHMS focal plane is subtended by four  $55 \times 60$  cm  
 931  $0.3$  cm thick glass mirrors, which reflect the Cherenkov  
 932 radiation to four Hamamatsu R1584  $12.5$  cm diameter  
 933 photomultiplier tubes located above and below the particle  
 934 envelope. The mirrors and gas are enclosed in a  
 935 cylindrical aluminum tank of  $164.9$  cm inner diameter and  
 936  $113.5$  cm length, with entrance and exit windows of  
 937  $0.102$  cm thickness 2024 T-4 aluminum alloy [37]. The  
 938 vessel is sufficiently strong to be pumped to vacuum before  
 939 introducing the radiator gas, avoiding the need to purge  
 940 when filling. A unique aspect of the detector is the  
 941 placement of the photomultipliers outside the gas  
 942 envelope, viewing the enclosure through  $1.00$  cm thick  
 943 Corning 7980 quartz windows. This allows the gas  
 944 enclosure to be smaller in diameter than would otherwise  
 945 be possible, as the full length of the PMT and base no  
 946 longer need to be fully within the diameter of the vessel.  
 947 It also makes the PMTs available for servicing without  
 948 venting the gas.

949 The mirrors are inexpensive, having been produced  
 950 by the slumping process [38]. As a result, they deviate  
 951 from the desired  $110$  cm radius of curvature with

a slightly oblate shape [39]. However, the Cherenkov  
 952 cone on the mirrors for  $3-7$  GeV/c  $\pi^\pm$  in  $C_4F_{10}$  is  $7-10$   
 953 cm in diameter, so optical quality mirrors are not  
 954 required for this application. The UV wavelength  
 955 characteristics of the respective optical components are  
 956 relatively well matched.  $C_4F_{10}$  has good transmittance  
 957 down to  $\sim 160$  nm [36]. The quartz viewing windows  
 958 provide  $>88\%$  transmission down to  $200$  nm, including  
 959 the  $\sim 10\%$  loss due to surface reflection [40], and the  
 960 optical glass face PMTs have  $70\%$  of their peak quantum  
 961 efficiency at  $200$  nm (peak at  $350$  nm) [41]. Accordingly,  
 962 the mirror reflectivity was optimized for  $>90\%$  at  
 963  $270$  nm, and  $75\%$  at  $200$  nm [42].  
 964

### 965 3.6.2. Calibration

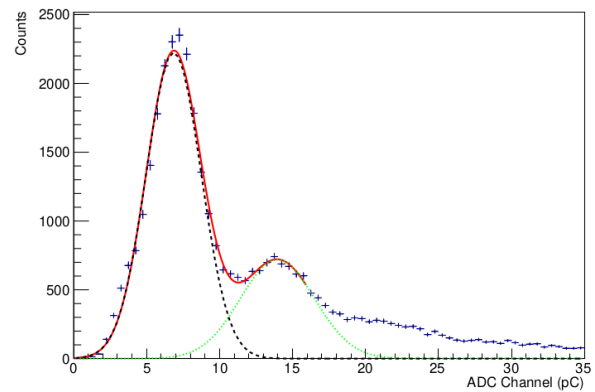


Figure 27: The isolated 1 (dashed black) and 2 (dotted green) photoelectron peaks for the lower right PMT #2, and their sum (solid red), obtained by selecting adjacent mirror light from the upper right quadrant #4. Three such adjacent mirror plots are obtained for each PMT. The light from the mirror closest to the PMT is far more intense, with too few SPE events available to yield a reliable calibration.

966 The goal of the SHMS HGC calibration procedure  
 967 is to generate an accurate translation from raw FADC  
 968 channels (or charge in pC) to the number of photoelectrons  
 969 emitted from the cathode surface of the PMT (NPE). This  
 970 is achieved by isolating the single photoelectron (SPE)  
 971 peak, yielding a calibration, and then verified by examining  
 972 the regular spacing of the first few photoelectron  
 973 contributions in the ADC spectrum.

974 To isolate the SPE peak, tracking cuts are applied  
 975 to the data to analyze what each PMT detected from  
 976 charged particles traversing each mirror quadrant. As a  
 977 charged particle passes through a mirror quadrant, the  
 978 produced Cherenkov cone allows some light to be  
 979 incident on adjacent mirrors. As each mirror is focused  
 980 on a single PMT, one PMT will receive most of the  
 981 produced light while the other three receive much  
 982 smaller amounts. This small signal allows the SPE peak to be

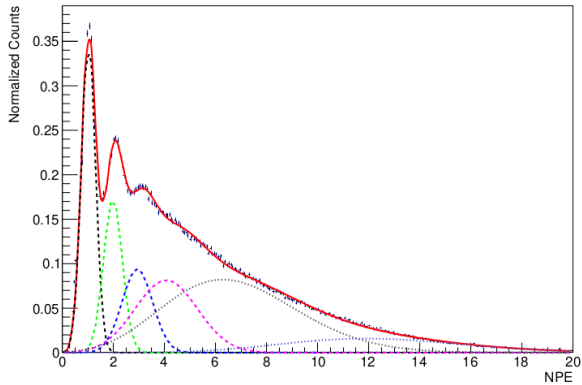


Figure 28: Results from a successful calibration of the HGC. Shown is the NPE distribution of the lower right PMT #2 obtained from all four mirrors. The 1, 2, and 3 NPE peaks are shown, indicated by dashed Gaussian distributions. Two Poisson distributions (dotted lines) provide a good description of the nearest mirror events with large NPE, and a broad Gaussian near 4 NPE fills in the gap with the lower NPE peaks. The sum of all 6 distributions is shown as the solid red curve.

measured, yielding a reliable calibration. To select this adjacent mirror light, cuts (based on the physical dimensions of the mirrors) are placed on the tracked coordinates of the charged particles, extrapolated to the HGC mirror plane,

$$x_{\text{HGC}} = x_{\text{Focal Plane}} + x'_{\text{Focal Plane}} \cdot z_{\text{HGC}} \quad (6)$$

$$y_{\text{HGC}} = y_{\text{Focal Plane}} + y'_{\text{Focal Plane}} \cdot z_{\text{HGC}}, \quad (7)$$

where  $z_{\text{HGC}} = 156.27$  cm is the distance from the focal plane to the HGC mirror plane. The coordinate axis for the HGC is the convention used in charged particle transport in dispersive magnetic systems. The  $x$ -axis is the direction of increasing particle momentum, the  $z$ -axis is the direction of particle travel through the spectrometer, and the  $y$ -axis is deduced from  $z \times x$ . Additionally, timing cuts are applied to the HGC data, collected using the high resolution pulse time setting in the FADC250's FPGA. The time measured corresponds to the time it takes a pulse to reach half of its maximum amplitude after passing a pedestal threshold of 5 mV. Lastly, a cut on particle velocity,  $\beta$ , is also applied, obtained from the tracking algorithm.

An example of a completed calibration is shown in Figs. 27, 28. For this run, the HGC was filled with  $\text{C}_4\text{F}_{10}$  at 1 atm, and the SHMS central momentum was 2.583 GeV/c, with polarity set to detect positively-charged particles. Cherenkov radiation is produced by  $\pi^+$  traversing the HGC with momentum  $> 2.598$  GeV/c. This can occur only for  $\delta > +0.5\%$ , which corresponds roughly to the bottom half of the HGC. Subthreshold  $\pi^+$  with  $\delta < +0.5\%$ , as well as  $K^+$  and  $p$ , may produce low-

level light in the HGC via knock-on electron emission and scintillation in the radiator gas. The adjacent mirror cuts described above produce a clear SPE peak in Fig. 27, which provides the main source of calibration information.

A histogram of light collected in one PMT from all four mirrors is shown in Fig. 28, where the average number of photo electrons detected per event is higher due to the more intense light from the closest mirror. In this figure, the spectrum is fit with a sum of four Gaussian and two Poisson distributions, shown by the solid red line.

An inherent systematic uncertainty is present in the HGC calibration due to statistical errors in determining the location of the SPE peak in the various mirror quadrants. This uncertainty was quantified by recording the locations of the SPE across several runs, for the different adjacent mirror combinations for each PMT, as well as by varying the contribution of the higher PE tail extending underneath the SPE peak, as in Figs. 27, 28. The systematic uncertainty in the calibration is taken to be the root mean square of this set of values, giving  $\pm 1.5\%$ . It should be noted this uncertainty is somewhat larger than the statistical uncertainty of the SPE peak, which is typically 0.2 to 0.6%.

### 3.6.3. Gain Matching

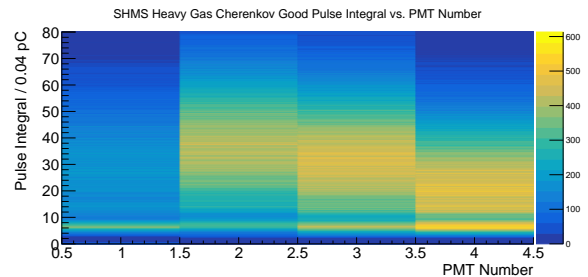


Figure 29: Demonstration of gain matching between PMTs by the alignment of the single photoelectron, indicated by the yellow band about 6.825 pC. The horizontal axis refers to PMT number, the vertical axis to Pulse Integral in bins of 0.04 pC. The color axis represents the number of events filling each bin.

To ensure each PMT has an identical response to incident light, the voltages of each PMT were adjusted to obtain accurate gain matching. This can be seen in Fig. 29 by the alignment of the SPE at approximately 6.825 pC, represented by the common band across all four PMTs at that value. Additionally, the gain of each PMT was tested by the manufacturer, Hamamatsu, and at Jefferson Lab. The results of each test are shown in Table 3. The Hamamatsu data were taken directly at

2000 V in a highly controlled environment, thus leading to small uncertainty in the gain which was not quoted. The Jefferson Lab measurement were also taken at 2000 V, but taken in an experimental environment. This gives rise to an uncertainty in the JLab gain data on the order of 1%, larger than the Hamamatsu data.

### 3.7. Noble-Gas Cherenkov Counter

#### 3.7.1. Design

Analyzing momenta up to 11 GeV/c at scattering angles from  $5.5^\circ$  to  $40.0^\circ$ , the SHMS will reach kinematic regions in which the pion background rate dominates the scattered electron rate by more than 1000:1. The suppression of these anticipated pion backgrounds while maintaining efficient identification of electrons is therefore one of the main duties of the SHMS detector elements and the SHMS Noble Gas Cherenkov Detector shoulders a large portion of this particle identification burden. The design of the noble gas threshold Cherenkov detector is such that it will meet these twin goals of suppression and identification. The main goal of the detector is to distinguish between electrons and pions with momenta between 6 GeV/c and 11 GeV/c. Operating at 1 atm it will use a mixture of Argon and Neon as the radiator: pure Argon with an index of refraction  $n=1.00028201$  at a SHMS momenta of 6 GeV/c and pure Neon with an index of refraction  $n=1.000066102$  at 11 GeV/c and a mixture of Argon and Neon at intermediate momenta.

The SHMS NGC design was restricted by the available space and the need to have good discrimination at the highest momenta. The number of photoelectrons is maximized in this design by the use of quartz window PMTs and mirrors with excellent reflectivity well into the UV.

The NGC consists of the four main elements: 1) a light tight box with thin entrance and exit windows designed to operate at 1 atm; 2) four spherical mirrors held in a rigid frame; 3) four 5 inch quartz window photo-multipliers (PMTs) and 4) the radiator gas.

PMT	JLab Gain	Hamamatsu Gain
PMT 1	$(2.79 \pm 0.01) \times 10^7$	$0.969 \times 10^7$
PMT 2	$(6.55 \pm 0.04) \times 10^7$	$3.60 \times 10^7$
PMT 3	$(7.12 \pm 0.05) \times 10^7$	$5.79 \times 10^7$
PMT 4	$(5.35 \pm 0.04) \times 10^7$	$3.20 \times 10^7$

Table 3: Gain characteristics for the PMTs in the HGC. Two measurements were performed, one at Jefferson Lab in an experimental setting, and one by the manufacturer Hamamatsu. The set voltage for the gain measurements is 2000 V for each PMT.

The tank was fabricated with an internal rigid aluminum t-slot frame and thin aluminum walls welded together and has an active length of 2 m along the beam direction and approximately 90 cm perpendicular to the beam direction. The main access is provided through a large ‘door’, and four small panels provide modest access to the PMTs. The tank has feedthroughs for gas management as well as for HV and signal cables. The interior was painted with a black flat paint to prevent the reflection of light from cosmic rays or hall background. Thin entrance and exit windows made of two layers of 2 mils of the Dupont product Tedlar  $(\text{CH}_2\text{CHCl})_n$  are also present. The PMTs were positioned outside the active area of the scattered particles, achieved by a  $15^\circ$  tilt of the mirrors.

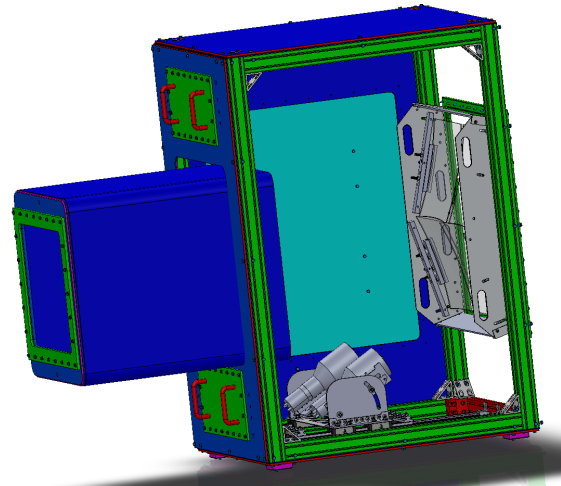


Figure 30: Sketch of the NGC tank. This view is possible as one panel is removed. Note the PMT mounting system is different than shown here.

Four spherical thin glass mirrors of radius 135 cm, square in shape with edges of 43 cm focus the Cherenkov light onto the PMTs. The glass blanks were manufactured by Rayotek Scientific [43] from borosilicate glass of 3 mm thickness by slumping over a polished steel mold and then cutting to dimensions. Simulations showed a reduction of collection efficiency due to incoming photon losses at the exposed edges of the mirror. As such, the edges were bevelled away from the active surface to minimize scattering from these edges.

The final batch of the glass blanks was shipped to Apex Metrology Solutions of Fort Wayne for CMM shape scanning measurements. Apex’s measurements were performed on a grid of 1806 points. The data were fitted with spherical, conical and elliptical fit functions

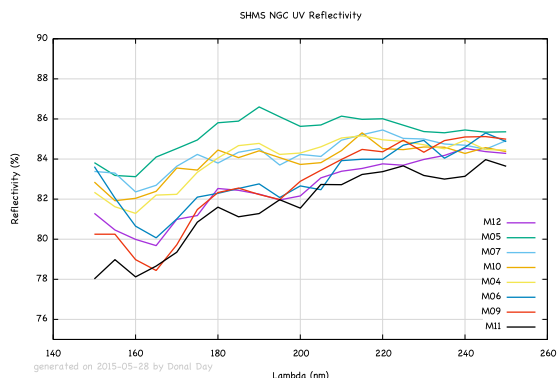


Figure 31: The UV measured reflectivity of the finished mirrors, coated at CERN which is no less than 78% at 150 nm. Between 250 nm and 600 nm the reflectivity rises to almost 90%.



Figure 32: Frame with mirrors about to be moved into tank.

1115 for each mirror. Though the elliptical fit described the  
 1116 surface slightly better than the spherical fit, the updated  
 1117 simulation with the real measured parameters showed  
 1118 almost no difference in the collection efficiency between  
 1119 the two. In addition the same fitting was performed for  
 1120 5 selected locations on the mirror: entire mirror, the  
 1121 center, and 4 quadrants. Based on the spherical fit re-  
 1122 sults “best” mirrors and “best” corners for each mirror  
 1123 were identified. The 4 mirrors come together and over-  
 1124 lap at the center of the acceptance where a majority of  
 1125 the scattered electrons are focused. Care was then made  
 1126 to select among the best 4 glass pieces their best corners  
 1127 so as to be in the overlap region. The radii of the 4 best  
 1128 pieces of glass, from fitting, was found to never vary by  
 1129 more than 2 cm from the contracted value of 135 cm in  
 1130 fit areas described above.

1131 The blanks were coated by the Thin Film and Glass  
 1132 Service of the Detector Technologies Group at CERN  
 1133 [44]. The reflectivity was also measured at CERN and  
 1134 found to be excellent well into the UV (Fig. 31).

1135 The four mirrors are arranged in a 2 by 2 array with  
 1136 a small overlap in the center, providing full coverage  
 1137 over the active area. In order to accomplish this with-  
 1138 out mechanical interference the mirrors were staggered  
 1139 at slightly different along the tank z-axis. The mirrors  
 1140 were mounted in a monolithic frame installed as single  
 1141 unit (see Figure 32), and are tilted at 15° off the z-axis  
 1142 to place the PMTs to be outside the active area.

1143 The four PMTs are 14 stage 5” quartz window  
 1144 PMTs manufactured by Electron Tubes Enterprises  
 1145 [45], model 9823QKB04. The tubes are surrounded by  
 1146 a mu-metal shield and the HV is distributed to the stages  
 1147 by a positive base. The 9823QKB04 has a quantum effi-  
 1148 ciency above 5% at 150 nm and 30% at 350 nm as seen

1149 in Figure 33.

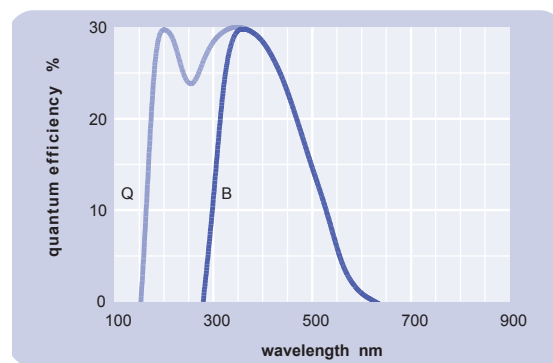


Figure 33: Quantum efficiency of Electron Tubes Enterprises model 9823QKB04 - light blue curve, labeled “Q”.

### 3.7.2. Calibration

As with the HGC (see Sec. 3.6.2), the goal of the NGC calibration procedure is to generate an accurate transformation from raw FADC channels to the number of photoelectrons (NPE) emitted from the cathode surface of the PMT. The NGC calibration method can be broken down into three key steps:

1. Selecting an appropriate data set.
2. Selection cuts to identify a clean electron sample for each PMT.
3. Using the clean electron sample to fit the pulse integral distribution for each PMT. This is used to determine the calibration constants.

*Selecting an appropriate data set.* The NGC calibration requires electron events in the SHMS. Any data set

1165 with the SHMS running with negative polarity can in  
 1166 theory be utilised for calibrations. However, for best re-  
 1167 sults, a data sample with an even distribution of events  
 1168 across all PMTs in the NGC should be utilised. Ad-  
 1169 ditionally, the data set should contain on the order of  
 1170  $\sim 10^6$  events or more.

1171 *Selection Cuts.* To obtain a clean electron sample from  
 1172 the data, several selection cuts are applied to the data.  
 1173 Cuts are applied on:

- 1174 •  $-10 \leq \delta \leq 20$ , a nominal acceptance cut, remov-  
 1175 ing events outside this range.
- 1176 •  $0.7 \leq E_{TotTrackNorm} \leq 2.0$ , a calorimeter based  
 1177 PID cut using the normalized calorimeter energy  
 1178 to remove pion/hadron background events.
- 1179 • NGC multiplicity and position cuts. These are  
 1180 used to select events where the majority of the  
 1181 Cherenkov light was deposited in a single PMT.

1182 After selection cuts, the PMTs can be calibrated.

1183 *Determining Calibration Constants.* After selection  
 1184 cuts, the pulse integral distributions for each of the NGC  
 1185 PMTs are fitted with the function -

$$f(x) = A \frac{\lambda^{\frac{x}{\mu}} e^{-\frac{\lambda}{\mu}}}{\Gamma\left(\frac{x}{\mu} + 1\right)}, \quad (8)$$

1186 where  $A$  is a normalization factor to account for the  
 1187 number of events in the dataset being fit,  $\lambda$  is the mean  
 1188 NPE emitted from the photocathode of the PMT for an  
 1189 event above the Cherenkov threshold, and  $\mu$  is the cali-  
 1190 bration constant that we wish to extract which relates the  
 1191 pulse integral to the corresponding NPE emitted from  
 1192 the photocathode of the PMT. This value is determined  
 1193 for each PMT. An example pulse integral distribution  
 1194 and the associated fit can be seen in Fig. 34.

1195 The NGC PMTs were also gain matched in a similar  
 1196 manner to the HGC. Refer to Sec. 3.6.3 for details on  
 1197 this procedure.

### 1198 3.8. Aerogel Cherenkov Counter

#### 1199 3.8.1. General Design Overview

1200 The detector design is summarized in Fig. 35 which  
 1201 shows a photograph of the aerogel counter installed  
 1202 downstream of the cylindrical HGC in the SHMS de-  
 1203 tector stack. The detector consists of two main com-  
 1204 ponents: a tray which holds the aerogel material, and a  
 1205 light diffusion box with photomultiplier tubes (PMTs)

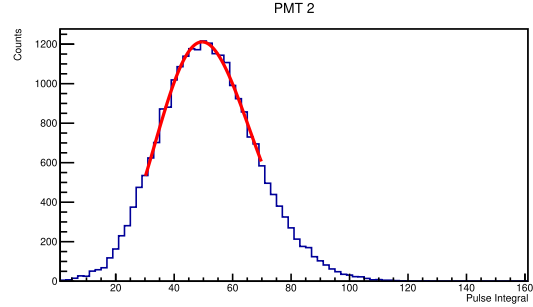


Figure 34: A sample pulse integral distribution fitted with the function described by Eqn. 8 shown in red.

1206 for light readout. Four identical trays for aerogel of  
 1207 nominal refractive indices of 1.030, 1.020, 1.015 and  
 1208 1.011 were constructed. The design allows for easy de-  
 1209 tector assembly and replacement of the aerogel trays.  
 1210 Using up to 9 cm aerogel thickness in the trays, the total  
 1211 depth of the detector is 24.5 cm along the optical axis of  
 1212 the SHMS. A detailed discussion of the detector, char-  
 1213 acterization of its components, and performance tests  
 1214 can be found in Refs. [46, 47].

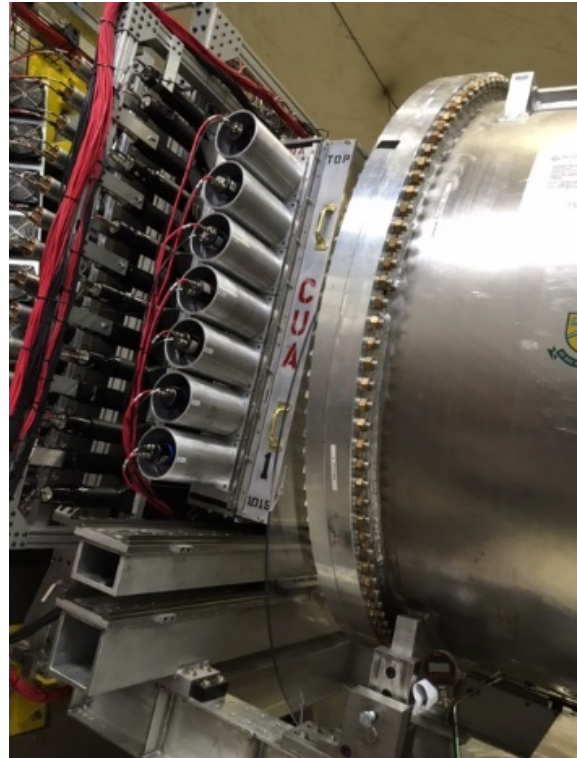


Figure 35: Photograph of the aerogel Cherenkov detector (“CUA” printed on the side of the radiator tray) installed in the SHMS detector stack. To its right is the Heavy Gas Cherenkov. On the left can be seen the edge of the s2x and s2y hodoscope arrays.

Table 4: Threshold momenta  $P_{Th}$  in GeV/c for Cherenkov radiation for charged muons, pions, kaons, and protons in aerogel of four refractive indices ranging from  $n=1.011$  to  $1.030$ .

Particle	$P_{Th}$ $n=1.030$	$P_{Th}$ $n=1.020$	$P_{Th}$ $n=1.015$	$P_{Th}$ $n=1.011$
$\mu$	0.428	0.526	0.608	0.711
$\pi$	0.565	0.692	0.803	0.935
$K$	2.000	2.453	2.840	3.315
$p$	3.802	4.667	5.379	6.307

The diffusion box is made of the aluminum alloy 6061-T6. The side panels are constructed of  $\sim 2.5$  cm (1-inch) plates. The back cover is  $\sim 1$  mm ( $1/16''$ ) thick. The inner dimensions of the box are  $\sim 103 \times 113 \times 17.3$  cm<sup>3</sup> ( $40.5'' \times 44.5'' \times 6.82''$ ). To optimize light collection the inner surface of the diffusion box is lined with either 3 mm (covering  $\sim 60\%$  of the surface) or 1 mm (remaining  $\sim 40\%$  of the surface) thick GORE reflector material [48]. This material has a reflectivity of about 99% over the entire spectrum.

The light collection is handled by 5'' diameter photomultiplier tubes (XP4500). The 5.56'' (14.1 cm) diameter cylindrical housings holding the PMTs are mounted upon 14 waterjet cut circular openings on the left and right (long) sides of the diffusion box, with minimum spacing of 14.92 cm (5.875'') between the centers. The PMTs are sealed into their housing using a light-tight synthetic rubber material (Momentive RTV103 Black Silicone Sealant) and the whole assembly is sealed light-tight. The mechanical design includes six openings on the top of the diffusion box, presently covered with blanks, that can be used to increase the signal output from the detector by about 30%, if needed.

The magnetic shielding for the PMTs consists of 13.5 cm (5.316'') diameter  $\mu$ -metal cylinders, which were constructed to end abreast with the PMT window. The construction also features bucking coils that can be installed on the PMTs, if excessive residual magnetic fields appear to be present in the SHMS hut.

The aerogel trays are of the same transverse size as the diffusion box but 11.3 cm (4.45'') deep. The front cover of the trays is made of a 5 mm thick honeycomb panel with an effective Aluminum thickness of  $\sim 1.3$  mm (0.050''). The inner surface of the SP-30 and SP-20 aerogel trays is covered with 0.45  $\mu$ m thick Millipore paper Membrane GSWP-0010 (Millipore) of reflectivity of about 96% [49]. Though Millipore is difficult to handle, its chemical inertness makes it superior to reflective paints. For the two lower refractive index trays (SP-15 and SP-11), in order to optimize light collection, we used 1 mm thick GORE diffusive reflector material

(DRP-1.0-12x30-PSA) with reflectivity of about 99%.

For the Cherenkov radiator high transparency aerogels were used. The higher two of the refractive indices (SP-30 and SP-20) were originally manufactured by Matsushita Electric Works, Ltd. The lower two indices (SP-15 and SP-11) were manufactured by the Japanese Fine Ceramics Center. These tiles have dimensions of approximately 11 cm by 11 cm by 1 cm. They feature a waterproof coating that make them hydrophobic [50, 51]. This removes the need for baking (which in fact would destroy the coating). Detailed studies of the aerogel characteristics are presented in Ref. [46].

The trays were filled with aerogel tiles layer by layer. In each layer the tiles were laid down flat and arranged in a brick pattern to minimize holes in the radiator. To fill gaps of less than the size of a full tile at the edges of the tray the aerogel material was cut using a diamond coated saw or razor depending on the refractive index of the material. The aerogel radiator is on average  $\sim 9$  cm thick (8 layers). The SP-30, SP-20 and SP-15 aerogel trays were filled over their entire 110 cm x 100 cm area. The SP-11 aerogel tray radiator covers only the active area of 90 cm x 60 cm required by the experiments [52, 19, 17, 53, 13]. An inner frame has been designed to arrange the aerogel tiles inside the active area of this tray. The sides of this inner frame are made of carbon fiber square tubes. This assembly allows future X-Y repositioning of the inner frame inside the tray.

To protect the aerogel radiator from severe damage in case of accidental flipping over of a tray during installation, a net of thin stainless steel wires is installed in close proximity to the aerogel surface. This is a technique previously tested in aerogel detectors at JLab [54]. The wires form an interweaving grid by running between stainless steel screws on the sides of the box. Small springs attached to the ends of wires provide necessary tension.

An aerogel tray attaches to the diffusion box by means of bolting through flanges surrounding both boxes. A round O-ring running in a shallow groove along the diffusion box sides ensures a light tight connection. The entire detector is designed so that it can be removed from the sliding detector stand that positions the detector into the SHMS detector stack.

### 3.8.2. Performance aspects

The light collection performance of the detector was tested with cosmic rays and electron beam. The detector signal shows good uniformity along the vertical (Y) coordinate of the detector surface, but has a significant dependence in the horizontal (X) direction. Possible optimization of this include a variable threshold and an op-



1307 timized selection of the PMTs installed on the right and 1356  
1308 left side of the detector. The response of the detector to 1357  
1309 particles is shown in Fig. 36. 1358

1310 The mean number of photo-electrons in saturation 1359  
1311 for the tray filled with  $n=1.030$  ( $n=1.020$ ) refractive index 1360  
1312 aerogel is  $\sim 10$  ( $\sim 8$ ) which is close to expectation 1361  
1313 from Monte Carlo simulation. For the trays filled with 1362  
1314  $n=1.015$  and  $n=1.011$  refractive index aerogel, high 1363  
1315 numbers of photoelectrons were obtained with the use 1364  
1316 of higher reflectivity GORE material to cover the tray, 1365  
1317  $\sim 10$  and  $\sim 5.5$  respectively. This result could be fully re- 1366  
1318 produced by our Monte Carlo simulation by also assum- 1367  
1319 ing the aerogel absorption length on the order of 220 cm. 1368

### 1320 3.8.3. Results from tests with beam 1370

1321 The performance of the detector was tested with 1371  
1322 beam in Hall C. The detector signal showed good uni- 1372  
1323 formity along the vertical direction, but significant de- 1373  
1324 pendence in the horizontal direction. Possible optimiza- 1374  
1325 tions to address this are discussed below. The mean 1375  
1326 number of photoelectrons in saturation for a tray filled 1376  
1327 with  $n=1.030$  refractive index aerogel is 12 photoelec- 1377  
1328 trons and 10 for the tray filled with  $n=1.015$  refractive 1378  
1329 index aerogel (see Fig. 36). 1379

### 1330 3.8.4. Optimizations 1379

1331 Possible optimizations include a variable threshold 1380  
1332 and optimized selection of PMTs. Lower refractive in- 1381  
1333 dex and highly transparent aerogel like that currently 1382  
1334 under investigation by Aspen Aerogel, Inc. may pro- 1383  
1335 vide kaon proton distinction at even higher particle mo-  
1336 menta. 1383

## 1337 3.9. Preshower and Shower Counters 1384

### 1338 3.9.1. Preface 1385

1339 The approved experiments demand a suppression 1386  
1340 of pion background for electron/hadron separation 1387  
1341 of 1,000:1, with suppression in the electromagnetic 1388  
1342 calorimeter alone on the level of 100:1. An experi- 1389  
1343 ment to measure the pion form factor at the highest ac- 1390  
1344 cessible  $Q^2$  at JLab with an 11 GeV beam requires a 1391  
1345 strong suppression of electrons against negative pions 1392  
1346 of a few 1,000:1, with a requirement on the electromag- 1393  
1347 netic calorimeter of a 200:1 suppression. 1393

1348 Particle detection using electromagnetic calorimeters 1394  
1349 is based on the production of electromagnetic showers 1395  
1350 in a material. The total amount of the light radiated in 1396  
1351 this case is proportional to the energy deposited by the 1397  
1352 primary particle in the medium. Electrons (as well as 1398  
1353 positrons and photons), will deposit their entire energy 1399  
1354 in the calorimeter giving the ratio of of energy detected 1400  
1355 in the calorimeter to particle energy of one. 1401

Charged hadrons entering a calorimeter have a low probability to interact and produce a shower, and may pass through without interaction. In this case they will deposit a constant amount of energy in the calorimeter. However, they may undergo nuclear interactions in the radiator (in our case lead-glass) and produce particle showers similar to the electron and positron induced particle showers. Hadrons that interact inelastically near the front surface of the calorimeter and transfer a sufficiently large fraction of their energy to neutral pions will mimic electrons. The maximum attainable electron/hadron rejection factor is limited mainly by the cross section of such interactions.

In this section we describe details of construction of the SHMS calorimeter. We present results of pre-assembly component checkout, and performance from experimental studies.

### 1392 3.9.2. Construction 1373

As a full absorption detector, the SHMS calorimeter is situated at the very end of detector stack of the spectrometer [55]. The relatively large beam envelope of the SHMS dictated a design of a wide acceptance coverage. The general requirements for the SHMS calorimeter were:

- Effective area:  $\sim 120 \times 140 \text{ cm}^2$ .
- Total thickness:  $\sim 20$  rad. length.
- Dynamic range: 1.0 - 11.0 GeV/c.
- Energy resolution:  $\sim 6\% / \sqrt{E}$ ,  $E$  in GeV.
- Pion rejection:  $\sim 100:1$  at  $P \gtrsim 1.5\text{-}2.0 \text{ GeV}/c$ .
- Electron detection efficiency:  $> 98\%$ .

The SHMS calorimeter consists of two parts (see Fig. 37): a Preshower at the front of the calorimeter, for additional PID, and the main part, the Shower, at the rear for full calorimetry.

An optimal and cost-effective choice was found by using available modules from the HERMES calorimeter for the Shower part, and modules from the Hall C decommissioned SOS calorimeter for the Preshower. With this choice the Shower is 18.2 radiation lengths deep and almost entirely absorbs showers from  $\sim 10$  GeV electromagnetic projectiles, and the Preshower is 3.6 radiation lengths thick.

The SHMS Preshower radiator consists of a layer of 28 TF-1 type lead glass blocks stacked in two columns in an aluminum enclosure (not shown in Fig. 37). 28 PMT assemblies, one per block, are attached to the left

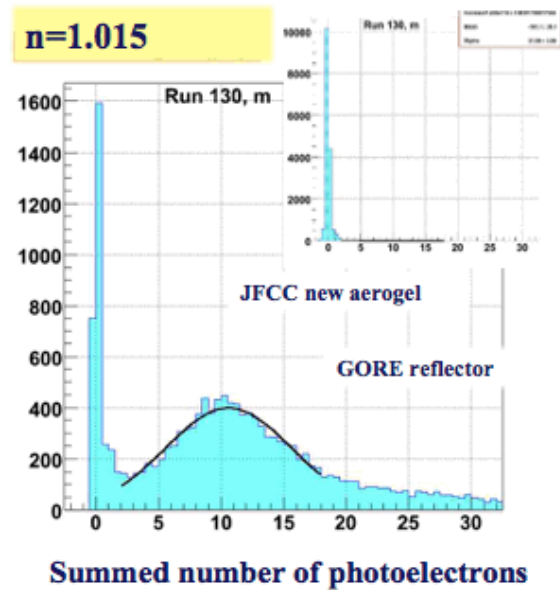
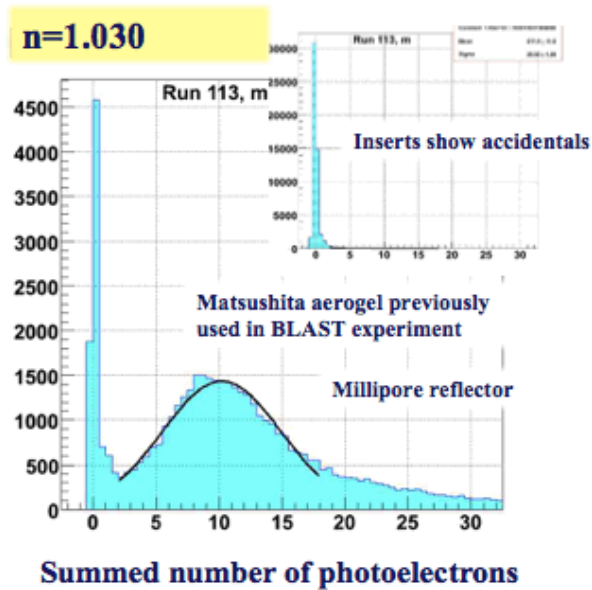


Figure 36: Numbers of photoelectrons observed in the Aerogel Cherenkov.

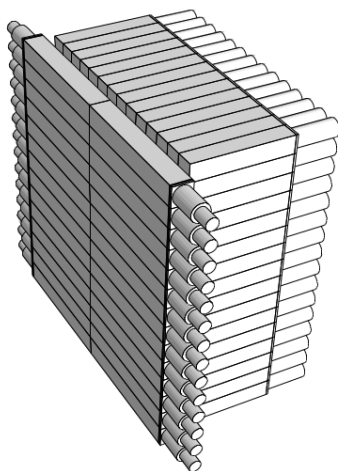


Figure 37: A sketch of SHMS calorimeter. Shown are Preshower (on the left) and Shower parts. Support structures are omitted.

1402 and right sides of the enclosure. The Shower part consists of 224 F-101 type lead glass modules stacked in a “fly’s eye” configuration of 14 columns and 16 rows. All blocks of the Preshower were produced between 1985-1990 by a Russian factory in Lytkarino [56], whose products were well known for their good optical quality.  $\sim 120 \times 130 \text{ cm}^2$  of effective area of detector covers the beam envelope at the calorimeter.

1407 The Preshower enclosure adds little to the material in the path of particles. On the front and back are a 2” Honeycomb plate and a 1 mm sheet of aluminum respec-

1413 tively, which add up to only 1.7% of a radiation length. The optical insulation of the  $10 \text{ cm} \times 10 \text{ cm} \times 70 \text{ cm}$  TF-1 blocks in the Preshower is optimized to minimize the dead material between them, without compromising the light tightness. First, the blocks are loosely wrapped in a single layer of  $50 \mu\text{m}$  thick reflective aluminized Mylar film, with the Mylar layer facing the block surface. Then, every other block is wrapped with a 10 cm wide strip of  $50 \mu\text{m}$  thick black Tedlar film, to cover its top, bottom, left and right sides except for the circular openings for the PMT attachments. Looking at the face of the detector, the wrapped and unwrapped blocks are arranged in a checkerboard pattern. Insulation of the remaining front and back sides of the blocks are provided by facing inner surfaces of the front and rear plates of the enclosure, also covered with Tedlar. In addition, a layer of Tedlar separates the left and the right columns.

1430 The PMT assembly tubes are screwed into 90 mm diameter circular openings on both sides of the enclosure. The spacing of the openings matches the height of the blocks, so that a PMT faces to each of the blocks. The 3” XP3462B PMTs are optically coupled to the blocks using ND-703 type Bicorn grease of refractive index 1.46.

1437 The HERMES modules used in the Shower part are similar in construction to the HMS but differ in details. The radiator is an optically isolated  $8.9 \times 8.9 \times 50 \text{ cm}^3$  block of F-101 lead-glass, which is similar to TF-1 in physical parameters. The typical density of F-101 type lead-glass is  $3.86 \text{ g/cm}^3$ , radiation length 2.78 cm, and

1443 a refractive index of  $\sim 1.65$ . Results of TF-1 and F-101 1494  
1444 type lead-glass blocks transmittance measurements are 1495  
1445 presented in [55]. 1496

1446 Each F-101 block is coupled to a 3" XP3461 PMT 1497  
1447 from Photonis, with green extended bi-alkali photocathode, 1498  
1448 of the same sizes and internal structure as the 1499  
1449 XP3462B in the Preshower. Typical quantum efficiency 1500  
1450 of the photocathode is  $\sim 30\%$  for  $\lambda \sim 400\text{ nm}$  light, and 1501  
1451 the gain is  $\sim 10^6$  at  $\sim 1500\text{ V}$ . Silgard-184 silicone glue  
1452 of refractive index 1.41 is used for optical coupling of 1502  
1453 the PMTs to the lead-glass blocks. 1503

1454 A 1.5 mm thick  $\mu$ -metal sheet and two layers of 1504  
1455 Teflon foil are used for magnetic shielding and electrical 1505  
1456 insulation of the PMTs. The blocks are wrapped with 1506  
1457  $50\text{ }\mu\text{m}$  aluminized Mylar and  $125\text{ }\mu\text{m}$  black Tedlar paper 1507  
1458 for optical insulation. A surrounding aluminum tube 1508  
1459 which houses the  $\mu$ -metal, is fixed to a flange, which 1509  
1460 is glued to the surface of the lead-glass. The flange is 1510  
1461 made of titanium, which matches the thermal expansion 1511  
1462 coefficient of F-101 lead-glass [57]. 1512

1463 Beyond simple repairs, no adjustments have been 1513  
1464 made to the original HERMES construction of the mod- 1514  
1465 ules for re-use in the SHMS calorimeter. As both the 1515  
1466 TF-1 and F-101 lead-glass blocks have been in use for 1516  
1467 more than 14 years under conditions of high luminosity, 1517  
1468 there was concern about possible radiation degradation 1518  
1469 of the blocks and the PMTs. The changes in 1519  
1470 transparency of TF-1 and F-101 type lead-glass radiators 1520  
1471 have been studied. The estimated radiation dose for 1521  
1472 the used blocks was about 2 krad. For several samples of 1522  
1473 F-101 and TF-1 type blocks the light transmittance has 1523  
1474 been measured before and after 5 days of curing with 1524  
1475 UV light (of wavelength  $\lambda=200\text{--}400\text{ nm}$ ). We did not 1525  
1476 find notable degradation in transmittance for the TF-1 1526  
1477 type blocks taken from the SOS calorimeter and F-101 1527  
1478 blocks taken from the HERMES detector. 1527

1479 The gain and relative quantum efficiencies for 1528  
1480 randomly selected PMTs from the SOS calorimeter 1529  
1481 (XP3462B) and from the HERMES detector (XP3461) 1530  
1482 have been measured to check possible degradation effects 1531  
1483 in the PMTs. A  $\sim 10\text{--}15\%$  systematic decrease in 1532  
1484 quantum efficiency was noticed. 1533

### 1485 3.9.3. Photomultiplier tube selection and studies 1535

1486 The SHMS Preshower inherited PMTs from the 1536  
1487 retired SOS calorimeter. The choice of XP3462B PMT 1537  
1488 for Hall C calorimeters was made in 1994 after studies 1538  
1489 of several other 3" and 3.5" photomultiplier tubes 1539  
1490 on the matter of having good linearity, photocathode 1540  
1491 uniformity, high quantum efficiency, and good timing 1541  
1492 properties. Gain variations with HV and dark currents 1542  
1493 were also measured [58]. For samples of PMTs, the 1542

photocathode uniformity and effective diameter have  
been studied with a laser scanner. Following these  
tests, as a time and cost effective solution, a 3" diame-  
ter ( $\approx 68\text{ mm}$ ) semitransparent bi-alkaline photocathode,  
Photonis XP3462B PMTs were chosen for the equip-  
ment of the JLab Hall C calorimeters. These 8-stage  
PMTs have a linear focused cube dynode structure with  
a peak quantum efficiency of  $\sim 29\%$  at 400 nm.

### 3.9.4. Studies on optical properties of TF-1 type lead glass blocks

With its index of refraction  $\sim 1.65$ , radiation length  
2.74 cm and density of  $3.86\text{ g/cm}^3$  TF-1 type lead glass  
is well suited for serving as Cherenkov radiator in elec-  
tromagnetic calorimeters. The fractional composition  
consists primarily of PbO (51.2%), SiO<sub>2</sub> (41.3%), K<sub>2</sub>O  
(3.5%) and Na<sub>2</sub>O (3.5%).

The light transmittance of TF-1 type lead-glass  
blocks for the SHMS Preshower was checked in 2008  
using a spectrophotometer from the JLab Detector  
Group [59]. The wave-length was scanned from 200 nm  
to 700 nm in steps of 10 nm. The blocks were oriented  
transversely, and the light intensity passing through the  
10 cm thickness was measured. The results were com-  
pared with measurements from 1992, before assembling  
of calorimeters for the Hall C HMS/SOS spectrometers.  
Reliability of the measurements was checked by mea-  
suring spared, unused blocks and comparing again with  
1992 data. From comparison of 1992 and 2008 data,  
signs of marginal degradation has been noticed. [Any-  
thing to quantify this?](#)

### 3.9.5. Choice and studies of PMT bases

The Preshower PMT high voltage base design is opti-  
mized for the requirements of good linearity (better than  
1%), high rate capability and a weak variation of PMT  
gain with anode current [58].

A design, which is a purely resistive, high cur-  
rent (2.3 mA at 1.5 kV), surface mounted divider  
( $\sim 0.640\text{ M}\Omega$ ), operating at negative HV was se-  
lected. The relative fractions of the applied HV  
between the dynodes (from cathode to anode) are:  
3.12/1.50/1.25/1.25/1.50/1.75/2.00/2.75/2.75. The sup-  
ply voltage for a gain of  $10^6$  is approximately 1750 V.

The PMT resistive base assembly is linear to within  
 $\sim 2\%$  up to the peak anode current of  $120\text{ }\mu\text{A}$  ( $\sim 5 \times 10^4$   
pe). The dark current is typically less than 3 nA. The  
base has anode and dynode output signals.

### 3.9.6. Monte Carlo simulations

Prior to construction, the designed calorimeter setup  
was simulated in order to possibly optimize the setup

1543 and get predictions for key characteristics. The simu- 1590  
 1544 lations were based on the GEANT4 package [60], re- 1591  
 1545 lease 9.2. As in the simulations of the HMS calorimeter 1592  
 1546 (see [55]), the QGSP\_BERT physics list was chosen to 1593  
 1547 model hadron interactions [61]. The code closely fol- 1594  
 1548 lowed the parameters of the detector components. Other 1595  
 1549 features are added into the model in order to bring it 1596  
 1550 closer to reality, such as: 1597

- 1551 • Light attenuation length in the lead glasses and its
- 1552 block to block variation according to our measure-
- 1553 ments.
- 1554 • PMT quantum efficiencies from the graphs pro-
- 1555 vided by vendor.
- 1556 • Passive material between the spectrometer focal
- 1557 plane and the calorimeter.
- 1558 • Sampling of incoming particles at the focal plane
- 1559 of the spectrometer.

1560 The Cherenkov light propagation and detection was  
 1561 handled by a custom code, using an approximation of  
 1562 strict rectangular geometry of the lead glass blocks with  
 1563 perfectly polished surfaces. Light reflection and absorp-  
 1564 tion by the Mylar wrapping was modeled via Aluminum  
 1565 complex refractive index, with Mylar support facing the  
 1566 block, and a thin air gap between the wrapping and the  
 1567 block. Both light passage to the PMT photocathode  
 1568 through the optical grease and the PMT window, and  
 1569 reflections from the block sides were modeled using the  
 1570 approximation of thin dielectric layers ([62], p. 360).  
 1571 The electronic effects, such as pedestal widths and chan-  
 1572 nel to channel PMT gain variations were assumed as for  
 1573 the HMS calorimeter before the 12 GeV modifications.  
 1574

1575 The simulations revealed no flaws in the design con-  
 1576 struction of the SHMS calorimeter, and performance  
 1577 similar to other lead glass based calorimeters. The  
 1578 studies indicated gain in pion suppression on the or-  
 1579 der of several times from combining signals from the  
 1580 Preshower with the total energy deposition in the  
 calorimeter.

### 1581 3.9.7. Calorimeter Gain Matching

1582 Gain matching of PMTs is important for uniformity  
 1583 of performance of the calorimeter over the spectrom-  
 1584 eter's acceptance. Minimum ionizing particles (MIP's)  
 1585 were used for this purpose as their signals from the  
 1586 calorimeter are nearly independent of the incident parti-  
 1587 cle's momentum.

1588 MIP pion candidates for the Shower gain match- 1607  
 1589 ing were selected by requesting 4 PMT signals from 1608

the Heavy Gas Cherenkov counter of less than 2 p.e.,  
 and the normalized deposited in the Preshower energies  
 close to the MIP peak value, within a range from 0.02  
 to 0.15. In addition, the MIP dominance in the Shower  
 itself was ensured by selecting single hit events, when  
 only one module was fired. The resultant MIP peaks in  
 the ADC signal distributions were localized by Gaus-  
 sian fits (see Fig. 38).

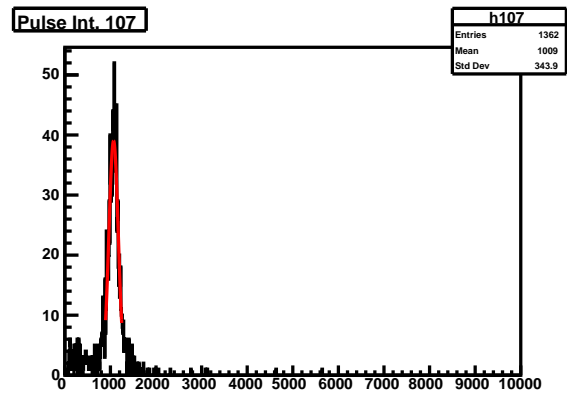


Figure 38: Distribution of ADC signals of a Shower module from minimum ionizing pions. The red line is a Gaussian fit to the MIP peak.

As gain matching had to be achieved by adjustment  
 of high voltages on the PMT bases, knowledge of gain  
 variations versus supplied HV's had been needed. That  
 was obtained by measuring signals from MIP pions at 2  
 constant supply high voltages on all the Shower chan-  
 nels, at 1.4 kV and 1.5 kV (see Fig. 39). By assuming  
 gain dependence on supplied voltage in the form  $\sim V^\alpha$   
 [41], the average exponent  $\alpha$  was found to be  $5.70 \pm$   
 $0.01$  for a set of  $\sim 100$  channels.

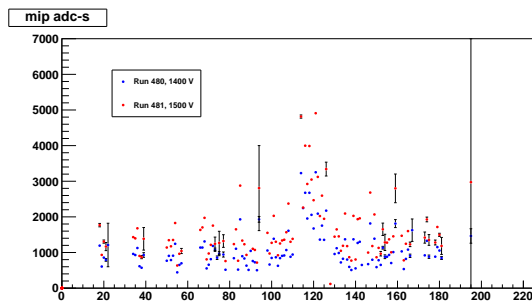


Figure 39: Amplitudes of ADC signals from MIP pions in a set of Shower channels, for supply voltages of 1.4 kV and 1.5 kV.

The gain matching was done in two ways. In the first  
 case, MIP signals from pions were used. From the ref-

1609 erence run with supply voltages  $A_{REF} = 1.4 \text{ kV}$  in all the 1636  
 1610 Shower channels, MIP ADC signal amplitudes  $A_{REF}(i)$  1637  
 1611 were obtained as described above. For a desired con- 1638  
 1612 stant signal amplitude  $A_{SET} = 1000 \text{ ADC channels}$ , the 1639  
 1613 set voltages  $V_{SET}(i)$  were estimated via

$$V_{SET}(i) = V_{REF} \cdot \left( \frac{A_{SET}}{A_{REF}(i)} \right)^{1/\alpha} \quad (9)$$

1614 In the second case, data from a run with negative po-  
 1615 larity (electrons in the SHMS) were used. The SHMS  
 1616 optics was set up at  $3 \text{ GeV}/c$  central momentum, in a  
 1617 defocused mode, which allowed for hitting and calibration  
 1618 with electrons of more than 150 Shower modules.  
 1619 For deposited energy,  $E$ , in a given module with signal  
 1620 amplitude  $A$ , PMT gain  $g$ , calibration constant  $c$  the fol-  
 1621 lowing holds:  $A \sim g \cdot E$ ,  $E = c \cdot A$ . Hence  $g \sim V^\alpha \sim 1/c$ ,  
 1622 and for the chosen calibration constant  $c_{SET}$  one gets

$$V_{SET}(i) = V_{REF} \cdot \left( \frac{c_{SET}^{-1}}{c_{REF}^{-1}(i)} \right)^{1/\alpha} \quad (10)$$

1623 The HV settings from the second method, for  $c_{SET} =$   
 1624  $35 \text{ MeV}/\text{ADC ch}$  are within the range from  $1.2 \text{ kV}$  to 1640  
 1625  $1.6 \text{ kV}$  and are grouped around  $1.4 \text{ kV}$  (Fig. 40). A few 1641  
 1626 settings above the hard limit of  $1.7 \text{ kV}$  were forced to 1642  
 1627 the limit. The HV settings from the two methods are in 1643  
 1628 correlation. 1644

1629 Note that out of acceptance, hence not gain matched, 1645  
 1630 channels were left at nominal  $1.4 \text{ kV}$  high voltages. 1646  
 1631 Note also that the chosen voltages are conservative, less 1647  
 1632 than HV settings at which modules had been operated 1648  
 1633 in the HERMES calorimeter. 1649

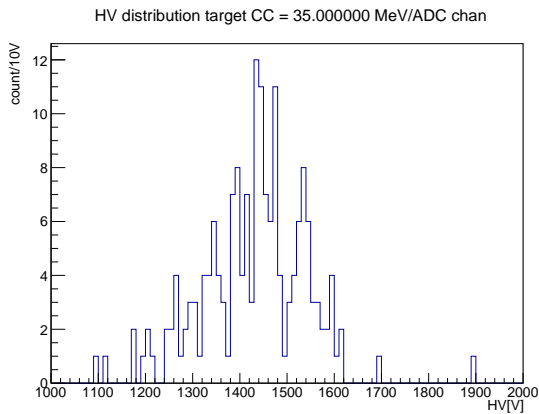


Figure 40: Gain matched high voltage settings for the Shower PMTs (see text for details).

1634 The amplitudes of ADC signals from MIP pions after  
 1635 the gain matching are shown in Fig. 41. The majority of

amplitudes are grouped between 20 and 30 ADC channels. The spread in signals among hit channels is much less than in the case of constant supply voltages (compare with Fig. 39).

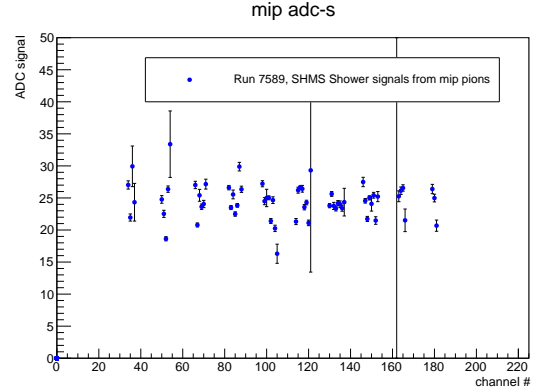


Figure 41: Amplitudes of ADC signals from MIP pions in a set of Shower channels after gain matching.

The Preshower detector was gain matched with cosmic rays, prior to installation in the spectrometer. Coincidence of signals from scintillator counters positioned above and below the detector served as a trigger. The gain matching was adjusted after the installation, again with cosmics but this time passing through the detector stack. Muons were identified as events of single track in the drift chambers and single hit module in the Preshower. New set of voltages were calculated based on MIP peak positions and according to a formula similar to Eqns 9, 10. The voltages span the range from  $1.1 \text{ kV}$  to  $1.7 \text{ kV}$ . The quality of gain matching was insured by taking cosmic data with the new HV settings (Fig. 42).

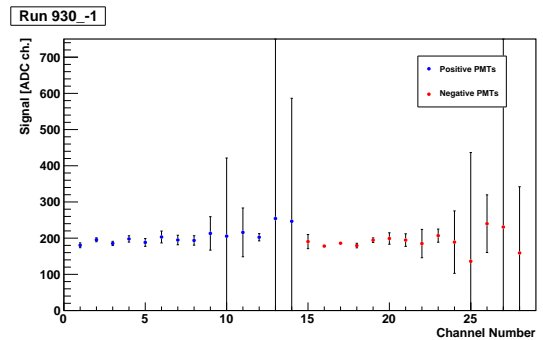


Figure 42: Amplitudes of ADC signals from cosmic muons in the Preshower channels after gain matching.

### 3.9.8. Calorimeter Calibration

The ability of particle identification of a calorimeter is based on differences in the energy deposition from different types of projectiles. The deposited energy is obtained by converting the recorded ADC channel value of each module into an equivalent energy.

The data analysis procedure corrects for the gain differences in the process of calorimeter calibration. Good electron events are selected by utilising the gas Cherenkov detector(s). The standard calibration algorithm [63] is based on minimization of the variance of the estimated energy with respect to the calibration constants, subject to the constraint that the estimate is unbiased (relative to the primary energy). The momentum of the primary electron is obtained from the tracking in the magnetic field of the spectrometer.

The deposited energy per channel is estimated by

$$e_i = c_i \times A_i, \quad (11)$$

where  $i$  is the channel number,  $c_i$  is the calibration constant,  $A_i$  is the FADC pulse integral signal. Note that the Preshower signals are corrected for the light attenuation dependence versus horizontal hit coordinate  $y$ . The calorimeter calibration can be checked by comparing the track momentum to the energy deposition in the calorimeter. The ratio -

$$\frac{P_{Track}}{E_{Dep}}, \quad (12)$$

is referred to as the *normalized energy*,  $E_{Norm}$ . For electrons,  $E_{Norm}$  should be equal to 1 as all energy should be deposited in the calorimeter. An example of the normalized energy distribution for electron tracks can be seen before and after a successful calibration in Figs. 43 and 44.

In the calorimeter analysis code, hits on adjacent blocks in the Preshower and in the Shower are grouped into clusters. For each cluster the deposited energy and center of gravity are calculated. These clusters are matched with tracks from the upstream detectors if the distance from the track to cluster is less than a predefined “slop” parameter (usually 7.5 cm). For the Preshower the distance is calculated in the vertical direction.

## 4. Trigger and Data Acquisition

The Hall C data acquisition (DAQ) system is designed to meet the needs of a high luminosity, dual spectrometer (SHMS + HMS) configuration, with the capability of extracting polarization-dependent absolute

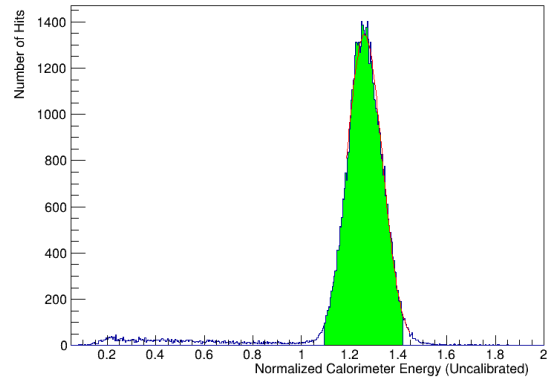


Figure 43: An electron sample (selected through Cherenkov PID) in the calorimeter before calibration. The peak of the  $E_{Norm}$  distribution is clearly greater than 1 and is relatively wide.

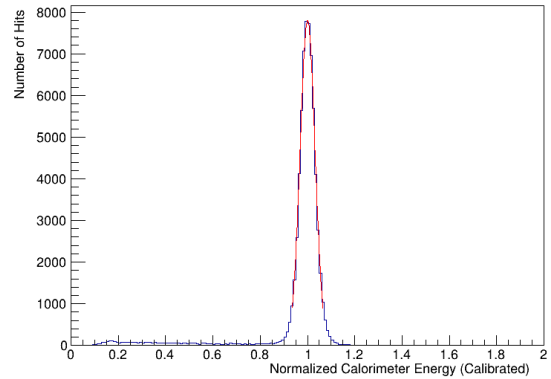


Figure 44: An electron sample (selected through Cherenkov PID) in the calorimeter after calibration. The peak of the  $E_{Norm}$  distribution is now much narrower and centred at 1 as expected for electrons.

cross sections with precision at the 1% level or better. JLab’s CODA data acquisition software [64] provides a framework that ties together a distributed network of read-out controllers (ROCs) controlling multiple crates of digitization hardware, event builders to serialize the data, and event recorder processes to write the data to disk. It also provides a graphical control interface for the users.

The Hall C DAQ system can run in dual-arm trigger mode that requires a coincidence between both spectrometers, or each arm’s DAQ may be run entirely independently of the other. Incorporating additional detector systems into the standard two-arm design is also straight forward. A high-level block diagram of trigger formation and readout for each spectrometer arm (SHMS or HMS) is depicted in Fig. 45.

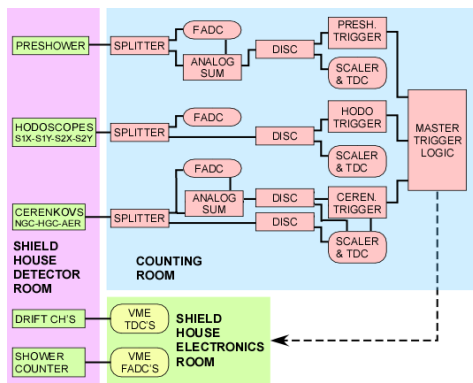


Figure 45: Block diagram of high-level trigger formation for SHMS (and HMS). See Sec. 4.1 for details.

#### 4.1. Standard Triggers

All trigger-related PMT signals from both the SHMS and HMS are routed out of the experimental Hall to a dedicated electronics room on the main level of the Hall C Counting House using low-loss RG-8 air-core signal cables. Those signals are then split with one copy running into a JLab F250 flash analog to digital converter (FADC)[65], and the second copy is processed and discriminated. All discriminated pulses are delivered to scalers for rate information, TDCs for precision timing measurement, and to form pre-triggers as described below. This design allows direct access to all raw signals that may participate in a trigger during beam operations and has proven invaluable during the debugging and commissioning phases of Hall operations.

Non-trigger related signals include wire-chamber readouts and the Shower (but not Preshower) layer of the SHMS calorimeter. The readout electronics for those sub-detectors remain inside their respective detector huts within the experimental Hall. All SHMS calorimeter PMT signals are fed into F250 FADCs configured to provide timing, integrated energy, pulse amplitude, and (optionally) pulse profile data as desired. The wire-chamber timing signals are digitized using multi-hit CAEN v1190 modules [66].

The CAEN v1190 payload module provide 128 independent multi-hit/multi-event TDC channels with a user configurable resolution ranging from  $52\ \mu\text{s}$ — $100\ \text{ps}$  per bin. They provide a 32 kilo-word deep output buffer and can be readout asynchronously with respect to the event triggers. Typical Hall C operation has all units configured for  $100\ \text{ps}/\text{bin}$ .

##### 4.1.1. JLab F250 Flash ADCs

The JLab F250 flash ADC modules are an FPGA-based design developed by the Jefferson Lab Fast Electronics group [65] and are used Lab wide. Each F250 module provides 16 independent  $50\ \Omega$  input channels. The voltage at each input channel is continuously digitized into an  $8\ \mu\text{s}$  ring buffer at  $250\ \text{MHz}$ , with a resolution of 12 bits, and a hardware adjustable full-scale range. When a module receives a readout trigger, digitized sample data stored in the ring buffer is processed in a parallel process that does not incur front-end deadtime. In typical operation each ‘hit’ over a pre-programmed threshold is assigned an interpolated leading-edge threshold time ( $<1\ \text{ns}$  resolution), integrated energy (analogous to a charge-integrating ADC value), a peak-amplitude, and a measurement of any DC offset (pedestal) present on the channel prior to the detected pulse. Full pulse-profile data for each hit may

The hardware DAQ and trigger designs were strongly influenced by the preceding 6 GeV HMS and SOS configurations. This choice was made to provide a careful and systematic migration from the very well understood systematics of the 6 GeV system while incorporating and characterizing a new generation of FPGA-based logic and readout electronics. To this end, the present system relies on a combination of legacy NIM and CAMAC discriminators and logic modules to form readout triggers, but utilizes a full set of modern high speed payload and front-end modules to allow a transition to a firmware based trigger and fully pipelined readout in the future.

In the present configuration, the DAQ has a nominal maximum trigger accept rate of  $4\ \text{kHz}$  with a deadtime of  $\approx 20\%$ . Dead times are measured using the Electronic Dead Time Measurement system outlined in Sec. 4.2. The underlying hardware supports running in a fully pipelined mode, and should be capable of running at trigger rates exceeding  $20\ \text{kHz}$  with minimal deadtime using firmware based triggers similar to those employed in Halls B and D. This capability was not part of the initial 12 GeV upgrade plan for Hall C, but may be pursued in the future (see Sec. 4.5).

Signals from the scintillator planes, Cherenkov detectors, and calorimeter detectors in the SHMS and HMS detector stacks are processed to form *pre-triggers*. Those pre-triggers can serve as *event triggers* themselves (that initiate a recorded event), or be combined to bias data collection towards particular particle types (*i.e.* electrons *vs.* pion) and suppress backgrounds. Each running DAQ can be fed up to six independent triggers simultaneously and the Experimenter can control what fraction of each is recorded to disk run-by-run through an integrated pre-scale feature.

1798 also be stored if desired. However, that mode increases  
 1799 the data rate by several orders of magnitude, and is generally  
 1800 used only for debugging or limited duration pulse  
 1801 characterization runs.

#### 1802 4.1.2. SHMS Triggers

1803 The SHMS detector stack layout is described in  
 1804 Sec. 3.2. A representative detector layout is presented  
 in Fig. 46.

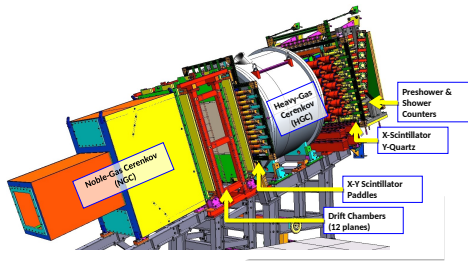


Figure 46: Typical detector layout for the SHMS.

1805 Each hodoscope plane described in Sec. 3.3 and  
 1806 Sec. 3.4 is constructed from an array of horizontal (or  
 1807 vertical) bars with a PMT on each end. Signals from  
 1808 those PMTs are split and one analog copy is delivered  
 1809 to F250 FADCs. The second analog copy is discriminated  
 1810 and sent to CAEN 1190 TDCs for precision timing  
 1811 information, to scalars for raw rate information, and  
 1812 to logic modules to provide the hodoscope pre-triggers  
 1813 plane by plane. A pre-trigger for each plane generated  
 1814 by OR'ing the discriminated signals from each side of  
 1815 a hodoscope plane together, then AND'ing the result-  
 1816 ing two signals together. The pre-triggers are designat-  
 1817 ed S1X, S1Y and S2X, S2Y; where 1(2) denote the  
 1818 up(down)stream plane, and X(Y) denote the horizon-  
 1819 tal(vertical) scintillator bar orientation (see Fig. 47).  
 1820

1821 It should be noted an optimal design would generate  
 1822 an AND between the PMTs on each side of every bar  
 1823 first, and OR the resulting per-bar coincidences to form  
 1824 a pre-trigger for the plane. The compromise above was  
 1825 driven by constraints of the legacy LeCroy 4564 CA-  
 1826 MAC logic units held over from the 6 GeV era.  
 1827

1828 The SHMS detector stack includes a permanent  
 1829 Heavy Gas Cherenkov (HGC) (see Sec. 3.6), but also in-  
 1830 cludes space for a second Noble Gas Cherenkov (NGC)  
 1831 (see Sec. 3.7). Each SHMS gas Cherenkov detector in-  
 1832 corporates four PMTs, each detecting light from one of  
 1833 four mirrors inside their respective gas volumes. Analog  
 signals from the PMTs are split (50:50) with one

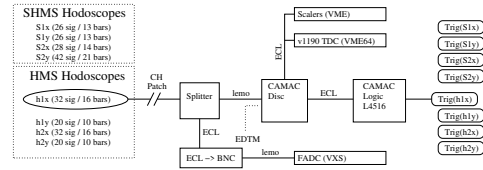


Figure 47: Block diagram for SHMS and HMS hodoscope pre-trigger formation.

1834 path plugged into an FADC. The second copies from  
 1835 each PMT are summed, and the summed output is dis-  
 1836 criminated to form a Cherenkov pre-trigger for that  
 1837 Cherenkov detector (HGC and NGC). The pre-triggers  
 1838 are also routed to scaler channels and a v1190 TDC.

1839 An optional SHMS Aerogel as detailed in Sec. 3.8  
 1840 may also be installed. It employs seven PMTs on each  
 1841 side of its diffusion box. The signals from all 14 PMTs  
 1842 are handled analogous to the gas Cherenkov, with each  
 1843 analog signal being split and readout by an individual  
 1844 FADC channel, and second copies being summed and  
 1845 discriminated to form an associated aerogel pre-trigger.  
 1846 The pre-trigger is routed to a scaler and v1190 TDC as  
 1847 well.

1848 A block diagram for the Cherenkov pre-triggers is  
 1849 presented in Fig. 48.

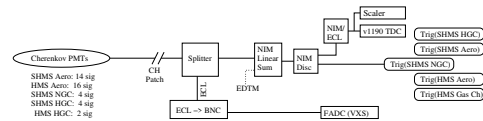


Figure 48: Block diagram for SHMS and HMS Cherenkov pre-trigger formation.

1850 The SHMS Preshower layer described in Sec. 3.9  
 1851 consists of 28 lead-glass blocks arranged 14 rows, with  
 1852 2 blocks to a row. Each block is coupled to a single  
 1853 PMT on the side facing the perimeter of the layer. Analog  
 1854 signals from the 28 PMTs are split and summed in  
 1855 3 groups of 4 rows, and 1 group of 2 rows. Each of the  
 1856 4 group sums is readout by an FADC channel for cross  
 1857 checks. The 4 group sums are summed in turn to provide  
 1858 a total Preshower sum which is then discriminated and  
 1859 provides the SHMS *PSh* pre-trigger. Provision is  
 1860 made to generate independent pre-triggers for both low-  
 1861 and high- energy depositions in the Preshower layer  
 1862 (*PSh<sub>Lo</sub>* and *PSh<sub>Hi</sub>*, respectively) as seen in Fig. 49.

1863 The aforementioned pre-triggers are then combined  
 1864 to form a set of triggers capable of initiating a DAQ  
 1865 event. These combination are often adjusted or opti-  
 1866 mized to serve the needs of particular experiments but a  
 1867 set of commonly available event triggers is outlined in  
 1868 Sec. 4.1.4.



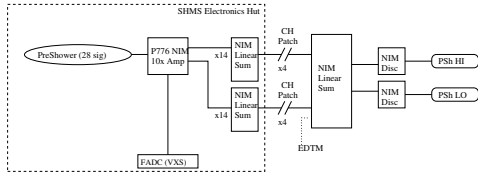


Figure 49: Block diagram for SHMS Preshower summing trigger.

#### 4.1.3. HMS Triggers

The standard HMS detector stack is the predecessor of the SHMS system and shares a nearly identical design as seen in Fig. 50. It consists of a pair of scintillator-based hodoscope planes in an X+Y configuration, a gas Cherenkov detector, a second pair of X+Y hodoscopes, and a Preshower + Shower Calorimeter. Provision is also made for an optional Aerogel Cherenkov to be inserted into the detector stack just downstream of the drift chambers for supplemental particle identification (PID).

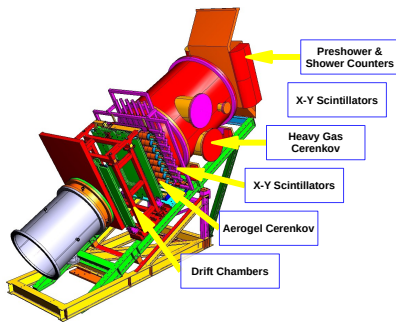


Figure 50: Typical detector layout for the HMS.

The trigger and readouts designs follow the patterns described in Sec. 4.1.2, with a modest difference associated with the HMS Calorimeter.

Signals from the four HMS hodoscope planes, denoted  $h1x$ ,  $h1y$ ,  $h2x$ ,  $h2y$ , are split, discriminated, and recombined to form a *Scin* trigger following the same logic as the SHMS hodoscopes described previously.

The HMS gas Cherenkov detector incorporates two PMTs detecting light from two mirrors inside the HMS Cherenkov tank. Analog signals from the PMTs are split (50:50) with one path plugged into an FADC. The second copies from each PMT are summed, and the summed output is discriminated to form the Cherenkov pre-trigger. That pre-trigger is also routed to a scaler and v1190 TDC.

The HMS Aerogel employs eight PMTs on each side of its diffusion box. The signals from all 16 PMTs are

split and readout by an individual FADC channel, with the second copies being summed and discriminated to form the associated aerogel pre-trigger. The pre-trigger is routed to a scaler and v1190 TDC as well.

The HMS calorimeter is composed of four layers of lead glass blocks. Each layer has 13 lead-glass blocks arranged horizontally, and the layers are denoted A, B, C and D as seen by a particle passing through the detector stack. Layers A and B have PMTs bonded to each end of their blocks, while Layers C and D have a single PMT on one side only. Analog signals from the PMTs are split 50:50 with one copy being delivered to an FADC. The copies are formed into an analog sum for each side of each layer, denoted  $hA+$ ,  $hA-$ ,  $hB+$ ,  $hB-$ ,  $hC$ , and  $hD$ . Layer sums  $hA$  and  $hB$  are formed by summing  $hA+$  and  $hA-$ , and  $hB+$  and  $hB-$ , respectively ( $hC$  and  $hD$  are already layer sums).

One copy of each layer sum is sent to an FADC for monitoring and cross checks. A Preshower pre-trigger is formed by summing and discriminating Layers A + B, and a *Shower Low* pre-trigger is formed by summing and discriminating Layers A+B+C+D. Copies of the Preshower and Shower sums are sent to FADCs and copies of the discriminated pre-trigger signals are sent to scalars and 1190 TDCs.

Fig. 51 depicts a block diagram of the HMS Calorimeter pre-triggers.

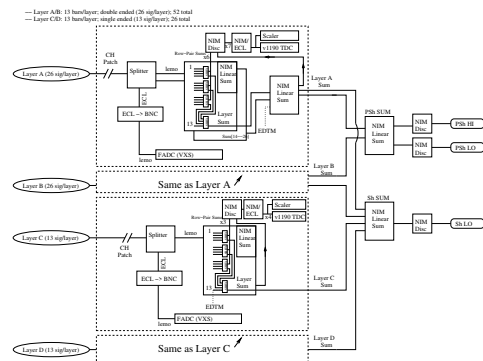


Figure 51: Block diagram for HMS Shower and Preshower summing triggers.

#### 4.1.4. Event Triggers

The aforementioned pre-triggers are then combined to form a set of triggers capable of initiating a DAQ event. The 'default' single-arm trigger is formed by 3 out of 4 hodoscope planes firing in coincidence. Often referred to as the *3 of 4* or *Scin* trigger, it provides a high-efficiency (> 99%) general-purpose charged particle trigger.

1932 A second standard trigger is referred to as *EL\_Clean*. 1981  
1933 It implements particle discrimination at the trigger level 1982  
1934 by forming a coincidence between the *Scin* pre-trigger, 1983  
1935 one (or more) Cherenkov pre-triggers, and (option- 1984  
1936 ally) the pre-shower (*PSh*) and/or calorimeter total-sum 1985  
1937 (*ShTot* pre-triggers). 1986

#### 1938 4.2. Electronic Dead Time Measurement System 1987 1939 (EDTM) 1988

1940 The DAQ and trigger system for each spectrometer 1989  
1941 also includes an Electronic Dead Time Measurement 1990  
1942 (EDTM) system. This is implemented by replicating 1991  
1943 a pulse from a pulse-generator circuit and feeding into 1992  
1944 every pre-trigger leg as close to the analog signals as 1993  
1945 possible. The timing of those duplicated pulses is ad- 1994  
1946 justed to match those generated by a real particle pass- 1995  
1947 ing through the detector stack. A copy of each synthetic 1996  
1948 EDTM trigger is counted in a deadtime free scaler and 1997  
1949 sent to a dedicated TDC channel in each arm. The pres- 1998  
1950 ence of an appropriately timed hit in that TDC channel 1999  
1951 tags an event as having been generated by an EDTM 2000  
1952 trigger. 2001

1953 During beam operations, this allows a direct measure- 2002  
1954 ment of the fraction of triggers that are lost due to some 2003  
1955 component of the DAQ being busy. This is known as 2004  
1956 the system *deadtime*. By inducing synthetic signals as 2005  
1957 early in the trigger electronics as possible, this system 2006  
1958 is sensitive to high-rate signal pile-up in the full front- 2007  
1959 end trigger logic chain, as well as digitization and read 2008  
1960 out related deadtimes implicit in the non-pipelined DAQ 2009  
1961 operation presently in use in Hall C. 2010

1962 In addition to the above function, the system has 2011  
1963 proved useful for pre-beam trigger verification and end 2012  
1964 to end checkout of the DAQ system. 2013

- 1965 • It allows rough timing on all trigger legs to be ver- 2014  
1966 ified without beam. 2015
- 1967 • It allows coincidence timing between the SHMS 2016  
1968 and HMS arms to be roughed in and tested without 2017  
1969 beam. 2018
- 1970 • It allows the entire DAQ system to be stress tested 2019  
1971 under controlled conditions without beam. 2020

#### 1972 4.3. Auxiliary Data Collection 2021

1973 The standard method for slow controls data logging is 2022  
1974 through the Experimental Physics and Industrial Con- 2023  
1975 trol System (EPICS) [67]. EPICS is a system of open 2024  
1976 source software tools and applications used to pro- 2025  
1977 vide control user interfaces and data logging for sys- 2026  
1978 tems such as high- and low-voltage detector power sup- 2027  
1979 plies, target systems, spectrometer magnets, vacuum, 2028  
1980 and cryogenic systems, etc. 2029

Long-term, persistent storage of EPICS based slow controls data is provided through an independent archiving system managed by the Accelerator Division's MYA archiving system. An experimentally relevant subset of EPICS data (beam and target characteristics; magnet, spectrometer and detector settings, etc.) are also stored in the experimental data files at regular intervals whenever the DAQ is running.

#### 4.4. Online Hall C Computing Environment

Hall C employs a dedicated stand-alone computing cluster with redundant multi-core servers focused on prompt online analysis, high volume local data storage, and 1–10 Gb ethernet interconnects. There are dedicated hosts for each independent DAQ system (*ex. SHMS and HMS*), and auxiliary machines for polarimetry, target controls, spectrometer slow controls, etc.

Experimental control and operational feedback is provided to users in the Hall C Counting house through a collection of multi-screen computer workstations and a set of large wall-mounted displays for critical data.

All systems have direct access to the JLab centrally managed Scientific Computing resources. This includes multi-petabyte tape storage and online disk facilities, as well as a several thousand core compute farm for simulation and offline data analysis [68].

#### 4.5. Future Plans / Pipeline trigger

During the early stages of the 12 GeV Hall C upgrade plan it was concluded that the risks of moving to a fully pipelined DAQ system with a firmware driven trigger were not justified by the needs of the initial experimental program. In general, those experiments did not impose a too heavy burden on the DAQ, and the more conventional trigger design with its well understood characteristics was preferred.

However, provision was made to design and build the low-level DAQ system with an upgrade path in mind. To that end, a full compliment of trigger and payload modules compatible with the pipelined systems being implemented for Halls B and D was selected.

A phased transition from the NIM/CAMAC trigger system to a fully pipelined approach would involve implementing the present trigger logic within the existing JLab FADC and VXS Trigger Processor (VTP) boards, and a thorough validation of the firmware based trigger decisions against the well understood conventional trigger. Once the firmware is fully debugged/characterized, the DAQ could transition to pipelined mode and take advantage of significant boost in trigger accept rates into the 10's of kHz range with minimal deadtime. At that

point the next DAQ bottleneck would likely be rate limitations in the detector systems themselves (signal pile-up in the front-end, track reconstruction limitations, etc.)

## 5. Software

Hall C Data is analyzed by the Hall C analysis package *hcana*. This package does full event reconstruction for the SHMS used alone or in coincidence with other detectors. *hcana* is based on the modular Hall A analyzer [69] ROOT [70] based C++ analysis framework. This framework provides for run time user configuration of histograms, ROOT tree contents, cuts, parameters and detector layout.

*hcana* includes C++ classes for detectors, spectrometers, and physics analyses. Instantiation of these classes as objects is configured at run-time through a ROOT script which also sets up the configuration of analysis replay. Due to the similarity of the SHMS and HMS spectrometers and their detector packages, the same spectrometer and detector classes are used for both spectrometers. For example, the drift chamber package class is instantiated for both spectrometers with each object configured by its specific parameters and geometry. Additional modules such as new front end decoders, detectors, or physics analysis modules can easily be added to *hcana*. These modules can either be compiled into the analyzer or be compiled separately and dynamically loaded at run time.

Event analysis is segmented into 3 steps of spectrometer and detector specific analysis.

1. Decoding: Detector requests from the low level decoder a list of hits sorted detector by plane and counter number. A minimal amount of processing is done to make data available for low level histograms.
2. Coarse Processing: Tracks are found in the drift chambers. Hits and clusters in the hodoscope, shower counter and other detectors are matched to the tracks to determine time-of flight. The various detectors provide information for particle identification.
3. Fine processing: Particle identification information is refined, tracks in the focal plane are traced back to the target coordinate system and particle momentum is determined.

Each step of these steps is completed for all detectors before proceeding to the next step. Some limited information is passed between detectors at each step. For example, timing information from the hodoscopes is used

to obtain the start time for the the drift chambers in the decoding step and tracks obtained from the drift chambers are associated with shower counter hit clusters in the fine processing step.

After these steps, single arm and coincidence physics quantities are calculated using various physics analysis classes that are configured at run-time.

### 5.1. Online Monitoring

After each data taking run (typically an hour or less) is started, a subset of the data is analyzed with *hcana*. An easily configurable histogram display GUI is used to view diagnostic histograms and compare them to reference histograms. The EPICS [67] control system alarm handler is used to monitor experiment settings and beam conditions. This includes spectrometer magnet settings, detector high voltages, drift chamber gas, cryogenic systems and spectrometer vacuum.

## 6. SHMS Performance: Operating Experience and Commissioning Results

### 6.1. Acceptance

The acceptance of the SHMS can be determined from simulation and defined as  $A(\delta, \theta) = N_{sus}(\delta, \theta)/N_{gen}(\delta, \theta)$ , where  $N_{gen}$  is the number of events generated into a particular  $\delta, \theta$  bin and  $N_{sus}$  is the number of events that successfully reached the detector stack. Since  $A(\delta, \theta)$  depends on the generation limits of the simulation, a more useful quantity is the effective solid angle,  $\Delta\Omega_{eff} = A(\delta, \theta) * \Delta\Omega_{gen}$ , where  $\Delta\Omega_{gen}$  is the solid angle generated into for each bin. Fig. 52 shows the effective solid angle of the SHMS at a central angle of  $21^\circ$  and central momentum of  $3.3 \text{ GeV}/c$  for a 10 cm liquid hydrogen target.

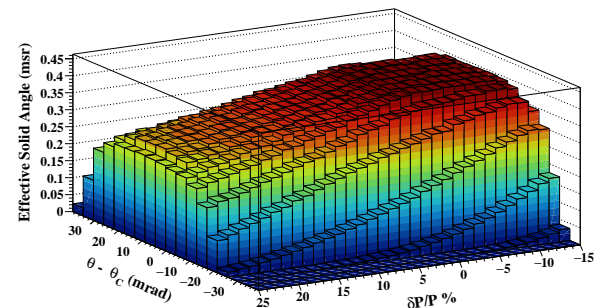


Figure 52: SHMS effective solid angle as a function of  $\delta P/P$  and  $\theta$ . SHMS  $\theta_{central} = 21^\circ$  and  $P_{central} = 3.3 \text{ GeV}/c$ .

2111 Fig. 53 shows the position and angular distribution  
 2112 of tracks formed from the drift chambers at the focal  
 2113 plane. A good agreement between the two reflects our  
 2114 understanding of both the magnetic forward transport  
 2115 and physical locations of the apertures which determine  
 the acceptance.

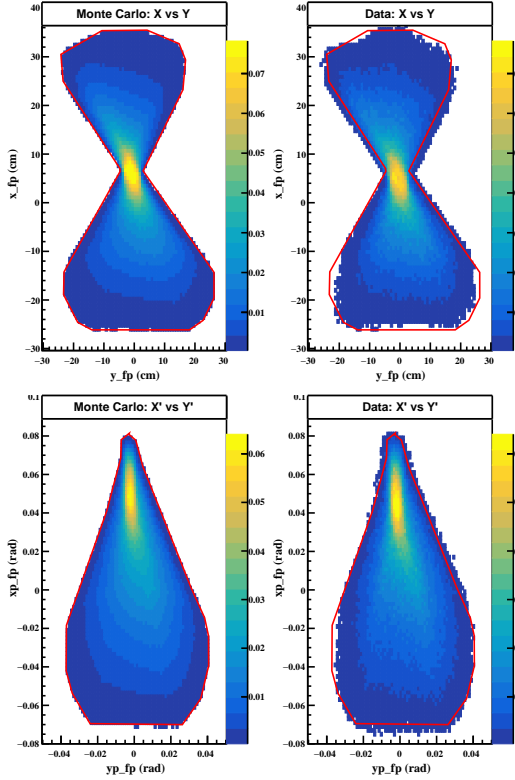


Figure 53: Comparison of focal plane quantities, simulation is on the left and data is on the right. The top plots are the position at the focal plane and the bottom is the angles at the focal plane determined from tracks formed by the drift chamber planes. The red outline represents the expected shape determined from simulation.

2116

2117 Fig. 54 demonstrates the agreement between simulation  
 2118 (after subtracting the cell walls) of the target  
 2119 variables  $Y_{tar}$ ,  $Y'_{tar}$ ,  $X'_{tar}$ , and  $\delta$  that were described in  
 2120 Sec. 3.1.

2121 To demonstrate how large the SHMS acceptance is in  
 2122  $Y_{tar}$ , one look at optics data taken during the A1N ex-  
 2123 periment. Fig. 55 plots the reconstructed position along  
 2124 the beam line,  $z_{tar}$  (which was reconstructed using the  
 2125 measured and  $Y'_{tar}$ ).

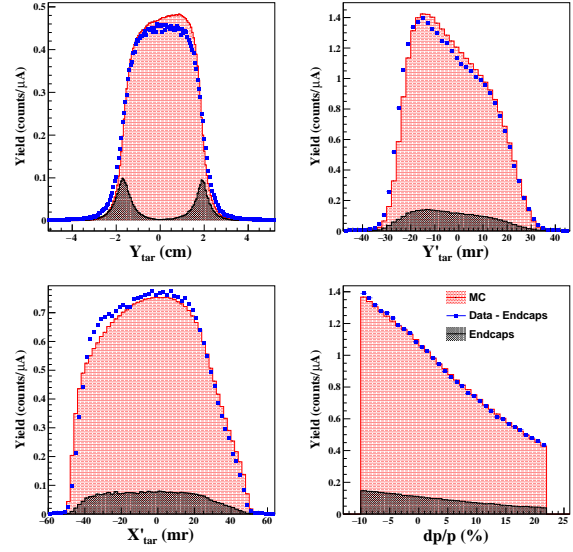


Figure 54: Target variable comparison of data versus Monte Carlo simulation from [10]. After subtracting the aluminum cell walls (black histogram) of the hydrogen target using dummy foil data, the agreement between data (blue histogram) and Monte Carlo (red histogram) is reasonable.

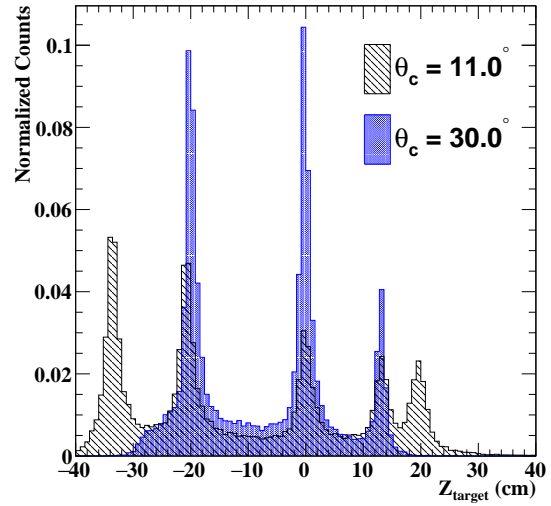


Figure 55: Reconstructed  $z_{tar}$  for a carbon foil optics target at SHMS central angles of  $11^\circ$  and  $30^\circ$ . Carbon foils were located at approximately -20, 0, 13.3 and 20.0 cm. The peak located at -35 cm is from the beam pipe exit window. The target chamber was not under vacuum and therefore a background from air is present in the data and not subtracted here.

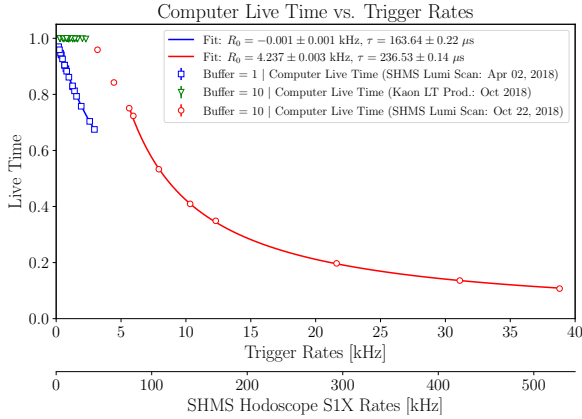


Figure 56: Computer live time vs. trigger rates (top x-axis) and SHMS hodoscope S1X plane rates (bottom x-axis) for DAQ buffer levels 1 and 10.

## 6.2. Rates and Livetime

### 6.2.1. Deadtime Measurement by Electronic Pulse Generator

The computer live time efficiency of the DAQ is defined as,

$$\epsilon_{\text{CLT}} = \frac{N_{(\text{phy}+\text{edtm}),\text{TDC}} - N_{(\text{edtm}),\text{TDC}}}{N_{(\text{phy}+\text{edtm}),\text{SCL}} - N_{(\text{edtm}),\text{SCL}}} \quad (13)$$

where the numerator is the total number of EDTM-subtracted TDC counts (total accepted physics triggers) and the denominator is the total number of EDTM-subtracted scaler counts (total physics pre-triggers). The EDTM introduces a bias in the computer live time calculation and must therefore be subtracted from the physics trigger. The bias comes from the fact that the EDTM is a clock and cannot be blocked by another EDTM signal, thereby having no contribution to the deadtime of the system. An additional bias arises during beam-off time periods, where only EDTM triggers are counted. To remove this bias, a beam current cut was required in the live time calculation.

The computer live time data shown in Fig. 56 is plotted against the un-prescaled input trigger rates (top x-axis) and the first plane (S1X) of the SHMS Hodoscopes (bottom-axis). The data were obtained from the SHMS luminosity scans and the Kaon LT experimental data taken on Fall 2018. The Spring 2018 scans (blue squares) were taken with DAQ in buffer level 1 (unbuffered mode) and the Kaon LT data (green triangles) and Fall 2018 scans (red circles) were with the DAQ in buffer level 10 (buffered mode). The advantage of buffered mode is that the DAQ is capable of accepting higher trigger rates while keeping the computer live

time efficiency  $\sim 100\%$ . Both buffered and unbuffered modes exhibit a characteristic fall-off of the live time as a function of the trigger rate which has been modeled using the fit function,

$$f_{\epsilon_{\text{CLT}}}(R) \equiv \frac{1}{1 + (R - R_0)\tau}, \quad (14)$$

where  $R$  is the input trigger rate,  $R_0$  describes a horizontal offset between the unbuffered and buffered modes and  $\tau$  represents the averaged data readout time (dead-time) before the DAQ is ready to accept another pre-trigger. The fit function, however, is unable to describe the “flat” region where the live time is nearly 100%. From the fit parameters, the fall-off behavior of buffered mode starts at trigger rates,  $R \sim 1/\tau$ , which corresponds to a numerical values of  $\sim 4.2$  kHz before a significant drop in the live time is observed.

As of Fall 2018, the DAQ has been operated in buffered mode which has proved to be more feasible for current and future high-rate experiments at Hall C.

## 6.3. Subsystem Performance

### 6.3.1. Hodoscope Performance

All hodoscope scintillator paddles and the PMTs used to build the S1X, S1Y, and S2X planes were extensively tested during assembly: the dark current and the gain as a function of the high voltage were measured for each tube; the finished paddles were light-leak tested and their detection efficiency as a function of position along the paddle was measured using cosmic rays on an automated test stand. A typical gain versus HV graph is shown in Fig. 57.

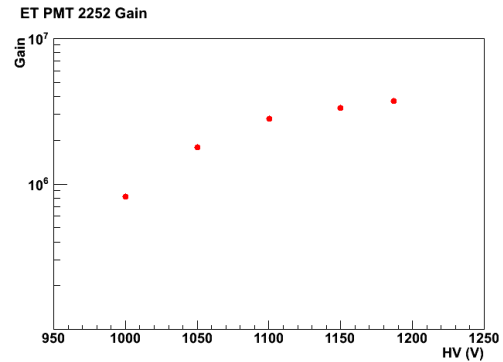


Figure 57: Gain versus high voltage graph for an ET tube used for the scintillator hodoscope.

2166 Once installed in the SHMS detector hut all paddles  
 2167 were retested and gain matched. During the Hall C com-  
 2168 missioning experiments carried out during the Spring  
 2169 2018 the scintillators performed as expected with no  
 2170 major problems. [Might want to put more text/a picture](#)  
 2171 [here, maybe time resolution, efficiency, etc?](#)

2172 The performance of the quartz plane (S2Y) was stud-  
 2173 ied with beam during the Hall C commissioning in Fall  
 2174 of 2017. A plot of the photoelectron response from most  
 2175 bars in the quartz plane is shown in Fig. 58 and Fig. 59.  
 2176 Only electrons with an incident angle close to  $90^\circ$  were  
 2177 chosen here to eliminate the bias coming from possibly  
 2178 reduced photon collection efficiency due to sub-optimal  
 2179 angles of the photon cones. All PMTs and optical cou-  
 2180 plings performed satisfactory.

2181 The threshold for Cherenkov light production in the  
 2182 quartz bars for electrons, pions, kaons and protons is  
 2183 shown in Fig. fig:TBD. Beam data confirmed the expect-  
 2184 ation that the detection efficiency for low momentum  
 2185 protons, for example, will be smaller than that for pi-  
 2186 ons or electrons simply due to the reduced number of  
 2187 Cherenkov photons that particles close to their firing  
 2188 threshold will produce. This is exemplified by Fig. 60,  
 2189 Fig. 61 and Fig. 62.

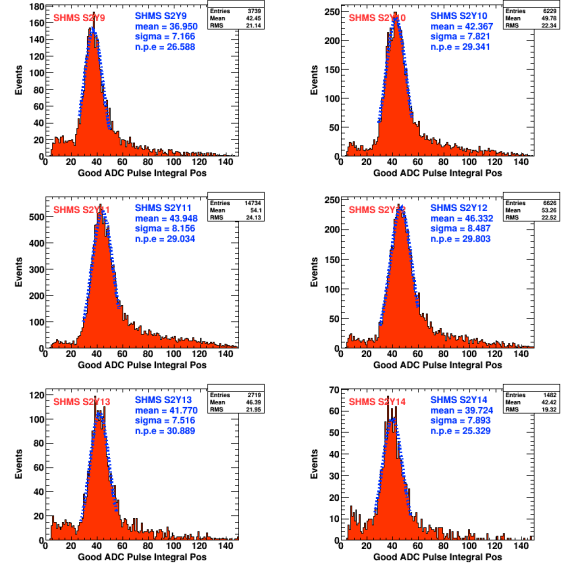


Figure 59: Number of photoelectrons response from the quartz plane.

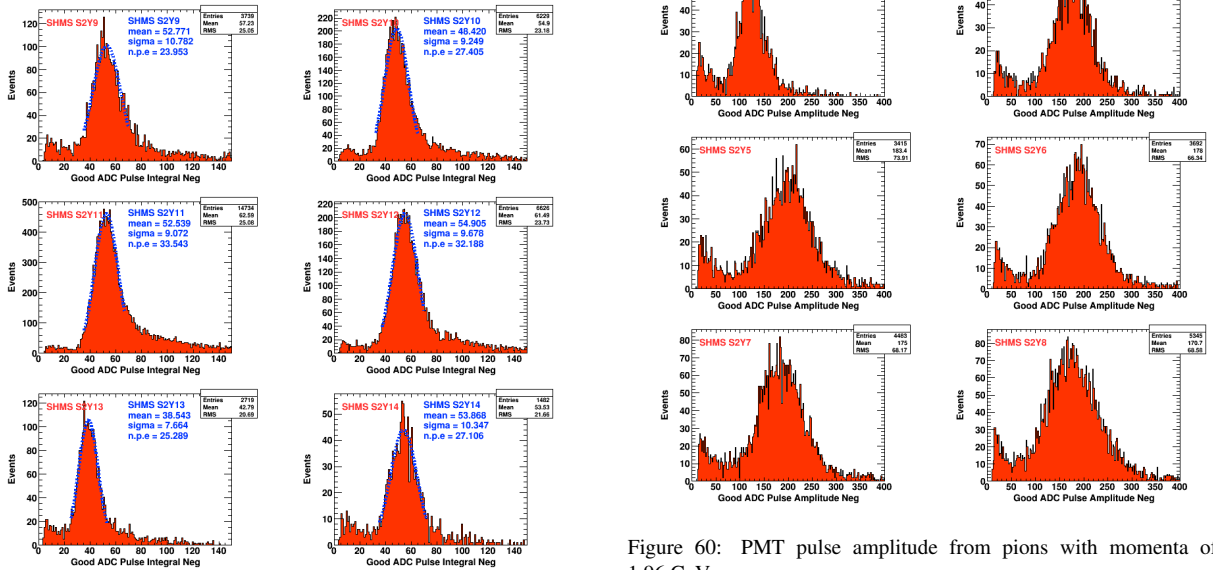


Figure 58: Number of photoelectrons response from the quartz plane.

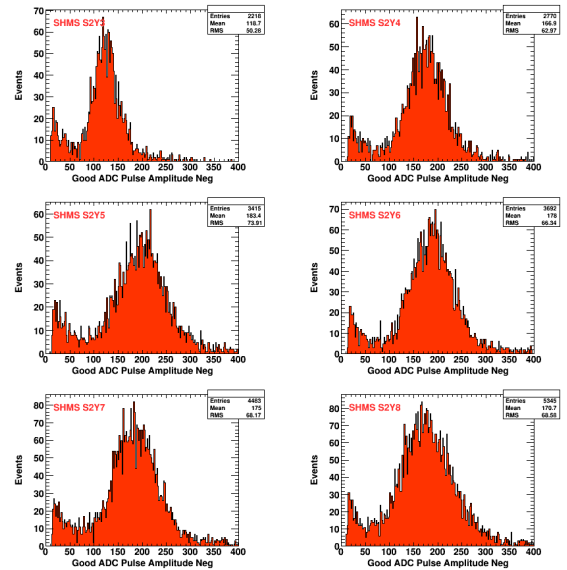


Figure 60: PMT pulse amplitude from pions with momenta of 1.96 GeV.

### 2190 6.3.2. DC Performance

2191 The SHMS drift chambers have proven to provide reli-  
 2192 able tracking for electrons and hadrons across a broad  
 2193 range of momenta. The drift chambers have also per-  
 2194 formed very well at high rate, with tracking efficiencies

2195 exceeding 96%, even at trigger rates over 2 MHz. The  
 2196 tracking efficiency as a function of the SIX hodoscope  
 2197 trigger rate (a good proxy for the overall event rate) in  
 2198 the SHMS can be seen in Figs. 63 and 64.

[Comment on tracking resolution?](#)

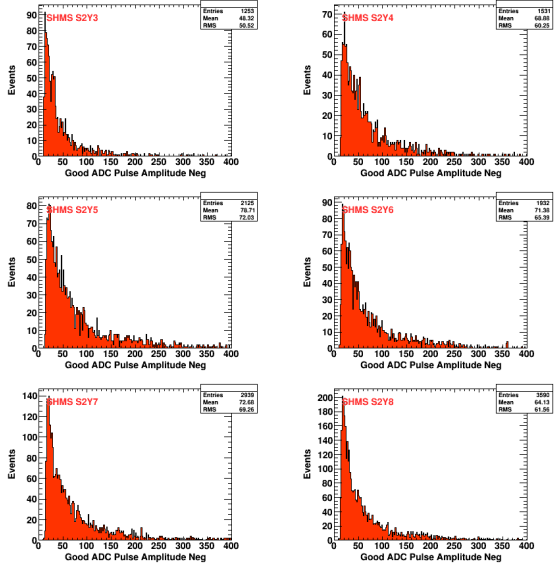


Figure 61: PMT pulse amplitude from protons with momenta of 1.96 GeV.

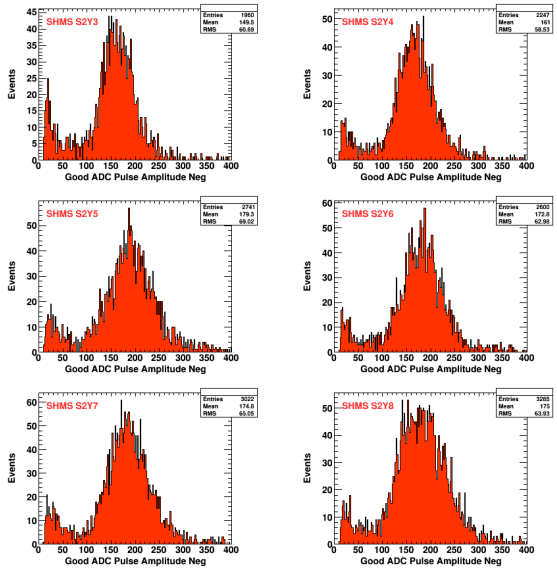


Figure 62: PMT pulse amplitude from protons with momenta of 5.05 GeV.

### 6.3.3. HGC Performance

The performance of the HGC is determined by the capacity to separate particle species on the basis of produced number of photoelectrons (NPE). In particular, the HGC is a threshold Cherenkov detector and thus identifies species based on whether or not a signal greater than 1.5 NPE was generated or not. The first metrics of performance to be discussed are the detector

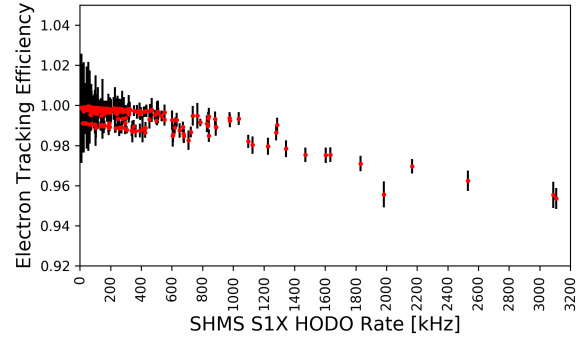


Figure 63: The SHMS electron tracking efficiency as a function of the S1X hodoscope trigger rate.

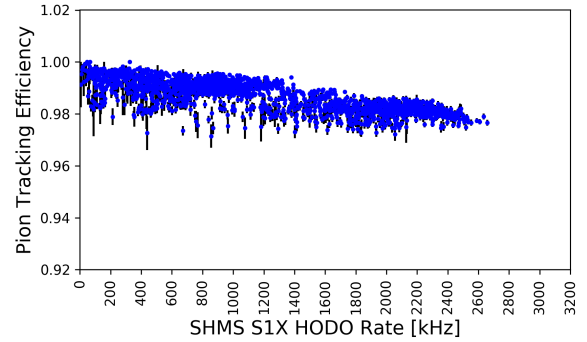


Figure 64: The SHMS pion tracking efficiency as a function of the S1X hodoscope trigger rate.

efficiency and contamination.

Efficiency in this context refers to the ratio of events selected as a particular particle species by all detectors in the SHMS, including the HGC, over the number of events selected as that same species without any information from the HGC. This is illustrated by the equation

$$\eta_{\text{HGC}} = \frac{\pi^+ \text{ detected with HGC signal}}{\pi^+ \text{ detected without HGC signal}}, \quad (15)$$

where  $\eta_{\text{HGC}}$  represents the detector efficiency of the HGC and  $\pi^+$  particle type is used as an example. The selection criteria includes cuts on the timing information, reconstructed  $\beta$ , calorimeter, aerogel and HGC information, and a single reconstructed track. Contamination refers to the number of events identified as a sub-threshold particle by the calorimeter and aerogel Cherenkov, but produced more than 1.5 NPE in the HGC. For example, if the HGC is configured for  $\pi^+/K^+$

2224 separation, the  $K^+$  contamination is defined as the number of events identified as a  $K^+$  by all detectors, except the HGC, which identified a  $\pi^+$ .

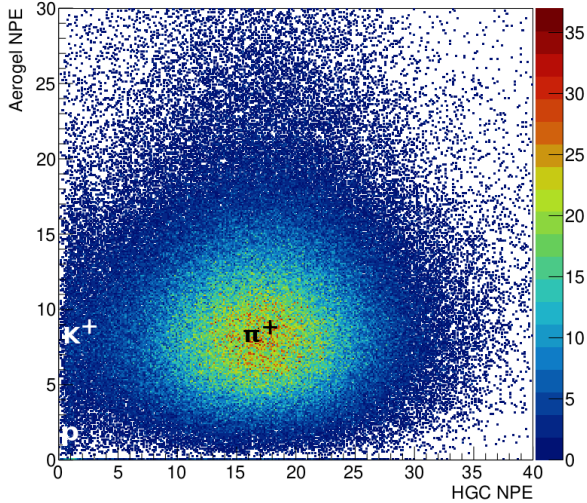


Figure 65: Demonstration of the particle identification capability of the Heavy Gas Cherenkov. Pictured is the separation between  $\pi^+$ ,  $K^+$  and proton at the 8.186 GeV beam energy and 6.053 GeV/c SHMS central momentum. The refractive indexes of HGC and aerogel Cherenkov detectors are 1.00143 and 1.011, respectively.

2227 Two runs are chosen to show HGC efficiency and contamination, one where the HGC separated between  $e^-/\pi^-$  and the other  $\pi^+/K^+$ . The former featured the HGC filled with  $\text{CO}_2$  at 1 atm and a SHMS central momentum of  $-3.0 \text{ GeV}/c^2$ . Particle identification was established by a cut on the normalized calorimeter energy. The latter had the HGC filled with  $\text{C}_4\text{F}_{10}$  at 1 atm, giving a  $\pi$  momentum threshold of  $2.8 \text{ GeV}/c^2$  and a  $K$  momentum threshold of  $9.4 \text{ GeV}/c^2$ , at a SHMS central momentum of  $+5.05 \text{ GeV}/c^2$ . Particle identification was performed by a cut on the aerogel Cherenkov detector and the normalized calorimeter energy. The spectrum obtained for the  $\pi^+/K^+$  separation is shown in Fig. 65. This figure illustrates the broad distribution of NPE produced by  $\pi$ , fit with the red curve, which are above their momentum threshold. At the lower end of the NPE axis, there is a very large number of events producing

PID Configuration	Efficiency	Contamination
$e^-/\pi^-$	95.99%	10000 : 1
$\pi^+/K^+$	98.22%	1000 : 1

Table 5: Summary of the Heavy Gas Cherenkov performance in separating between particle species. Efficiency is based on a photoelectron cut greater than 1.5.

2244 no light, or just the SPE. These events correspond to  $K$  since they are below the momentum threshold to produce Cherenkov light. The presence of the SPE is likely due to  $\delta$ -rays, or knock-on  $e^-$ , a phenomenon where a kaon can ionize the Cherenkov media and produce  $e^-$  which produce Cherenkov radiation. The vertical blue line indicates the NPE threshold, above which events are identified as  $\pi$ , below which are  $K$ . The summary of the particle identification efficiency and contamination is shown in Table 5

2248 Lastly, measurements of the  $\pi$  efficiency across a variety of momentum settings can be used to verify the index of refraction of the Cherenkov media. The relationship between  $\pi$  efficiency and momentum is fit with the equation [71]

$$\eta_{HGC} = 1 - e^{-(p-p_0)/\Gamma}, \quad (16)$$

2254 where  $\eta_{HGC}$  is the detector efficiency,  $p$  is the momentum of the  $\pi$ , and  $p_0$  and  $\Gamma$  are free parameters. Data taken in the range of  $2.53 \text{ GeV}/c$  to  $5.05 \text{ GeV}/c$  with the HGC filled with  $\text{C}_4\text{F}_{10}$  yields an index of refraction of  $n = 1.001 \pm 0.002$ . This is in agreement with the accepted value of  $n = 1.00143$  [72].

#### 6.3.4. NGC Performance

2261 The primary purpose of the NGC in the SHMS is to distinguish electrons from pions. Typically, PID is determined utilising a cut on the number of photoelectrons detected in the NGC. This cut is usually set at **X photoelectrons**. As this is a threshold Cherenkov, any events with less than the cutoff are identified as pions (or heavier hadron) and any with more than the cutoff are electrons.

[Comment/discussion on the NGC performance.](#)

#### 6.3.5. Aerogel Performance

PID Configuration	Efficiency	Contamination
$K^+/p$	99.94%	1000 : 1

Table 6: Aerogel performance for kaon-proton separation with efficiency based off of cut greater than 1.5 photoelectrons.

2271 The primary use of the aerogel Cherenkov detector in the SHMS is to distinguish between kaons and protons. A variety of aerogel tile refractive indices are used to cover a range of momenta. A cut of greater than 1.5 photoelectron (NPE) is used to cleanly identify particles. Fig. 65 shows the particle identification of the Heavy Gas Cherenkov as well as the aerogel Cherenkov detector. This figure shows the importance of having



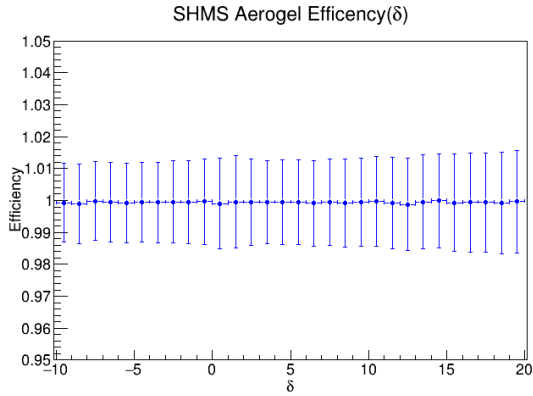


Figure 66: The efficiency of the aerogel is plotted over a range of  $\delta$ . This efficiency is taken at a beam energy of 6.2 GeV for an SHMS central momentum of 3.486 GeV/c. The refractive index of the aerogel detector is 1.015.

both the Heavy Gas and the aerogel Cherenkov detectors as the kaon and proton would be indistinguishable without the aerogel.

In order to get clean kaon samples, a high detector efficiency in the aerogel is required. The efficiency is determined by -

$$\eta_{\text{aero}} = \frac{K^+ \text{ detected with aerogel signal}}{K^+ \text{ detected without aerogel signal}}, \quad (17)$$

where the detector efficiency is represented by  $\eta_{\text{aero}}$ . The efficiency of the aerogel detector can be seen in Table 6. It is clear that the aerogel has a very high efficiency as required, crucially though, this efficiency also runs over the full range of  $\delta$  as seen in Fig. 66. This, plus the ability to change refractive indices, allows for terrific kaon identification over a wide range of kinematics.

### 6.3.6. Calorimeter Performance

**Material on the gain stability/consistency to be added (resolution versus run number for a time period, or mip peak position versus run number).**

The performance of the SHMS calorimeter under the beam conditions was tested first time during 12 GeV Hall C Key Performance Parameter Run in spring of 2017. As part of the SHMS detector package, the calorimeter was commissioned in the Hall C fall run period of the same year. The first experimental data with use of the calorimeter is being collected for a series 12 GeV Hall C experiments:

- E12-10-002 ( $F_2$  structure function at large  $x$ ) [10]

- E12-06-107 (Search for Color Transparency) [13]
- E12-10-008 (EMC effect) [11]
- E12-10-003 (Deuteron Electro-Disintegration) [14]
- E12-09-017 ( $P_t$  dependence of SIDIS cross section) [17]
- E12-09-002 (Precise  $\pi^+/\pi^-$  ratios in SIDIS) [18]
- E12-09-011 (L/T separated  $p(e, e'K)$  factorization test) [19]

As discussed briefly in Sec. 3.9.8,  $E_{\text{Norm}}$  should be 1 for electrons. This quantity can be utilised for PID. In the few GeV/c range, pions and electrons are well separated as can be seen in Fig. 7. The early analyses of the calorimeter data also demonstrate satisfactory performance of the detector in terms of resolution, as demonstrated in Fig. 67.

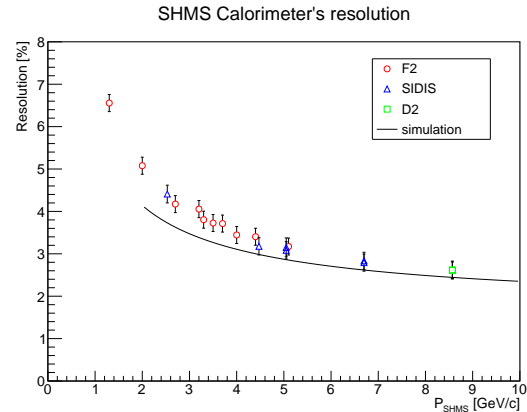


Figure 67: Resolution of the SHMS calorimeter from calibrations of runs from the Spring 18 run period. The solid line is result from the early simulations. **[This figure is not final.]**

## 7. Conclusion

The SHMS has been in service for a number of years. Through a range of experiments that utilised a broad range of run conditions, the SHMS has demonstrated itself to be a reliable and stable spectrometer. Both in terms of its ion optics, and its detector package.

Numerous experiments have completed and published high profile results since the SHMS was commissioned in 2017. This includes many high profile results on color transparency [73, 74], the EMC effect [75], deuteron structure [76] and proton structure [77]. This

2333 also extends to detailed studies of the proton's gravita- 2395  
2334 tional form factors [78]. 2396

2335 Many more high profile scientific results are expected 2397  
2336 in the near future, with several experimental campaigns 2398  
2337 now completed and data analysis in advanced stages. 2399  
2338 Due to the design parameters of the SHMS, it could also 2400  
2339 be utilised extensively in an upgraded, 22 GeV Jefferson 2401  
2340 Lab Scenario. Some possible experiments and scenarios 2402  
2341 that utilise the SHMS in a 22 GeV era are outlined in an 2403  
2342 upcoming 22 GeV white paper [79]. 2404  
2405  
2406  
2407

2343 [1] I. Niculescu, C. S. Armstrong, J. Arrington, K. A. Assama- 2408  
2344 gan, O. K. Baker, D. H. Beck, C. W. Bochna, R. D. Carlini, 2409  
2345 J. Cha, C. Cothran, D. B. Day, J. A. Dunne, D. Dutta, R. Ent, 2410  
2346 B. W. Filippone, V. V. Frolov, H. Gao, D. F. Geesaman, P. L. J. 2411  
2347 Gueye, W. Hinton, R. J. Holt, H. E. Jackson, C. E. Keppel, 2412  
2348 D. M. Koltenuk, D. J. Mack, D. G. Meekins, M. A. Miller, J. H. 2413  
2349 Mitchell, R. M. Mohring, G. Niculescu, D. Potterveld, J. W. 2414  
2350 Price, J. Reinhold, R. E. Segel, P. Stoler, L. Tang, B. P. Terburg, 2415  
2351 D. Van Westrum, W. F. Vulcan, S. A. Wood, C. Yan, B. Zeidman, 2416  
2352 Experimental verification of quark-hadron duality, Phys. Rev. 2417  
2353 Lett. 85 (2000) 1186–1189. doi:10.1103/PhysRevLett.85. 2418  
2354 1186. 2419

2355 [2] V. Tvaskis, M. E. Christy, J. Arrington, R. Asaturyan, O. K. 2420  
2356 Baker, H. P. Blok, P. Bosted, M. Boswell, A. Bruell, A. Cochran, 2421  
2357 L. Cole, J. Crowder, J. Dunne, R. Ent, H. C. Fenker, B. W. Filip- 2422  
2358 ponne, K. Garrow, A. Gasparian, J. Gomez, H. E. Jackson, C. E. 2423  
2359 Keppel, E. Kinney, L. Lapiak, Y. Liang, W. Lorenzon, A. Lung, 2424  
2360 D. J. Mack, J. W. Martin, K. McIlhany, D. Meekins, R. G. Mil- 2425  
2361 ner, J. H. Mitchell, H. Mkrтчyan, B. Moreland, V. Nazaryan, 2426  
2362 I. Niculescu, A. Opper, R. B. Piercey, D. H. Potterveld, B. Rose, 2427  
2363 Y. Sato, W. Seo, G. Smith, K. Spurlock, G. van der Steen- 2428  
2364 hoven, S. Stepanyan, V. Tadevosian, A. Uzzle, W. F. Vulcan, 2429  
2365 S. A. Wood, B. Zihlmann, V. Ziskin, Longitudinal-transverse 2430  
2366 separations of deep-inelastic structure functions at low  $Q^2$  for 2431  
2367 hydrogen and deuterium, Phys. Rev. Lett. 98 (2007) 142301. 2432  
2368 doi:10.1103/PhysRevLett.98.142301. 2433

2369 [3] J. Volmer, D. Abbott, H. Anklin, C. Armstrong, J. Arrington, 2434  
2370 K. Assamagan, S. Avery, O. K. Baker, H. P. Blok, C. Bochna, 2435  
2371 E. J. Brash, H. Breuer, N. Chant, J. Dunne, T. Eden, R. Ent, 2436  
2372 D. Gaskell, R. Gilman, K. Gustafsson, W. Hinton, G. M. Hu- 2437  
2373 ber, H. Jackson, M. K. Jones, C. E. Keppel, P. H. Kim, W. Kim, 2438  
2374 A. Klein, D. Koltenuk, M. Liang, G. J. Lolos, A. Lung, D. J. 2439  
2375 Mack, D. McKee, D. Meekins, J. Mitchell, H. Mkrтчyan, 2440  
2376 B. Mueller, G. Niculescu, I. Niculescu, D. Pitz, D. Potterveld, 2441  
2377 L. M. Qin, J. Reinhold, I. K. Shin, S. Stepanyan, V. Tade- 2442  
2378 vosyan, L. G. Tang, R. L. J. van der Meer, K. Vansyoc, 2443  
2379 D. Van Westrum, W. Vulcan, S. Wood, C. Yan, W.-X. Zhao, 2444  
2380 B. Zihlmann, Measurement of the charged pion electromag- 2445  
2381 netic form factor, Phys. Rev. Lett. 86 (2001) 1713–1716. doi: 2446  
2382 10.1103/PhysRevLett.86.1713. 2447

2383 [4] T. Horn, K. Aniol, J. Arrington, B. Barrett, E. J. Beise, H. P. 2448  
2384 Blok, W. Boeglin, E. J. Brash, H. Breuer, C. C. Chang, M. E. 2449  
2385 Christy, R. Ent, D. Gaskell, E. Gibson, R. J. Holt, G. M. Hu- 2450  
2386 ber, S. Jin, M. K. Jones, C. E. Keppel, W. Kim, P. M. King, 2451  
2387 V. Kovaltchouk, J. Liu, G. J. Lolos, D. J. Mack, D. J. Margazi- 2452  
2388 otis, P. Markowitz, A. Matsumura, D. Meekins, T. Miyoshi, 2453  
2389 H. Mkrтчyan, I. Niculescu, Y. Okayasu, L. Pentchev, C. Per- 2454  
2390 drisat, D. Potterveld, V. Punjabi, P. Reimer, J. Reinhold, 2455  
2391 J. Roche, P. G. Roos, A. Sarty, G. R. Smith, V. Tadevosyan, 2456  
2392 L. G. Tang, V. Tvaskis, S. Vidakovic, J. Volmer, W. Vulcan, 2457  
2393 G. Warren, S. A. Wood, C. Xu, X. Zheng, Determination of the 2458  
2394 pion charge form factor at  $Q^2 = 1.60$  and  $2.45$  (GeV/c) $^2$ , Phys.

Rev. Lett. 97 (2006) 192001. doi:10.1103/PhysRevLett. 2395  
97.192001. 2396

[5] T. Navasardyan, G. S. Adams, A. Ahmidouch, T. Ange- 2397  
lescu, J. Arrington, R. Asaturyan, O. K. Baker, N. Ben- 2398  
mouna, C. Bertoncini, H. P. Blok, W. U. Boeglin, P. E. Bosted, 2399  
H. Breuer, M. E. Christy, S. H. Connell, Y. Cui, M. M. 2400  
Dalton, S. Danagoulian, D. Day, T. Dodario, J. A. Dunne, 2401  
D. Dutta, N. El Khayari, R. Ent, H. C. Fenker, V. V. Frolov, 2402  
L. Gan, D. Gaskell, K. Hafidi, W. Hinton, R. J. Holt, T. Horn, 2403  
G. M. Huber, E. Hungerford, X. Jiang, M. Jones, K. Joo, 2404  
N. Kalantarians, J. J. Kelly, C. E. Keppel, V. Kubarovski, 2405  
Y. Li, Y. Liang, S. Malace, P. Markowitz, E. McGrath, P. Mc- 2406  
Kee, D. G. Meekins, H. Mkrтчyan, B. Moziak, G. Niculescu, 2407  
I. Niculescu, A. K. Opper, T. Ostapenko, P. Reimer, J. Rein- 2408  
hold, J. Roche, S. E. Rock, E. Schulte, E. Segbefia, C. Smith, 2409  
G. R. Smith, P. Stoler, V. Tadevosyan, L. Tang, M. Ungaro, 2410  
A. Uzzle, S. Vidakovic, A. Villano, W. F. Vulcan, M. Wang, 2411  
G. Warren, F. Wesselmann, B. Wojtsekhowski, S. A. Wood, 2412  
C. Xu, L. Yuan, X. Zheng, H. Zhu, Onset of quark-hadron dual- 2413  
ity in pion electroproduction, Phys. Rev. Lett. 98 (2007) 022001. 2414  
doi:10.1103/PhysRevLett.98.022001. 2415

[6] D. Abbott, A. Ahmidouch, T. A. Amaturi, C. Armstrong, J. Ar- 2416  
rington, K. A. Assamagan, K. Bailey, O. K. Baker, S. Bar- 2417  
row, K. Beard, D. Beatty, S. Beedoe, E. Beise, E. Belz, 2418  
C. Bochna, H. Breuer, E. E. W. Bruins, R. Carlini, J. Cha, 2419  
N. Chant, C. Cothran, W. J. Cummings, S. Danagoulian, D. Day, 2420  
D. DeSchepper, J.-E. Ducret, F. Duncan, J. Dunne, D. Dutta, 2421  
T. Eden, R. Ent, H. T. Fortune, V. Frolov, D. F. Geesaman, 2422  
H. Gao, R. Gilman, P. Guèye, J. O. Hansen, W. Hinton, R. J. 2423  
Holt, C. Jackson, H. E. Jackson, C. E. Jones, S. Kaufman, 2424  
J. J. Kelly, C. Keppel, M. Khandaker, W. Kim, E. Kinney, 2425  
A. Klein, D. Koltenuk, L. Kramer, W. Lorenzon, K. McFar- 2426  
lane, D. J. Mack, R. Madey, P. Markowitz, J. Martin, A. Mateos, 2427  
D. Meekins, M. A. Miller, R. Milner, J. Mitchell, R. Mohring, 2428  
H. Mkrтчyan, A. M. Nathan, G. Niculescu, I. Niculescu, T. G. 2429  
O'Neill, D. Potterveld, J. W. Price, J. Reinhold, C. Salgado, J. P. 2430  
Schiffer, R. E. Segel, P. Stoler, R. Suleiman, V. Tadevosyan, 2431  
L. Tang, B. Terburg, D. van Westrum, P. Welch, C. Williamson, 2432  
S. Wood, C. Yan, J.-C. Yan, J. Yu, B. Zeidman, W. Zhao, 2433  
B. Zihlmann, Quasifree ( $e, e'p$ ) reactions and proton propaga- 2434  
tion in nuclei, Phys. Rev. Lett. 80 (1998) 5072–5076. doi: 2435  
10.1103/PhysRevLett.80.5072. 2436

[7] K. Garrow, D. McKee, A. Ahmidouch, C. S. Armstrong, J. Ar- 2437  
rington, R. Asaturyan, S. Avery, O. K. Baker, D. H. Beck, H. P. 2438  
Blok, C. W. Bochna, W. Boeglin, P. Bosted, M. Bouwhuis, 2439  
H. Breuer, D. S. Brown, A. Bruell, R. D. Carlini, N. S. Chant, 2440  
A. Cochran, L. Cole, S. Danagoulian, D. B. Day, J. Dunne, 2441  
D. Dutta, R. Ent, H. C. Fenker, B. Fox, L. Gan, D. Gaskell, 2442  
A. Gasparian, H. Gao, D. F. Geesaman, R. Gilman, P. L. J. 2443  
Guèye, M. Harvey, R. J. Holt, X. Jiang, C. E. Keppel, E. Kin- 2444  
ney, Y. Liang, W. Lorenzon, A. Lung, D. J. Mack, P. Markowitz, 2445  
J. W. Martin, K. McIlhany, D. Meekins, M. A. Miller, R. G. 2446  
Milner, J. H. Mitchell, H. Mkrтчyan, B. A. Mueller, A. Nathan, 2447  
G. Niculescu, I. Niculescu, T. G. O'Neill, V. Papavassiliou, 2448  
S. Pate, R. B. Piercey, D. Potterveld, R. D. Ransome, J. Rein- 2449  
hold, E. Rollinde, P. Roos, A. J. Sarty, R. Sawafta, E. C. Schulte, 2450  
E. Segbefia, C. Smith, S. Stepanyan, S. Strauch, V. Tadevosyan, 2451  
L. Tang, R. Tieulent, A. Uzzle, W. F. Vulcan, S. A. Wood, 2452  
F. Xiong, L. Yuan, M. Zeier, B. Zihlmann, V. Ziskin, Nu- 2453  
clear transparency from quasielastic  $A(e, e'p)$  reactions up to 2454  
 $Q^2 = 8.1(\text{GeV}/c)^2$ , Phys. Rev. C 66 (2002) 044613. doi: 2455  
10.1103/PhysRevC.66.044613. 2456

[8] N. Fomin, J. Arrington, D. B. Day, D. Gaskell, A. Daniel, 2457  
J. Seely, R. Asaturyan, F. Benmokhtar, W. Boeglin, B. Boillat, 2458  
P. Bosted, A. Bruell, M. H. S. Bukhari, M. E. Christy, E. Chu- 2459

- 2460 dakov, B. Clasie, S. H. Connell, M. M. Dalton, D. Dutta, R. Ent, 2525  
 2461 L. El Fassi, H. Fenker, B. W. Filippone, K. Garrow, C. Hill, 2526  
 2462 R. J. Holt, T. Horn, M. K. Jones, J. Jourdan, N. Kalantarians, 2527  
 2463 C. E. Keppel, D. Kiselev, M. Kotulla, R. Lindgren, A. F. Lung, 2528  
 2464 S. Malace, P. Markowitz, P. McKee, D. G. Meekins, T. Miyoshi, 2529  
 2465 H. Mkrтчyаn, T. Navasardyan, G. Niculescu, Y. Okayasu, A. K. 2530  
 2466 Oppер, C. Perdrisat, D. H. Potterveld, V. Punjabi, X. Qian, P. E. 2531  
 2467 Reimer, J. Roche, V. M. Rodriguez, O. Rondon, E. Schulte, 2532  
 2468 E. Segbefia, K. Slifer, G. R. Smith, P. Solvignon, V. Tade- 2533  
 2469 vosyan, S. Tajima, L. Tang, G. Testa, R. Trojer, V. Tvaskis, W. F. 2534  
 2470 Vulcan, C. Wasko, F. R. Wesselmann, S. A. Wood, J. Wright, 2535  
 2471 X. Zheng, Scaling of the  $F_2$  structure function in nuclei and 2536  
 2472 quark distributions at  $x > 1$ , Phys. Rev. Lett. 105 (2010) 212502. 2537  
 2473 doi:10.1103/PhysRevLett.105.212502. 2538  
 [9] N. Fomin, J. Arrington, R. Asaturyan, F. Benmokhtar, 2539  
 2474 W. Boeglin, P. Bosted, A. Bruell, M. H. S. Bukhari, M. E. 2540  
 2475 Christy, E. Chudakov, B. Clasie, S. H. Connell, M. M. Dal- 2541  
 2476 ton, A. Daniel, D. B. Day, D. Dutta, R. Ent, L. El Fassi, 2542  
 2477 H. Fenker, B. W. Filippone, K. Garrow, D. Gaskell, C. Hill, 2543  
 2478 R. J. Holt, T. Horn, M. K. Jones, J. Jourdan, N. Kalantari- 2544  
 2480 ans, C. E. Keppel, D. Kiselev, M. Kotulla, R. Lindgren, A. F. 2545  
 2481 Lung, S. Malace, P. Markowitz, P. McKee, D. G. Meekins, 2546  
 2482 H. Mkrтчyаn, T. Navasardyan, G. Niculescu, A. K. Oppер, 2547  
 2483 C. Perdrisat, D. H. Potterveld, V. Punjabi, X. Qian, P. E. Reimer, 2548  
 2484 J. Roche, V. M. Rodriguez, O. Rondon, E. Schulte, J. Seely, 2549  
 2485 E. Segbefia, K. Slifer, G. R. Smith, P. Solvignon, V. Tade- 2550  
 2486 vosyan, S. Tajima, L. Tang, G. Testa, R. Trojer, V. Tvaskis, W. F. 2551  
 2487 Vulcan, C. Wasko, F. R. Wesselmann, S. A. Wood, J. Wright, 2552  
 2488 X. Zheng, New measurements of high-momentum nucleons and 2553  
 2489 short-range structures in nuclei, Phys. Rev. Lett. 108 (2012) 2554  
 2490 092502. doi:10.1103/PhysRevLett.108.092502. 2555  
 [10] S. Malace, M. Christy, C. Keppel, M. Niculescu, Precision mea- 2556  
 2492 surements of the  $F_2$  structure function at large  $x$  in the resonance 2557  
 2493 region and beyond, JLab Proposal E12-10-002. 2558  
 2494 URL [https://www.jlab.org/exp\\_prog/proposals/10/](https://www.jlab.org/exp_prog/proposals/10/PR12-10-002.pdf) 2559  
 2495 [PR12-10-002.pdf](https://www.jlab.org/exp_prog/proposals/10/PR12-10-002.pdf) 2560  
 [11] D. Gaskell, J. Arrington, A. Daniel, N. Fomin, Detailed studies 2561  
 2497 of the nuclear dependence of  $F_2$  in light nuclei, Jlab Proposal 2562  
 2498 E12-10-008. 2563  
 2499 URL [https://www.jlab.org/exp\\_prog/proposals/10/](https://www.jlab.org/exp_prog/proposals/10/PR12-10-008.pdf) 2564  
 2500 [PR12-10-008.pdf](https://www.jlab.org/exp_prog/proposals/10/PR12-10-008.pdf) 2565  
 [12] A. Karki, et al., First Measurement of the EMC effect in B10 and 2566  
 2502 B11, Phys. Rev. C 108 (3) (2023) 035201. arXiv:2207.03850, 2567  
 2503 doi:10.1103/PhysRevC.108.035201. 2568  
 [13] D. Dutta, R. Ent, The search for color transparency at 12 gev, 2569  
 2505 JLab Proposal E12-06-107. 2570  
 2506 URL [https://www.jlab.org/exp\\_prog/proposals/06/](https://www.jlab.org/exp_prog/proposals/06/PR12-06-107.pdf) 2571  
 2507 [PR12-06-107.pdf](https://www.jlab.org/exp_prog/proposals/06/PR12-06-107.pdf) 2572  
 [14] W. Boeglin, M. Jones, Deuteron electro-disintegration at very 2573  
 2509 high missing momentum, JLab Proposal E12-10-108. 2574  
 2510 URL [https://www.jlab.org/exp\\_prog/proposals/10/](https://www.jlab.org/exp_prog/proposals/10/PR12-10-003.pdf) 2575  
 2511 [PR12-10-003.pdf](https://www.jlab.org/exp_prog/proposals/10/PR12-10-003.pdf) 2576  
 [15] D. Bhetuwal, et al., Ruling out Color Transparency in Quasielas- 2577  
 2512 tic  $^{12}\text{C}(e,e'p)$  up to  $Q^2$  of 14.2 (GeV/c) $^2$ , Phys. Rev. Lett. 2578  
 2514 126 (8) (2021) 082301. arXiv:2011.00703, doi:10.1103/ 2579  
 2515 PhysRevLett.126.082301. 2580  
 [16] C. Yero, et al., Probing the Deuteron at Very Large Internal 2581  
 2517 Momenta, Phys. Rev. Lett. 125 (26) (2020) 262501. arXiv: 2582  
 2518 2008.08058, doi:10.1103/PhysRevLett.125.262501. 2583  
 [17] R. Ent, P. Bosted, E. Kinney, H. Mkrтчyаn, Transverse mo- 2584  
 2520 mentum dependence of semi-inclusive pion production, JLab 2585  
 2521 Proposal E12-09-017. 2586  
 2522 URL [https://www.jlab.org/exp\\_prog/PACpage/](https://www.jlab.org/exp_prog/PACpage/PAC38/proposals/Previously_Approved/E12-09-017_Update.pdf) 2587  
 2523 [PAC38/proposals/Previously\\_Approved/E12-09-017\\_](https://www.jlab.org/exp_prog/PACpage/PAC38/proposals/Previously_Approved/E12-09-017_Update.pdf) 2588  
 2524 [Update.pdf](https://www.jlab.org/exp_prog/PACpage/PAC38/proposals/Previously_Approved/E12-09-017_Update.pdf) 2589
- [18] K. Hafidi, D. Dutta, D. Gaskell, Precise measurement of 2590  
 $\pi^+/\pi^-$  ratios in semi-inclusive deep inelastic scattering part i: 2591  
 Charge symmetry violating quark distributions, JLab Proposal 2592  
 E12-09-002. 2593  
 URL [https://www.jlab.org/exp\\_prog/PACpage/](https://www.jlab.org/exp_prog/PACpage/PAC38/proposals/Previously_Approved/E12-09-002Update.pdf) 2594  
[PAC38/proposals/Previously\\_Approved/](https://www.jlab.org/exp_prog/PACpage/PAC38/proposals/Previously_Approved/E12-09-002Update.pdf) 2595  
[E12-09-002Update.pdf](https://www.jlab.org/exp_prog/PACpage/PAC38/proposals/Previously_Approved/E12-09-002Update.pdf) 2596
- [19] T. Horn and G. M. Huber, P. Markowitz, Studies of the l-t 2597  
 separated kaon electroproduction cross section from 5-11 gev, 2598  
 JLab Proposal E12-09-011. 2599  
 URL [https://www.jlab.org/exp\\_prog/PACpage/](https://www.jlab.org/exp_prog/PACpage/PAC38/proposals/Previously_Approved/E12-09-011_Update.pdf) 2600  
[PAC38/proposals/Previously\\_Approved/E12-09-011\\_](https://www.jlab.org/exp_prog/PACpage/PAC38/proposals/Previously_Approved/E12-09-011_Update.pdf) 2601  
[Update.pdf](https://www.jlab.org/exp_prog/PACpage/PAC38/proposals/Previously_Approved/E12-09-011_Update.pdf) 2602
- [20] B. Duran, et al., Determining the gluonic gravitational form 2603  
 factors of the proton, Nature 615 (7954) (2023) 813–816. arXiv: 2604  
 2207.05212, doi:10.1038/s41586-023-05730-4. 2605
- [21] R. Li, et al., Measured proton electromagnetic structure 2606  
 deviates from theoretical predictions, Nature 611 (7935) 2607  
 (2022) 265–270. arXiv:2210.11461, doi:10.1038/ 2608  
 s41586-022-05248-1. 2609
- [22] T. Horn, G. Huber, D. Gaskell et al., Study of the l-t separated 2610  
 pion electroproduction cross section at 11 gev and measurement 2611  
 of the charged pion form factor to high  $q^2$ , approved Jefferson 2612  
 Lab 12 GeV Experiment (2019). 2613  
 URL [http://www.jlab.org/exp\\_prog/proposals/19/](http://www.jlab.org/exp_prog/proposals/19/E12-19-006.pdf) 2614  
[E12-19-006.pdf](http://www.jlab.org/exp_prog/proposals/19/E12-19-006.pdf) 2615
- [23] X. Zheng, G. Cates, J. P. Chen, Z. E. Meziani et al., Mea- 2616  
 surement of neutron spin asymmetry  $aln$  in the valence quark 2617  
 region using an 11 gev beam and a polarized  $^3\text{He}$  target in hall 2618  
 c, approved Jefferson Lab 12 GeV Experiment (2006). 2619  
 URL [http://www.jlab.org/exp\\_prog/proposals/06/](http://www.jlab.org/exp_prog/proposals/06/PR12-06-110.pdf) 2620  
[PR12-06-110.pdf](http://www.jlab.org/exp_prog/proposals/06/PR12-06-110.pdf) 2621
- [24] B. Sawatzky, T. Averett, W. Korsch, Z. E. Meziani et al., 2622  
 A path to 'color polarizabilities' in the neutron: A precision 2623  
 measurement of the neutron  $g_2$  and  $d_2$  at high  $q^2$  in hall c, 2624  
 approved Jefferson Lab 12 GeV Experiment (2006). 2625  
 URL [http://www.jlab.org/exp\\_prog/proposals/06/](http://www.jlab.org/exp_prog/proposals/06/PR12-06-121.pdf) 2626  
[PR12-06-121.pdf](http://www.jlab.org/exp_prog/proposals/06/PR12-06-121.pdf) 2627
- [25] O. Hen, F. Hauenstein, D. Higinbotham, L. Weinstein et al., 2628  
 The cafe experiment: Short-range pairing mechanisms in heavy 2629  
 nuclei, approved Jefferson Lab 12 GeV Experiment (2017). 2630  
 URL [https://misportal.jlab.org/pacProposals/](https://misportal.jlab.org/pacProposals/proposals/1352/attachments/98357/Proposal.pdf) 2631  
[proposals/1352/attachments/98357/Proposal.pdf](https://misportal.jlab.org/pacProposals/proposals/1352/attachments/98357/Proposal.pdf) 2632
- [26] J. Arrington, D. Day, N. Fomin, P. Solvignon et al., Inclusive 2633  
 scattering from nuclei at  $x > 1$  in the quasielastic and deeply 2634  
 inelastic regimes, approved Jefferson Lab 12 GeV Experiment 2635  
 (2006). 2636  
 URL [http://www.jlab.org/exp\\_prog/proposals/06/](http://www.jlab.org/exp_prog/proposals/06/PR12-06-105.pdf) 2637  
[PR12-06-105.pdf](http://www.jlab.org/exp_prog/proposals/06/PR12-06-105.pdf) 2638
- [27] P. J. Griffin, T. F. Luera, F. W. S. P. J. Cooper, S. G. Karr, 2639  
 G. L. Hash, E. Fuller, The role of thermal and fission neutrons 2640  
 in reactor neutron-induced upsets in commercial systems, IEEE 2641  
 Transactions on Nuclear Science 44 (1997) 2079–2086. 2642
- [28] C. I. Underwood, The single-event-effect behaviour of 2643  
 commercial-off-the-shelf memory devices - a decade in the low- 2644  
 earth orbit, IEEE Transactions on Nuclear Science 45. 2645
- [29] T. Horn, SHMS Shielding Design, JLab Hall C Document 2646  
 Database 392-v1. 2647
- [30] W. R. Leo, Techniques for nuclear and particle physics exper- 2648  
 iments: a how-to approach; 2nd ed., Springer, Berlin, 1994. 2649  
 doi:10.1007/978-3-642-57920-2. 2650  
 URL <https://cds.cern.ch/record/302344> 2651
- [31] J. F. B. (ed.), Mcnp - a general monte carlo n-particle transport 2652  
 code version a, LA-12625-M, Los Alamos National Laboratory, 2653  
 Los Alamos, New Mexico. 2654

- [32] S. Wood, Private Communications (2008). 2655
- [33] M. Jones, *et al.*, Private Communication (2008). 2656
- [34] Y. Birenbaum, Z. Berant, S. Kahane, A. Wolf, R. Moreh, 2657  
 Absolute cross sections for  $(\gamma, n)$  transitions in lead, bis- 2658  
 muth, and terbium, Phys. Rev. C 51 (1995) 3496–3499. 2659  
 doi:10.1103/PhysRevC.51.3496. 2660  
 URL [https://link.aps.org/doi/10.1103/PhysRevC.](https://link.aps.org/doi/10.1103/PhysRevC.51.3496) 2661  
[51.3496](https://link.aps.org/doi/10.1103/PhysRevC.51.3496) 2662
- [35] D. Marsh, Particle practice, [https://concreteproducts.](https://concreteproducts.com/index.php/2014/02/14/particle-practice/) 2663  
[com/index.php/2014/02/14/particle-practice/](https://concreteproducts.com/index.php/2014/02/14/particle-practice/) 2664  
 (2014). 2665
- [36] T. Skwarnicki, Beam test of a c4f8o-mapmt rich prototype, 2666  
 Nuclear Instruments and Methods in Physics Research Section 2667  
 A: Accelerators, Spectrometers, Detectors and Associated 2668  
 Equipment 553 (1) (2005) 339–344, proceedings of the 2669  
 fifth International Workshop on Ring Imaging Detectors. 2670  
 doi:<https://doi.org/10.1016/j.nima.2005.08.070>. 2671  
 URL [https://www.sciencedirect.com/science/](https://www.sciencedirect.com/science/article/pii/S0168900205016219) 2672  
[article/pii/S0168900205016219](https://www.sciencedirect.com/science/article/pii/S0168900205016219) 2673
- [37] ASM Aerospace Specification Metals, 2501 NW 34th Pl #29, 2674  
 Pompano Beach, FL 33069, United States. 2675  
 URL <https://aerospacemetals.com/> 2676
- [38] Sinclair Glass, 105 N Wabash Ave, Hartford City, IN 47348, 2677  
 United States. 2678  
 URL <https://sinclairglass.com/> 2679
- [39] W. Li, Heavy gas cherenkov detector construction for hall c 2680  
 at thomas jefferson national accelerator facility, University of 2681  
 Regina, MSc Thesis (2012). 2682  
 URL <https://hdl.handle.net/10294/3818> 2683
- [40] Corning International, 1 Riverfront Plaza, Corning, NY 14831, 2684  
 United States. 2685  
 URL <https://www.corning.com/> 2686
- [41] Hamamatsu Photonics K.K., 314-5 Shimokanzo, Iwata, 2687  
 Shizuoka 438-0126, Japan. 2688  
 URL <http://www.hamamatsu.com/> 2689
- [42] Evaporated Coatings Inc., 2365 Maryland Rd, Willow Grove, 2690  
 PA 19090, United States. 2691  
 URL <https://evaporatedcoatings.com/> 2692
- [43] Rayotek Scientific, 8845 Rehco Rd, San Diego, CA 92121, 2693  
 United States. 2694  
 URL <https://rayotek.com/> 2695
- [44] Detector Technologies Group (CERN), espl. des Particules 1, 2696  
 1211 Meyrin, Switzerland. 2697  
 URL [https://ep-dep-dt.web.cern.ch/](https://ep-dep-dt.web.cern.ch/thin-film-glass-service) 2698  
[thin-film-glass-service](https://ep-dep-dt.web.cern.ch/thin-film-glass-service) 2699
- [45] ET Enterprises, 45 Riverside Way, Uxbridge UB8 2YF, United 2700  
 Kingdom. 2701  
 URL <http://et-enterprises.com/> 2702
- [46] T. Horn, *et al.*, The Aerogel Čerenkov detector for the SHMS 2703  
 magnetic spectrometer in Hall C at Jefferson Lab, Nucl. Instrum. 2704  
 Meth. A842 (2017) 28–47. arXiv:1607.05264, doi: 2705  
[10.1016/j.nima.2016.10.039](https://doi.org/10.1016/j.nima.2016.10.039). 2706
- [47] T. Horn, H. Mkrtchyan, S. Ali, A. Asaturyan, M. Carmignotto, 2707  
 A. Dittmann, D. Dutta, R. Ent, N. Hlavin, Y. Illieva, 2708  
 A. Mkrtchyan, P. Nadel-Turonski, I. Pegg, A. Ramos, J. Rein- 2709  
 hold, I. Sapkota, V. Tadevosyan, S. Zhamkochyan, S. Wood, 2710  
 The aerogel Čerenkov detector for the shms magnetic spectrom- 2711  
 eter in hall c at jefferson lab, Nuclear Instruments and Methods 2712  
 in Physics Research Section A: Accelerators, Spectrometers, 2713  
 Detectors and Associated Equipment 842 (2017) 28–47. 2714  
 doi:<https://doi.org/10.1016/j.nima.2016.10.039>. 2715  
 URL [https://www.sciencedirect.com/science/](https://www.sciencedirect.com/science/article/pii/S0168900216310774) 2716  
[article/pii/S0168900216310774](https://www.sciencedirect.com/science/article/pii/S0168900216310774) 2717
- [48] Gore, W. L. & Associates INC., 555 Paper Mill Road, Newark, 2718  
 DE 19711, United States. 2719
- URL <http://www.gore.com>
- [49] Millipore Corporation, 80 Ashly Road, Bedford, MA 01730. 2720  
 URL <http://www.millipore.com/>
- [50] I. Adachi, *et al.*, Study of highly transparent silica aerogel as 2721  
 a RICH radiator, Nucl. Instrum. Meth. A553 (2005) 146–151. 2722  
 doi:10.1016/j.nima.2005.08.022. 2723
- [51] E. Aschenauer, *et al.*, Optical characterization of  $n = 1.03$  2724  
 silica aerogel used as radiator in the RICH of HERMES. 2725  
 Nucl. Instrum. Meth. A440 (2000) 338–347. doi:10.1016/ 2726  
 S0168-9002(99)00923-7. 2727
- [52] T. Horn, G.M. Huber *et al.*, Scaling study of the l-t separated 2728  
 pion electroproduction cross section at 11 gev, approved 2729  
 Jefferson Lab 12 GeV Experiment (2007). 2730  
 URL [https://www.jlab.org/exp\\_prog/PACpage/](https://www.jlab.org/exp_prog/PACpage/PAC38/proposals/Previously_Approved/E12-07-105_Update.pdf) 2731  
[PAC38/proposals/Previously\\_Approved/E12-07-105\\_](https://www.jlab.org/exp_prog/PACpage/PAC38/proposals/Previously_Approved/E12-07-105_Update.pdf) 2732  
[Update.pdf](https://www.jlab.org/exp_prog/PACpage/PAC38/proposals/Previously_Approved/E12-07-105_Update.pdf) 2733
- [53] P. Bosted, R. Ent, E. Kinney *et al.*, Measurement of the ratio 2734  
 $r = \sigma_l/\sigma_r$  in semi-inclusive deep-inelastic regimes, approved 2735  
 Jefferson Lab 12 GeV Experiment (2006). 2736  
 URL [https://www.jlab.org/exp\\_prog/PACpage/](https://www.jlab.org/exp_prog/PACpage/PAC36/Proposals/previously%20approved/E12-06-104.pdf) 2737  
[PAC36/Proposals/previously%20approved/](https://www.jlab.org/exp_prog/PACpage/PAC36/Proposals/previously%20approved/E12-06-104.pdf) 2738  
[E12-06-104.pdf](https://www.jlab.org/exp_prog/PACpage/PAC36/Proposals/previously%20approved/E12-06-104.pdf) 2739
- [54] R. Asaturyan, *et al.*, The aerogel threshold Čerenkov detector 2740  
 for the high momentum spectrometer in Hall C at Jefferson Lab, 2741  
 Nucl. Instrum. Meth. A548 (2005) 364–374. arXiv:physics/ 2742  
 0411147, doi:10.1016/j.nima.2005.04.058. 2743
- [55] H. Mkrtchyan, R. Carlini, V. Tadevosyan, J. Arrington, 2744  
 A. Asaturyan, M. Christy, D. Dutta, R. Ent, H. Fenker, 2745  
 D. Gaskell, T. Horn, M. Jones, C. Keppel, D. Mack, 2746  
 S. Malace, A. Mkrtchyan, M. Niculescu, J. Seely, V. Tvaskis, 2747  
 S. Wood, S. Zhamkochyan, The lead-glass electromag- 2748  
 netic calorimeters for the magnetic spectrometers in hall 2749  
 c at jefferson lab, Nuclear Instruments and Methods in 2750  
 Physics Research Section A: Accelerators, Spectrometers, 2751  
 Detectors and Associated Equipment 719 (2013) 85–100. 2752  
 doi:<https://doi.org/10.1016/j.nima.2013.03.070>. 2753  
 URL [https://www.sciencedirect.com/science/](https://www.sciencedirect.com/science/article/pii/S0168900213004154) 2754  
[article/pii/S0168900213004154](https://www.sciencedirect.com/science/article/pii/S0168900213004154) 2755
- [56] Lytkarino optical glass plant, Iytkarino Optical Glass Factory, 2756  
 140061, Lytkarino, Moscow Oblast, Russia. 2757  
 URL <https://lzos.ru/>
- [57] H. Avakian, N. Bianchi, G. Capitani, E. De Sanctis, A. Fantoni, 2758  
 V. Giourdjian, R. Mozzetti, V. Muccifora, M. Nupieri, A. Re- 2759  
 olon, P. Rossi, J. van den Brand, M. Doets, T. Henkes, 2760  
 M. Kolstein, A. Airapetian, N. Akopov, M. Amarian, 2761  
 R. Avakian, A. Avetissian, V. Garibian, S. Taroian, P. Gal- 2762  
 lumian, A. Simon, B. Bray, B. Filippone, A. Lung, Performance 2763  
 of f101 radiation resistant lead glass shower counters, Nu- 2764  
 clear Instruments and Methods in Physics Research Section 2765  
 A: Accelerators, Spectrometers, Detectors and Associ- 2766  
 ated Equipment 378 (1) (1996) 155–161. doi:[https://doi.org/10.1016/0168-9002\(96\)00443-3](https://doi.org/10.1016/0168-9002(96)00443-3). 2767  
 URL [https://www.sciencedirect.com/science/](https://www.sciencedirect.com/science/article/pii/S0168900296004433) 2768  
[article/pii/S0168900296004433](https://www.sciencedirect.com/science/article/pii/S0168900296004433) 2769
- [58] T. Amatuni, G. Kazaryan, H. Mkrtchyan, V. Tadevosyan, 2770  
 W. Vulcan, A study of gain variation in philips xp-3462p 2771  
 photomultipliers, Nuclear Instruments and Methods in Physics 2772  
 Research Section A: Accelerators, Spectrometers, Detectors 2773  
 and Associated Equipment 374 (1) (1996) 39–47. doi:[https://doi.org/10.1016/0168-9002\(96\)37473-1](https://doi.org/10.1016/0168-9002(96)37473-1). 2774  
 URL [https://www.sciencedirect.com/science/](https://www.sciencedirect.com/science/article/pii/S0168900296374731) 2775  
[article/pii/S0168900296374731](https://www.sciencedirect.com/science/article/pii/S0168900296374731) 2776
- [59] C. Zorn, Private Communication (2008). 2777
- [60] S. Agostinelli, J. Allison, K. Amako, J. Apostolakis, H. Araujo, 2778  
 P. Arce, M. Asai, D. Axen, S. Banerjee, G. Barrand, F. Behner, 2779

- 2720 L. Bellagamba, J. Boudreau, L. Brogna, A. Brunengo, 2785  
2721 H. Burkhardt, S. Chauvie, J. Chuma, R. Chytrcek, G. Cooper- 2786  
2722 man, G. Cosmo, P. Degtyarenko, A. Dell'Acqua, G. Depaola, 2787  
2723 D. Dietrich, R. Enami, A. Feliciello, C. Ferguson, H. Fesefeldt, 2788  
2724 G. Folger, F. Foppiano, A. Forti, S. Garelli, S. Giani, R. Gian- 2789  
2725 nitrapani, D. Gibin, J. Gómez Cadenas, I. González, G. Gracia 2790  
2726 Abril, G. Greeniaus, W. Greiner, V. Grichine, A. Grossheim, 2791  
2727 S. Guatelli, P. Gumplinger, R. Hamatsu, K. Hashimoto, H. Ha- 2792  
2728 sui, A. Heikkinen, A. Howard, V. Ivanchenko, A. Johnson, 2793  
2729 F. Jones, J. Kallenbach, N. Kanaya, M. Kawabata, Y. Kawa- 2794  
2730 bata, M. Kawaguti, S. Kelner, P. Kent, A. Kimura, T. Kodama, 2795  
2731 R. Kokoulin, M. Kossov, H. Kurashige, E. Lamanna, T. Lampén, 2796  
2732 V. Lara, V. Lefebvre, F. Lei, M. Liendl, W. Lockman, F. Longo, 2797  
2733 S. Magni, M. Maire, E. Medernach, K. Minamimoto, P. Mora 2798  
2734 de Freitas, Y. Morita, K. Murakami, M. Nagamatu, R. Nar- 2799  
2735 tallo, P. Nieminen, T. Nishimura, K. Ohtsubo, M. Okamura, 2800  
2736 S. O'Neale, Y. Oohata, K. Paech, J. Perl, A. Pfeiffer, M. Pia, 2801  
2737 F. Ranjard, A. Rybin, S. Sadilov, E. Di Salvo, G. Santin, 2802  
2738 T. Sasaki, N. Savvas, Y. Sawada, S. Scherer, S. Sei, V. Sirotenko, 2803  
2739 D. Smith, N. Starkov, H. Stoecker, J. Sulkimo, M. Takahata, 2804  
2740 S. Tanaka, E. Tcherniaev, E. Safai Tehrani, M. Tropeano, P. Tr- 2805  
2741 uscotti, H. Uno, L. Urban, P. Urban, M. Verderi, A. Walkden, 2806  
2742 W. Wander, H. Weber, J. Wellisch, T. Wenaus, D. Williams, 2807  
2743 D. Wright, T. Yamada, H. Yoshida, D. Zschesche, [Geant4—a](#) 2808  
2744 [simulation toolkit](#), Nuclear Instruments and Methods in Physics 2809  
2745 Research Section A: Accelerators, Spectrometers, Detectors 2810  
2746 and Associated Equipment 506 (3) (2003) 250–303. doi: 2811  
2747 [https://doi.org/10.1016/S0168-9002\(03\)01368-8](https://doi.org/10.1016/S0168-9002(03)01368-8). 2812  
2748 URL [https://www.sciencedirect.com/science/](https://www.sciencedirect.com/science/article/pii/S0168900203013688) 2813  
2749 [article/pii/S0168900203013688](https://www.sciencedirect.com/science/article/pii/S0168900203013688) 2814  
2750 [61] J. Apostolakis, G. Folger, V. Grichine, A. Heikkinen, 2815  
2751 A. Howard, V. Ivanchenko, P. Kaitaniemi, T. Koi, M. Kosov, 2816  
2752 J. M. Quesada, A. Ribon, V. Uzhinskiy, D. Wright, [Progress](#) 2817  
2753 [in hadronic physics modelling in geant4](#), Journal of Physics: 2818  
2754 Conference Series 160 (1) (2009) 012073. doi:10.1088/ 2819  
2755 1742-6596/160/1/012073. 2820  
2756 URL [https://dx.doi.org/10.1088/1742-6596/160/1/](https://dx.doi.org/10.1088/1742-6596/160/1/012073) 2821  
2757 [012073](https://dx.doi.org/10.1088/1742-6596/160/1/012073) 2822  
2758 [62] M. Born, E. Wolf, Principles of Optics, 3rd Edition, Pergamon 2823  
2759 Press, 1965. 2824  
2760 [63] Ts. Amatuni, On the calibration of segmented full absorption 2825  
2761 calorimeters, unpublished (1995). 2826  
2762 [64] JLab DAQ Group, [Cebaf online data acquisition system \(coda\)](#). 2827  
2763 URL <https://coda.jlab.org/> 2828  
2764 [65] JLab DAQ Group, [Jefferson lab f250 flash adc module](#). 2829  
2765 URL [https://coda.jlab.org/drupal/node/91/](https://coda.jlab.org/drupal/node/91/10671311) 2830  
2766 [10671311](https://coda.jlab.org/drupal/node/91/10671311) 2831  
2767 [66] CAEN, [Caen v1190 time to digital converter](#). 2832  
2768 URL <https://www.caen.it/products/v1190a-2esst/> 2833  
2769 [67] EPICS Collaboration, [Experimental physics and industrial control system \(epics\)](#). 2834  
2770 URL <https://epics-controls.org/> 2835  
2771 [68] JLab Scientific Computing, [Jefferson lab farm](#). 2836  
2772 URL <https://scicomp.jlab.org> 2837  
2773 [69] O. Hansen *et al.*, [Hall a analyzer](#). 2838  
2774 URL <https://redmine.jlab.org/projects/podd/wiki> 2839  
2775 [70] R. Brun, F. Rademakers, [Root — an object oriented data](#) 2840  
2776 [analysis framework](#), Nuclear Instruments and Methods in 2841  
2777 Physics Research Section A: Accelerators, Spectrometers, 2842  
2778 Detectors and Associated Equipment 389 (1) (1997) 81–86, 2843  
2779 new Computing Techniques in Physics Research V. doi: 2844  
2780 [https://doi.org/10.1016/S0168-9002\(97\)00048-X](https://doi.org/10.1016/S0168-9002(97)00048-X). 2845  
2781 URL [https://www.sciencedirect.com/science/](https://www.sciencedirect.com/science/article/pii/S016890029700048X) 2846  
2782 [article/pii/S016890029700048X](https://www.sciencedirect.com/science/article/pii/S016890029700048X) 2847  
2783 [71] E. Brash, J. Hovdebo, G. Lolos, G. Huber, R. van der 2848  
2784 Meer, Z. Papandreou, [Operational performance of the](#) 2849  
[hall a mirror aerogel cherenkov counter](#), Nuclear In-  
struments and Methods in Physics Research Section  
A: Accelerators, Spectrometers, Detectors and Associated  
Equipment 487 (3) (2002) 346–352. doi:[https://doi.org/10.1016/S0168-9002\(01\)02199-4](https://doi.org/10.1016/S0168-9002(01)02199-4).  
URL [https://www.sciencedirect.com/science/](https://www.sciencedirect.com/science/article/pii/S0168900201021994)  
[article/pii/S0168900201021994](https://www.sciencedirect.com/science/article/pii/S0168900201021994)  
[72] O. Ullaland, [Fluid systems for rich detectors](#), Nuclear In-  
struments and Methods in Physics Research Section A:  
Accelerators, Spectrometers, Detectors and Associated  
Equipment 553 (1) (2005) 107–113, proceedings of the  
fifth International Workshop on Ring Imaging Detectors.  
doi:<https://doi.org/10.1016/j.nima.2005.08.033>.  
URL [https://www.sciencedirect.com/science/](https://www.sciencedirect.com/science/article/pii/S0168900205015779)  
[article/pii/S0168900205015779](https://www.sciencedirect.com/science/article/pii/S0168900205015779)  
[73] D. Bhetuwal, J. Matter, H. Szumila-Vance, M. L. Kabir,  
D. Dutta, R. Ent, D. Abrams, Z. Ahmed, B. Aljawrneh, S. Al-  
salmi, R. Ambrose, D. Androic, W. Armstrong, A. Asaturyan,  
K. Assumin-Gyimah, C. Ayerbe Gayoso, A. Bandari, S. Basnet,  
V. Berdnikov, H. Bhatt, D. Biswas, W. U. Boeglin, P. Bosted,  
E. Brash, M. H. S. Bukhari, H. Chen, J. P. Chen, M. Chen,  
E. M. Christy, S. Covrig, K. Craycraft, S. Danagoulian,  
D. Day, M. Diefenthaler, M. Dlamini, J. Dunne, B. Duran,  
R. Evans, H. Fenker, N. Fomin, E. Fuchey, D. Gaskell, T. N.  
Gautam, F. A. Gonzalez, J. O. Hansen, F. Hauenstein, A. V.  
Hernandez, T. Horn, G. M. Huber, M. K. Jones, S. Joosten,  
A. Karki, C. Keppel, A. Khanal, P. M. King, E. Kinney, H. S.  
Ko, M. Kohl, N. Lashley-Colthirst, S. Li, W. B. Li, A. H.  
Liyanage, D. Mack, S. Malace, P. Markowitz, D. Meekins,  
R. Michaels, A. Mkrtchyan, H. Mkrtchyan, S. J. Nazeer,  
S. Nanda, G. Niculescu, I. Niculescu, D. Nguyen, Nuruzza-  
man, B. Pandey, S. Park, E. Pooser, A. Puckett, M. Rehfuss,  
J. Reinhold, N. Santiesteban, B. Sawatzky, G. R. Smith, A. Sun,  
V. Tadevosyan, R. Trotta, S. A. Wood, C. Yero, J. Zhang,  
[Ruling out color transparency in quasielastic  \$^{12}\text{C}\(e, e' p\)\$  up to  \$Q^2\$  of 14.2 \(GeV/c\) \$^2\$](#) , Phys. Rev. Lett. 126 (2021) 082301.  
doi:10.1103/PhysRevLett.126.082301.  
URL [https://link.aps.org/doi/10.1103/](https://link.aps.org/doi/10.1103/PhysRevLett.126.082301)  
[PhysRevLett.126.082301](https://link.aps.org/doi/10.1103/PhysRevLett.126.082301)  
[74] D. Bhetuwal, J. Matter, H. Szumila-Vance, C. A. Gayoso,  
M. L. Kabir, D. Dutta, R. Ent, D. Abrams, Z. Ahmed, B. Al-  
jawrneh, S. Alsalmi, R. Ambrose, D. Androic, W. Armstrong,  
A. Asaturyan, K. Assumin-Gyimah, A. Bandari, S. Basnet,  
V. Berdnikov, H. Bhatt, D. Biswas, W. U. Boeglin, P. Bosted,  
E. Brash, M. H. S. Bukhari, H. Chen, J. P. Chen, M. Chen,  
E. M. Christy, S. Covrig, K. Craycraft, S. Danagoulian,  
D. Day, M. Diefenthaler, M. Dlamini, J. Dunne, B. Duran,  
R. Evans, H. Fenker, N. Fomin, E. Fuchey, D. Gaskell, T. N.  
Gautam, F. A. Gonzalez, J. O. Hansen, F. Hauenstein, A. V.  
Hernandez, T. Horn, G. M. Huber, M. K. Jones, S. Joosten,  
A. Karki, C. Keppel, A. Khanal, P. M. King, E. Kinney, H. S.  
Ko, M. Kohl, N. Lashley-Colthirst, S. Li, W. B. Li, A. H.  
Liyanage, D. Mack, S. Malace, P. Markowitz, D. Meekins,  
R. Michaels, A. Mkrtchyan, H. Mkrtchyan, S. J. Nazeer,  
S. Nanda, G. Niculescu, I. Niculescu, D. Nguyen, Nuruzza-  
man, B. Pandey, S. Park, E. Pooser, A. Puckett, M. Rehfuss,  
J. Reinhold, N. Santiesteban, B. Sawatzky, G. R. Smith, A. Sun,  
V. Tadevosyan, R. Trotta, S. A. Wood, C. Yero, J. Zhang,  
[Constraints on the onset of color transparency from quasielastic  \$^{12}\text{C}\(e, e' p\)\$  up to  \$Q^2 = 14.2\$  \(GeV/c\) \$^2\$](#) , Phys. Rev. C 108 (2023) 025203.  
doi:10.1103/PhysRevC.108.025203.  
URL [https://link.aps.org/doi/10.1103/PhysRevC.](https://link.aps.org/doi/10.1103/PhysRevC.108.025203)  
[108.025203](https://link.aps.org/doi/10.1103/PhysRevC.108.025203)  
[75] A. Karki, D. Biswas, F. A. Gonzalez, W. Henry, C. Morean,

- 2850 A. Nadeeshani, A. Sun, D. Abrams, Z. Ahmed, B. Aljawrneh, 2915  
2851 S. Alsalmi, R. Ambrose, D. Androic, W. Armstrong, J. Arring- 2916  
2852 ton, A. Asaturyan, K. Assumin-Gyimah, C. Ayerbe Gayoso, 2917  
2853 A. Bandari, J. Bane, J. Barrow, S. Basnet, V. Berdnikov, 2918  
2854 H. Bhatt, D. Bhetuwal, W. U. Boeglin, P. Bosted, E. Brash, 2919  
2855 M. H. S. Bukhari, H. Chen, J. P. Chen, M. Chen, M. E. 2920  
2856 Christy, S. Covrig, K. Craycraft, S. Danagoulian, D. Day, 2921  
2857 M. Diefenthaler, M. Dlamini, J. Dunne, B. Duran, D. Dutta, 2922  
2858 C. Elliott, R. Ent, H. Fenker, N. Fomin, E. Fuchey, D. Gaskell, 2923  
2859 T. N. Gautam, J. O. Hansen, F. Hauenstein, A. V. Hernandez, 2924  
2860 T. Horn, G. M. Huber, M. K. Jones, S. Joosten, M. L. Kabir, 2925  
2861 N. Kalantarians, C. Keppel, A. Khanal, P. M. King, E. Kinney, 2926  
2862 H. S. Ko, M. Kohl, N. Lashley-Colthirst, S. Li, W. B. Li, 2927  
2863 A. H. Liyanage, D. Mack, S. Malace, P. Markowitz, J. Matter, 2928  
2864 D. Meekins, R. Michaels, A. Mkrtchyan, H. Mkrtchyan, 2929  
2865 S. Nanda, D. Nguyen, G. Niculescu, I. Niculescu, Nuruzzaman, 2930  
2866 B. Pandey, S. Park, E. Pooser, A. J. R. Puckett, M. Rehfuss, 2931  
2867 J. Reinhold, N. Santiesteban, B. Sawatzky, G. R. Smith, 2932  
2868 H. Szumila-Vance, A. S. Tadepalli, V. Tadevosyan, R. Trotta, 2933  
2869 S. A. Wood, C. Yero, J. Zhang, *First measurement of the* 2934  
2870 *emc effect in  $^{10}\text{B}$  and  $^{11}\text{B}$* , *Phys. Rev. C* 108 (2023) 035201. 2935  
2871 [doi:10.1103/PhysRevC.108.035201](https://doi.org/10.1103/PhysRevC.108.035201). 2936  
2872 URL [https://link.aps.org/doi/10.1103/PhysRevC.](https://link.aps.org/doi/10.1103/PhysRevC.108.035201) 2937  
2873 [108.035201](https://link.aps.org/doi/10.1103/PhysRevC.108.035201) 2938  
2874 [76] C. Yero, D. Abrams, Z. Ahmed, A. Ahmidouch, B. Al- 2939  
2875 jawrneh, S. Alsalmi, R. Ambrose, W. Armstrong, A. Asaturyan, 2940  
2876 K. Assumin-Gyimah, C. Ayerbe Gayoso, A. Bandari, J. Bane, 2941  
2877 S. Basnet, V. V. Berdnikov, J. Bericic, H. Bhatt, D. Bhetuwal, 2942  
2878 D. Biswas, W. U. Boeglin, P. Bosted, E. Brash, M. H. S. 2943  
2879 Bukhari, H. Chen, J. P. Chen, M. Chen, M. E. Christy, 2944  
2880 S. Covrig, K. Craycraft, S. Danagoulian, D. Day, M. Diefen- 2945  
2881 thaler, M. Dlamini, J. Dunne, B. Duran, D. Dutta, R. Ent, 2946  
2882 R. Evans, H. Fenker, N. Fomin, E. Fuchey, D. Gaskell, T. N. 2947  
2883 Gautam, F. A. Gonzalez, J. O. Hansen, F. Hauenstein, A. V. 2948  
2884 Hernandez, T. Horn, G. M. Huber, M. K. Jones, S. Joosten, 2949  
2885 M. L. Kabir, A. Karki, C. E. Keppel, A. Khanal, P. King, 2950  
2886 E. Kinney, N. Lashley-Colthirst, S. Li, W. B. Li, A. H. 2951  
2887 Liyanage, D. J. Mack, S. P. Malace, J. Matter, D. Meekins, 2952  
2888 R. Michaels, A. Mkrtchyan, H. Mkrtchyan, S. J. Nazeer, 2953  
2889 S. Nanda, G. Niculescu, M. Niculescu, D. Nguyen, N. Nuruzza- 2954  
2890 man, B. Pandey, S. Park, C. F. Perdrisat, E. Pooser, M. Rehfuss, 2955  
2891 J. Reinhold, B. Sawatzky, G. R. Smith, A. Sun, H. Szumila- 2956  
2892 Vance, V. Tadevosyan, S. A. Wood, J. Zhang, *Probing the* 2957  
2893 *deuteron at very large internal momenta*, *Phys. Rev. Lett.* 125 2958  
2894 (2020) 262501. [doi:10.1103/PhysRevLett.125.262501](https://doi.org/10.1103/PhysRevLett.125.262501). 2959  
2895 URL [https://link.aps.org/doi/10.1103/](https://link.aps.org/doi/10.1103/PhysRevLett.125.262501) 2960  
2896 [PhysRevLett.125.262501](https://link.aps.org/doi/10.1103/PhysRevLett.125.262501) 2961  
2897 [77] R. Li, N. Sparveris, H. Atac, M. K. Jones, M. Paolone, Z. Akbar, 2962  
2898 C. A. Gayoso, V. Berdnikov, D. Biswas, M. Boer, A. Camsonne, 2963  
2899 J.-P. Chen, M. Diefenthaler, B. Duran, D. Dutta, D. Gaskell, 2964  
2900 O. Hansen, F. Hauenstein, N. Heinrich, W. Henry, T. Horn, 2965  
2901 G. M. Huber, S. Jia, S. Joosten, A. Karki, S. J. D. Kay, V. Kum- 2966  
2902 ar, X. Li, W. B. Li, A. H. Liyanage, S. Malace, P. Markowitz, 2967  
2903 M. McCaughan, Z.-E. Meziani, H. Mkrtchyan, C. Morean, 2968  
2904 M. Muhoza, A. Narayan, B. Pasquini, M. Rehfuss, B. Sawatzky, 2969  
2905 G. R. Smith, A. Smith, R. Trotta, C. Yero, X. Zheng, J. Zhou, 2970  
2906 *Measured proton electromagnetic structure deviates from theo-* 2971  
2907 *retical predictions*, *Nature* 611 (7935) (2022) 265–270. [doi:](https://doi.org/10.1038/s41586-022-05248-1) 2972  
2908 [10.1038/s41586-022-05248-1](https://doi.org/10.1038/s41586-022-05248-1). 2973  
2909 URL <https://doi.org/10.1038/s41586-022-05248-1> 2974  
2910 [78] B. Duran, Z.-E. Meziani, S. Joosten, M. K. Jones, S. Prasad, 2975  
2911 C. Peng, W. Armstrong, H. Atac, E. Chudakov, H. Bhatt, 2976  
2912 D. Bhetuwal, M. Boer, A. Camsonne, J.-P. Chen, M. M. Dalton, 2977  
2913 N. Deokar, M. Diefenthaler, J. Dunne, L. El Fassi, E. Fuchey, 2978  
2914 H. Gao, D. Gaskell, O. Hansen, F. Hauenstein, D. Higin- 2979
- botham, S. Jia, A. Karki, C. Keppel, P. King, H. S. Ko, X. Li, R. Li, D. Mack, S. Malace, M. McCaughan, R. E. McClellan, R. Michaels, D. Meekins, M. Paolone, L. Pentchev, E. Pooser, A. Puckett, R. Radloff, M. Rehfuss, P. E. Reimer, S. Rior- dan, B. Sawatzky, A. Smith, N. Sparveris, H. Szumila-Vance, S. Wood, J. Xie, Z. Ye, C. Yero, Z. Zhao, *Determining the gluonic gravitational form factors of the proton*, *Nature* 615 (7954) (2023) 813–816. [doi:10.1038/s41586-023-05730-4](https://doi.org/10.1038/s41586-023-05730-4). URL <https://doi.org/10.1038/s41586-023-05730-4>
- [79] A. Accardi, P. Achenbach, D. Adhikari, A. Afanasev, C. S. Akondi, N. Akopov, M. Albaladejo, H. Albataineh, M. Albrecht, B. Almeida-Zamora, M. Amaryan, D. Androic, W. Armstrong, D. S. Armstrong, M. Arratia, J. Arrington, A. Asaturyan, A. Austregesilo, H. Avagyan, T. Averett, C. A. Gayoso, A. Bacchetta, A. B. Balantekin, N. Baltzell, L. Barion, P. C. Barry, A. Bashir, M. Battaglieri, V. Bellini, I. Belov, O. Benhar, B. Benkel, F. Benmokhtar, W. Bentz, V. Bertone, H. Bhatt, A. Bianconi, L. Bibrzycki, R. Bijker, D. Binosi, D. Biswas, M. Boer, W. Boeglin, S. A. Bogacz, M. Boggione, M. Bondi, E. E. Boos, P. Bosted, G. Bozzi, E. J. Brash, R. A. Briceño, P. D. Brindza, W. J. Briscoe, S. J. Brodsky, W. K. Brooks, V. D. Burkert, A. Camsonne, T. Cao, L. S. Cardman, D. S. Carman, M. Carpinelli, G. D. Cates, J. Caylor, A. Celentano, F. G. Celiberto, M. Cerutti, L. Chang, P. Chatagnon, C. Chen, J.-P. Chen, T. Chetry, A. Christopher, E. Christy, E. Chudakov, E. Cisbani, I. C. Cloët, J. J. Cobos-Martinez, E. O. Cohen, P. Colangelo, P. L. Cole, M. Constantinou, M. Contalbrigo, G. Costantini, W. Cosyn, C. Cotton, A. Courtoy, S. C. Dusa, V. Crede, Z. F. Cui, A. D’Angelo, M. Döring, M. M. Dalton, I. Danilkin, M. Davydov, D. Day, F. D. Fazio, M. D. Napoli, R. D. Vita, D. J. Dean, M. Defurne, A. Deur, B. Devkota, S. Dhital, P. D. Nezza, M. Diefenthaler, S. Diehl, C. Dilks, M. Ding, C. Djalali, S. Dobbbs, R. Dupré, D. Dutta, R. G. Edwards, H. Egiyan, L. Ehinger, G. Eichmann, M. Elaasar, L. Elouadrhiri, A. E. Alaoui, L. E. Fassi, A. Emmert, M. Engelhardt, R. Ent, D. J. Ernst, P. Eugenio, G. Evans, C. Fanelli, S. Fegan, C. Fernández-Ramírez, L. A. Fernandez, I. P. Fernando, A. Filippi, C. S. Fischer, C. Fogler, N. Fomin, L. Frankfurt, T. Frederico, A. Freese, Y. Fu, L. Gamber, L. Gan, F. Gao, H. Garcia-Tecocoatzi, D. Gaskell, A. Gasparian, K. Gates, G. Gavalian, P. K. Ghoshal, A. Giachino, F. Giacosa, F. Gianuzzi, G. P. Gilfoyle, F.-X. Girod, D. I. Glazier, C. Gleason, S. Godfrey, J. L. Goity, A. A. Golubenko, S. González-Solís, R. W. Gothe, Y. Gotra, K. Griffioen, O. Grocholski, B. Grube, P. Guèye, F. K. Guo, Y. Guo, L. Guo, T. J. Hague, N. Hammoud, J. O. Hansen, M. Hattawy, F. Hauenstein, T. Hayward, D. Heddle, N. Heinrich, O. Hen, D. W. Higinbotham, I. M. Higuera-Angulo, A. N. H. Blin, A. Hobart, T. Hobbs, D. E. Holmberg, T. Horn, P. Hoyer, G. M. Huber, P. Hurck, P. T. P. Hutaaruk, Y. Ilieva, I. Illari, D. G. Ireland, E. L. Isupov, A. Italiano, I. Jaegle, N. S. Jarvis, D. Jenkins, S. Jeschonnek, C.-R. Ji, H. S. Jo, M. Jones, R. T. Jones, D. C. Jones, K. Joo, M. Ju- naid, T. Kageya, N. Kalantarians, A. Karki, G. Karyan, A. T. Katramatou, S. J. D. Kay, R. Kazimi, C. D. Keith, C. Keppel, A. Kerbizi, V. Khachatryan, A. Khanal, M. Khandaker, A. Kim, E. R. Kinney, M. Kohl, A. Kotzinian, B. T. Kriesten, V. Kubarovskiy, B. Kubis, S. E. Kuhn, V. Kumar, T. Kutz, M. Leali, R. F. Lebed, P. Lenisa, L. Leskovec, S. Li, X. Li, J. Liao, H. W. Lin, L. Liu, S. Liuti, N. Liyanage, Y. Lu, I. J. D. MacGregor, D. J. Mack, L. Maiani, K. A. Mamo, G. Mandaglio, C. Mariani, P. Markowitz, H. Marukyan, V. Mascagna, V. Mathieu, J. Maxwell, M. Mazouz, M. McCaughan, R. D. McKeown, B. McKinnon, D. Meekins, W. Melnitchouk, A. Metz, C. A. Meyer, Z. E. Meziani, C. Mezzag, R. Michaels, G. A. Miller, T. Mineeva, A. S. Miramontes, M. Mirazita, K. Mizu-

2980 tani, H. Mkrtchyan, A. Mkrtchyan, B. Moffit, P. Mohanmurthy,  
2981 V. I. Mokeev, P. Monaghan, G. Montaña, R. Montgomery,  
2982 A. Moretti, J. M. M. Chávez, U. Mosel, A. Movsisyan, P. Mu-  
2983 sico, S. A. Nadeeshani, P. M. Nadolsky, S. X. Nakamura,  
2984 J. Nazeer, A. V. Nefediev, K. Neupane, D. Nguyen, S. Nic-  
2985 colai, I. Niculescu, G. Niculescu, E. R. Nocera, M. Nycz,  
2986 F. I. Olness, P. G. Ortega, M. Osipenko, E. Pace, B. Pandey,  
2987 P. Pandey, Z. Papandreou, J. Papavassiliou, L. L. Pappalardo,  
2988 G. Paredes-Torres, R. Paremuzyan, S. Park, B. Parsamyan,  
2989 K. D. Paschke, B. Pasquini, E. Passemar, E. Pasyuk, T. Patel,  
2990 C. Paudel, S. J. Paul, J.-C. Peng, L. Pentchev, R. Perrino, R. J.  
2991 Perry, K. Peters, G. G. Petratos, W. Phelps, E. Piasetzky, A. Pil-  
2992 lioni, B. Pire, D. Pitonyak, M. L. Pitt, A. D. Polosa, M. Pospelov,  
2993 A. C. Postuma, J. Poudel, L. Preet, S. Prelovsek, J. W. Price,  
2994 A. Prokudin, A. J. R. Puckett, J. R. Pybus, S. X. Qin, J. W.  
2995 Qiu, M. Radici, H. Rashidi, A. D. Rathnayake, B. A. Raue,  
2996 T. Reed, P. E. Reimer, J. Reinhold, J. M. Richard, M. Rinaldi,  
2997 F. Ringer, M. Ripani, J. Ritman, J. R. West, A. Rivero-Acosta,  
2998 C. D. Roberts, A. Rodas, S. Rodini, J. Rodríguez-Quintero,  
2999 T. C. Rogers, J. Rojo, P. Rossi, G. C. Rossi, G. Salmè, S. N.  
3000 Santiesteban, E. Santopinto, M. Sargsian, N. Sato, S. Schad-  
3001 mand, A. Schmidt, S. M. Schmidt, G. Schnell, R. A. Schu-  
3002 macher, P. Schweitzer, I. Scimemi, K. C. Scott, D. A. Seay,  
3003 J. Segovia, K. Semenov-Tian-Shansky, A. Seryi, A. S. Sharda,  
3004 M. R. Shepherd, E. V. Shirokov, S. Shrestha, U. Shrestha, V. I.  
3005 Shvedunov, A. Signori, K. J. Slifer, W. A. Smith, A. Somov,  
3006 P. Souder, N. Sparveris, F. Spizzo, M. Spreafico, S. Stepanyan,  
3007 J. R. Stevens, I. I. Strakovsky, S. Strauch, M. Strikman, S. Su,  
3008 B. C. L. Sumner, E. Sun, M. Suresh, C. Sutura, E. S. Swan-  
3009 son, A. P. Szczepaniak, P. Sznajder, H. Szumila-Vance, L. Szy-  
3010 manowski, A. S. Tadealli, V. Tadevosyan, B. Tamang, V. V.  
3011 Tarasov, A. Thiel, X. B. Tong, R. Tyson, M. Ungaro, G. M.  
3012 Urciuoli, A. Usman, A. Valcarce, S. Vallarino, C. A. Vaquera-  
3013 Araujo, L. Venturelli, F. Vera, A. Vladimirov, A. Vossen, J. Wag-  
3014 ner, X. Wei, L. B. Weinstein, C. Weiss, R. Williams, D. Win-  
3015 ney, B. Wojtsekhowski, M. H. Wood, T. Xiao, S. S. Xu, Z. Ye,  
3016 C. Yero, C. P. Yuan, M. Yurov, N. Zachariou, Z. Zhang, Z. W.  
3017 Zhao, Y. Zhao, X. Zheng, X. Zhou, V. Ziegler, B. Zihlmann,  
3018 W. de Paula, G. F. de Téramond, Strong interaction physics at  
3019 the luminosity frontier with 22 gev electrons at jefferson lab  
3020 (2023). [arXiv:2306.09360](https://arxiv.org/abs/2306.09360).